NTNU

Norwegian University of
Science and Technology

Numerical Study of the Interaction of Flow over Two Airfoils in Relative Motion

Vebjørn Tveiterås

Master of Science in Physics and Mathematics

Submission date: June 2011

Supervisor: Jon Andreas Støvneng, IFY

Co-supervisor: Bernhard Müller, EPT
Kristian Einarsrud, EPT
Per-Åge Krogstad, EPT

Norwegian University of Science and Technology
Department of Physics

Numerical study of the interaction of flow over two airfoils in relative motion

Vebjørn Tveiterås

Abstract

Computational fluid dynamics (CFD) was be used to investigate aspects of interaction of flow over two airfoils in relatie motion in detail.

2D tandem airfoil setups were studied, where the leading airfoil was performing an oscillating motion in the vertical direction while the trailing airfoil was kept stationary. The NACA 0012 and the S809 airfoils were considered.

Ansys Fluent v13.0 was used as the CFD solver, and Gambit v2.4.6 was employed for grid generation. All simulations were transient at a Reynolds number of either $2{\cdot}10^4$ (laminar flow) or $3{\cdot}10^6$ (turbulent flow). The Transition SST turbulence model was chosen to model turbulence, and Fluent's sliding grid technique was used to achieve the relative motion between the airfoils.

The tandem setup was found able to outperform a single airfoil for similar conditions. The presence of a trailing airfoil did not significantly affect the leading airfoil's performance, whereas it did affect the wake structures significanlty. The suction peak near the nose of the airfoil was found to be the most important factor determining the airfoil's propulsive efficiency. Therefore, leading edge vortex (LEV) shedding was found to be of higher importance than trailing edge vortex (TEV) shedding when airfoil performance was concidered.

The asymmetric S809 airfoil provided similar results as the symmetric NACA 0012 airfoil. However, the NACA 0012 airfoil achieved slightly higher propulsive efficiencies for the cases investigated, indicating that a symmetric airfoil is desired for flapping airfoil setups. For the tandem setup the highest propulsive efficienies were 0.766 and 0.742 for the NACA 0012 airfoil and the S809 airfoil, respectively. Both peaks were found at $k = 0.3$ and $h = 0.6$ ($Sr = 0.11$) for the leading airfoil. A maximum thrust coefficient of 2.32 was found for the tandem S809 airfoil setup at $k = 1.5$ and $h = 0.5$ ($Sr = 0.48$).

The Strouhal number was found to be an important describing parameter, but additional information about the reduced frequency or the oscillating amplitude was needed in order to fully describe the setup.

Preface

Background for project

First, it should be mentioned that this work was intended to focus on interactions between wind turbines. However, it ended up with a focus on flapping airfoils, mainly because of coincidences. Still, aspects of this report may be of interest for wind turbine technology.

This report is written as a requirement to obtain the degree of Master of Science (Sivilingeniør) at the Norwegian University of Science and Technology (NTNU). The report is to serve as a documentation of all work done during the 10th semester of the degree. The project is awarded 30 credits, corresponding to approximately 700 hours of work over 20 weeks.

Report organization

The report is organized into eight chapters and three appendixes.

Chapter one: Introduction presents the background for the study and choice of airfoil. A litterature review is also included.

Chapter two: Theory gives an overview of different theoretical aspects relevant for this study.

Chapter three: Numerical methods covers some of the numerical methods that are relevant for this study. Solver settings are also presented.

Chapter four: Grid generation explains basic concepts of grid generation. Descriptions of the grids used are also covered, as well as a presentation of the sliding grid technique.

Chapter five: Model verifcation and validation presents results from the verification and validation processes.

Chapter six: Results and discussion presents the simulation results for flow over a tandem setup. Parameter dependency is first discussed, followed by focus on airfoil performance. Theory from chapter two is used to explain different flow feautures.

Chapter seven: Model uncertainties reviews uncertainties in the model setup based on post-processing of the results from the numerical simulations.

Chapter eight: Conclusions summarizes the study. Issues for further research are included at the end of this chapter.

Three appendices are included at the end of the report. They cover high performance computing, user-defined functions, and results from regression analysis.

Following the appendices is a bibliography.

Acknowledgements

I would like to thank my supervisor Bernhard Müller for both his advice and motivation throughout the spring. His continous thorough feedback provided me with new ways of looking at my problems; crucial for overcoming many of the obstacles I faced. He also made sure I stayed on track, despite the sometimes overwhelming choices of different paths a work of this scale usually offers.

Both Kristian E. Einarsrud and Per-Åge Krogstad have also been of assistance during this study. Special thanks go to Kristian E. Einarsrud for always keeping his door open and offering his greatly appreciated help.

I would also like to thank Jon Andreas Støvneng for being my formal advisor.

At last, I would like to thank two of my fellow students for help with proof-reading my report: Kristoffer Hellton and Nikolai H. Rivedal.

Contents

List of Figures

List of Tables

Nomenclature

Some symbols have more than one definition. In the report it is given by context which definition is used.

α	Angle of attack
β	Under relaxation factor
δ_{ij}	The Kronecker delta, $\delta_{ij} = 1$ for $i = j$ and $\delta_{ij} = 0$ otherwise
ϵ	Turbulent dissipation
η	Propulsive efficiency, $\frac{C_{T\text{mean}}}{C_{\text{Power-mean}}}$
Γ	Diffusion coefficient
γ	intermittency
Γ_k	Effective diffusitivity of turbulence kinetic energy
Γ_ω	Effective diffusitivity of ω
μ	Kinematic viscosity
μ_t	Eddy viscosity
μ_τ	Friction velocity, $\sqrt{\frac{\tau_w}{\rho}}$
ν	Dynamic viscosity
ω	Oscillation frequency, $2\pi f$
ϕ	A fluid property or variable
ρ	Fluid density
τ_ω	Wall shear stress
τ_{ij}	Specific Reynolds stress tensor, $-\rho\overline{u'_j u'_i}$
τ	Stress tensor
$\mathbf{F}$	Force vector
$\mathbf{g}$	Gravity
$\mathbf{r}$	Spatial displacment vector
$\mathbf{v}$	Velocity vector
A	Characteristic length
a	Oscillation amplitude
C	Airfoil Chord length
C_{Power}	Power coefficient, $\frac{-C_L \dot{y}}{U_0}$
C_{Pressure}	Pressure coefficient, $\frac{p-p_0}{\frac{1}{2}\rho U_0^2}$
C_D	Drag coefficient, $\frac{D}{\frac{1}{2}\rho U_0^2 C}$
C_L	Lift coefficient, $\frac{L}{\frac{1}{2}\rho U_0^2 C}$
C_T	Thrust coefficient, $\frac{-D}{\frac{1}{2}\rho U_0^2 C}$
D	Drag
D_k	Dissipation of k

D_ω	Cross-diffusion between ω and k
e	East face of control volume
f	Oscillation frequency
G_k	Generation of turbulence kinetic energy
G_ω	Generation of ω
h	Non-dimensional amplitude, $\frac{h}{C}$
k	Reduced frequency, $\frac{\pi f C}{U_0}$
k	Turbulent kinetic energy per unit mass, $\frac{1}{2}\sum_{i=1}^{3}\overline{u_i'^2}$
L	Characteristic length
L	Lift
l_0	Length scale
n	Time level
p	Pressure
p_0	Free stream pressure
P_k	Production of k
Q_{EAS}	Equiangle skew
Re	Reynolds number
$Re_{\theta t}$	Transition onset Reynolds number
$Re_{x,\mathrm{crit}}$	Critical Reynolds number for stable laminar flow
$Re_{x,\mathrm{tr}}$	Transitional Reynolds number
s_{ij}	Strain rate tensor, $\frac{1}{2}\left(\frac{\partial u_i}{\partial x_j}+\frac{\partial u_j}{\partial x_i}\right)$
Sr	Strouhal number
T	Oscillation period
t	Thickness for NACA 00XX series
t	Time
t_{ij}	Viscous stress tensor, $2\mu s_{ij}$
U	Characteristic velocity
u	Velocity component
u^+	Non-dimensional velocity, $\frac{u}{\mu_\tau}$
U_0	Free stream velocity
v	Velocity component
v_0	Velocity scale
w	West face of control volume
x, y	Cartesian coordinates
X_{shift}	Horizontal distance between airfoils in tandem setup
y^+	Non-dimensional wall normal distance, $\frac{y\mu_\tau}{\nu}$
Y_k	Dissipation of turbulence kinetic energy
Y_ω	Dissipation of ω

Abbreviations

AIAA	American Institute of Aeronautics and Astronautics
BC	Boundary condition
BL	Boundary layer
CFD	Computational fluid dynamics
CV	Control volume
DNS	Direct numerical simulation
LES	Large eddy simulation

LEV	Leading edge vortex
MAV	Micro air vehicle
PISO	Pressure-implicit with splitting of operatos
PRESTO	Pressure staggering option
RANS	Reynolds averaged Navier-Stokes
SIMPLE	Semi-implicit method for pressure-linked equations
SIMPLEC	SIMPLE consistent
SST	Shear stress transport
TEV	Trailing edge vortex
TI	Turbulent intensity
URANS	Unsteady Reynolds averaged Navier-Stokes
URF	Under relaxation factors

Chapter 1

Introduction

1.1 Background

Most research on oscillating airfoils or wings are motivated mostly by either a better understanding of animals that use flapping motion for propulsion, or the development of micro air vehicles (MAVs)[18, 14]. Also of interest is a bettwer understanding of wing flutter [11]. Wing flutter is of interest for aircrafts, helicopters and turbomachine blades, among others.

As is true for most fields within aeordynamics, flapping-wing aerodynamics is a field that benefits from the use of computational fluid dynamcs (CFD). CFD can compliment experimental results, and also help in designing experiments.

More details on background are covered in the following section.

1.2 Literature review

Knoller [19] and Betz [20] proved as early as 1909 and 1912, respectively, that flapping wings generate thrust and lift due to an effective angle of attack generated as a result of the flapping motion, as may be seen in Figure 1.1. In recent years, the development of MAVs has generated an increased interest in the field of flapping wings, which can be inferred by a study done by Platzer, Jones, Young and Lai [18].

There are still many unresolved issues related to flapping wing aerodynamics [18, 21], such as 3-D effects, investigations of a range of different airfoils, flexible wings and the determination of the conditions for optimal performance. Of special relevance for this study is the investigation of different airfoils than the NACA 0012 profile, which is the most widely used profile in studies of flapping wing aerodynamics. However, since the NACA 0012 profile has been thoroughly tested, there are both numerical and experimental data available for a wide range of case set-ups, which is valuable for validation and verification purposes.

In the study of flapping airfoils it is important to determine the parameters that may be altered in order to optimize the thrust, efficiency or other criteria. The Strouhal number is considered to be one such parameter, it is defined as

$$Sr = \frac{fA}{U_0}, \tag{1.1}$$

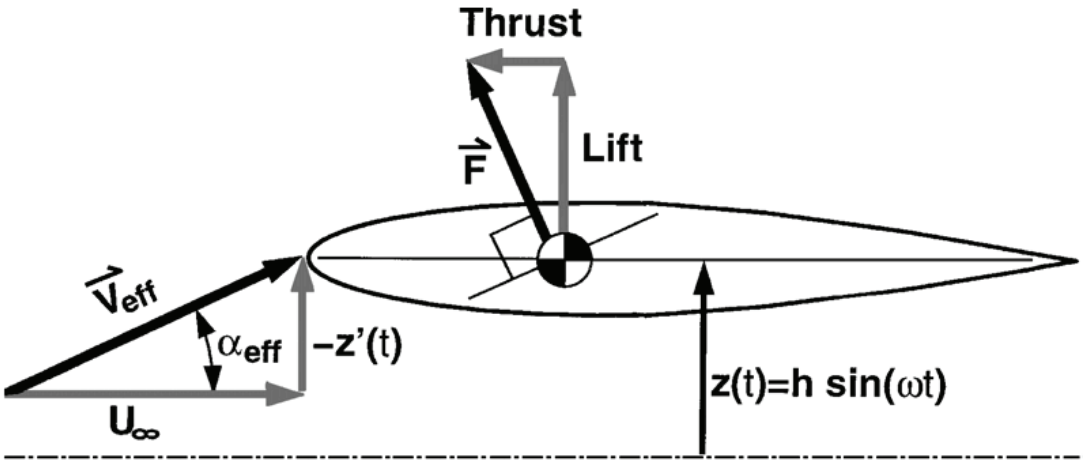

Figure 1.1: Figure showing how the motion of the airfoil forms an effective angle of attack and the resulting forces. From Jones et al. [1]

where f is the oscillation frequency, A is a characteristic length and U_0 is the free stream velocity. Although it has been found by many researchers to be the most important parameter, not all studies conclude that the Strouhal number alone is sufficient to describe the flow.

An analysis done by Taylor et al. [22] of 42 species of birds, bats and insects concluded that the flying animals operate in a narrow range of Strouhal numbers between 0.2 and 0.4. With flapping amplitudes varying greatly among the animals, this indicates that the product kh, and thus the Strouhal number, is a useful similarity parameter to describe flapping motion. A study by Triantafyllou et al. [23], which looked at the operating ranges of several different fish, concluded that all the fish in the study operated at Strouhal numbers between 0.25 and 0.35. This supports the use of Strouhal number as describing parameter.

Jones et al. found an approximate dependence on the Strouhal number in their experiments on a plunging NACA 0012 airfoil. This may be seen in Figure 1.2, where data is sorted depending on the type of wake generated.

Wang [25] performed incompressible Navier-Stokes simulations on an elliptic airfoil in plunging motion. She found that there was an optimum flapping frequency for generation of maximum thrust, which itself varied with Strouhal number. Wang also noted that the interaction of vortices shed from the leading and the trailing edges are important for determining the optimum thrust. This leads to two separate time scales governing the optimum frequency, the times for formation and separation of the leading edge vortex.

Numerical studies performed by Guerrero [2] and Young [26] show that for a given Sr number, leading edge vortex shedding may or may not occur, depending on the frequency-amplitude combination of the Sr number. This is a strong indication that the frequency as well as the Sr number is needed as describing parameters. Leading edge vortex shedding is discussed in Section 6.3.1.

Figure 1.3 shows a contour map of propulsive efficiency for different values of both Strouhal number and heaving amplitude (and thus indirectly frequency) generated by Guerrero [2]. Had the Strouhal number been sufficient to describe

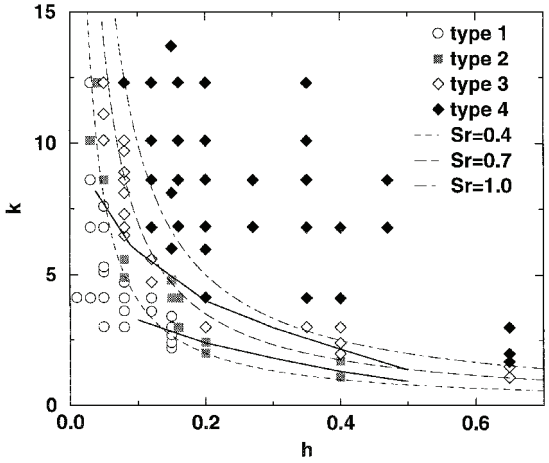

Figure 1.2: Wake classification based on observed vortex positions. Type 1: Drag production, type 2: Neither drag nor thrust, type 3: Thrust production and type 4: Both thrust and lift production. The dotted lines indicate constant Strouhal numbers. The solid lines are curvefit boundaries between type 1, 2 and 3 wake topologies (not fitted to data shown in figure, extracted from Ref. [24]). From Jones et al. [1]

the system, all the contours would have been horizontal. However, this is not the case, and for a given Strouhal number, it is also important to know the amplitude or the frequency.

Experimental studies by Lai and Platzer [11] and Jones et al. [1] investigate the wake structures behind an oscillating NACA 0012 profile for a laminar Reynolds number. Lai and Platzer [11] show through experiments using dye flow visualization how the wake structures changes from drag to thrust as the nondimensional plunge velocity Sr increases. Their experiments showed that drag is induced for Sr lower than about 0.2. In the drag situation the vortices in the upper row (above the horizontal airfoil symmetry axis) rotate clockwise and the vortices in the lower row rotate counterclockwise. This may be seen in Figure 1.4.

As Sr increases the wake turns neutral and two vortices are shed from each side (upper or lower) of the airfoil before two are shed from the opposite side. For Sr values larger than about 0.4, thrust is produced. Only one vortex is shed from each side. The rotation of the vortices are now opposite to that for the drag wake, resulting in a thrust generating jet behind the airfoil. This may be seen in Figure 1.5.

The experiments of Jones et al. [1] indicate that drag occurs for values of Sr up to 0.4, which are higher values than Lai and Platzer [11] observed. In some cases neutral wakes were observed for Sr as high as 0.7. The results also indicate that the Strouhal number alone might not be sufficient to describe the wake characteristics.

Jones et al. [1] also compare numerical data from simulations with an inviscid unsteady panel code to their experimental data, and the results indicate that the thrust-indicative wake structures are primarily inviscid phenomena.

Young and Lai (2004) [27] conclude that flow over a NACA 0012 profile at a

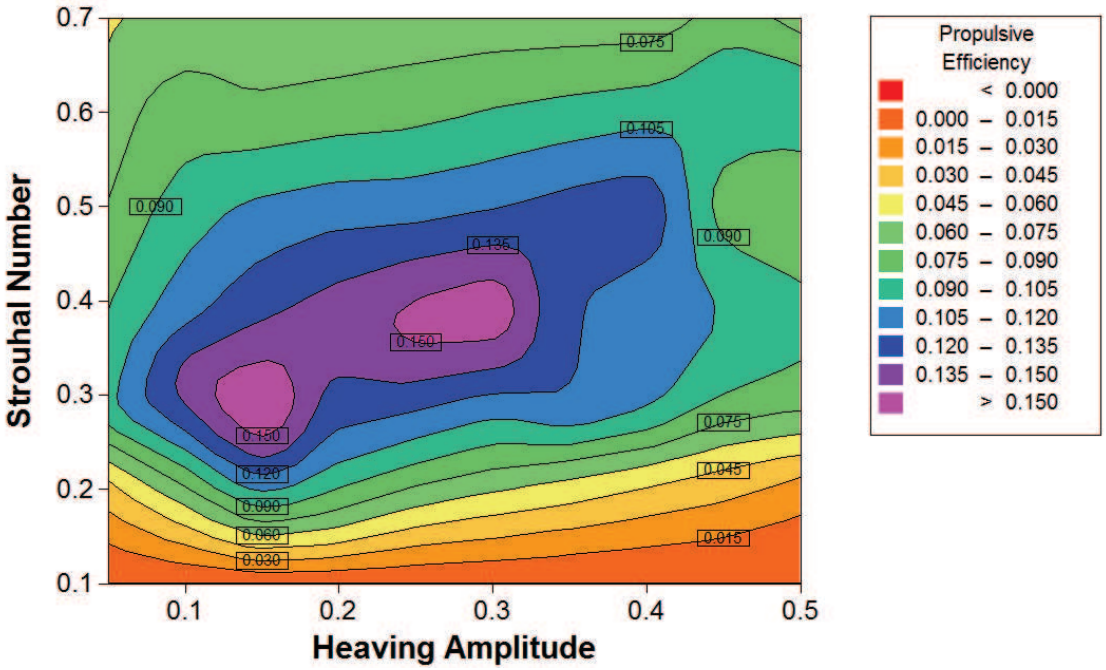

Figure 1.3: Contour map of propulsive efficiency for different Strouhal numbers and heaving amplitudes. From Guerrero [2]

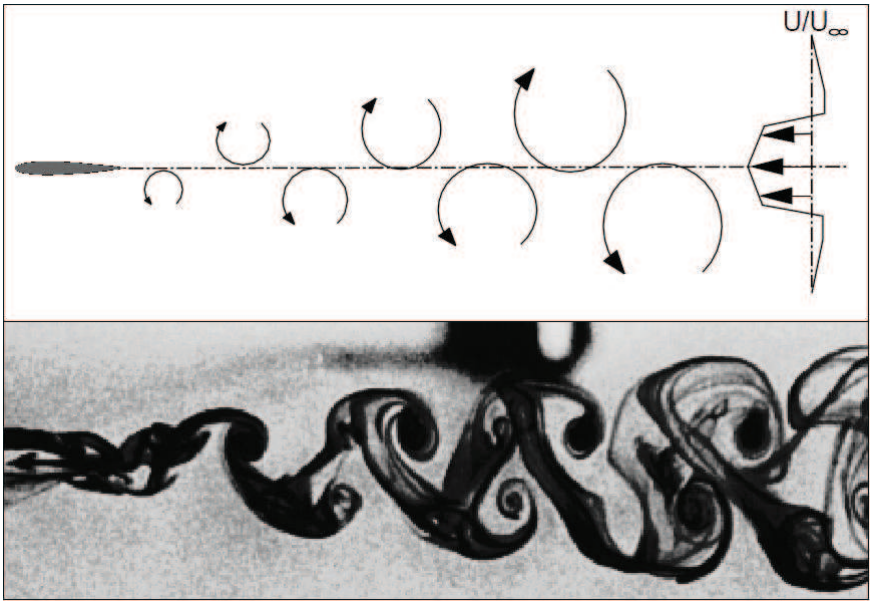

Figure 1.4: Drag indicating vortex street. From Jones et al. [3]

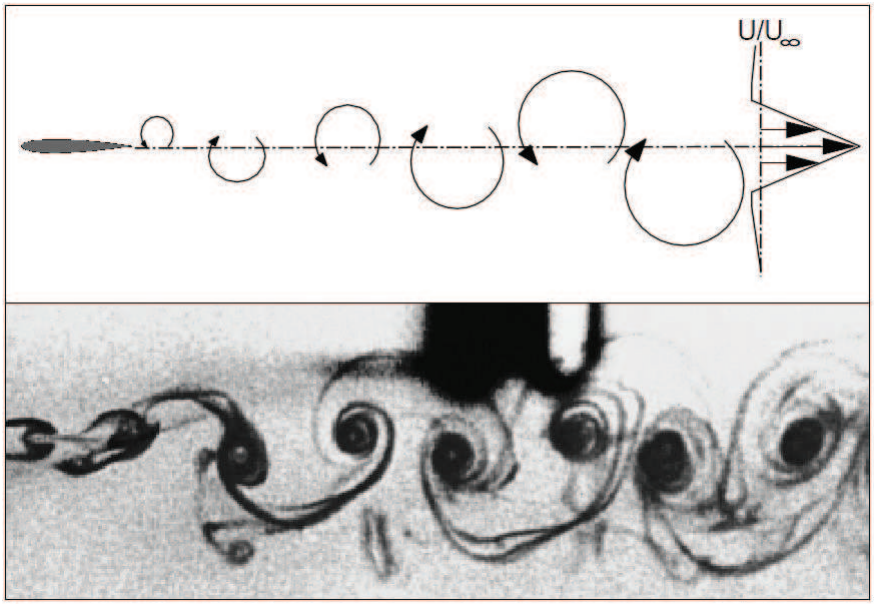

Figure 1.5: Thrust indicating vortex street. From Jones et al. [3]

Reynolds number of 20,000 is laminar, by comparing wake structures from both laminar and turbulent simulations to experiments by Lai and Platzer [11]. They also conclude that the wake structures are primarily determined by trailing edge separations. Aerodynamic forces where shown to be generated by leading edge separation for reduced oscillation frequencies of $k < 4$ while these separations became of secondary importance at higher k. For $k < 4$ they note that k and Sr are the controlling parameters, as opposed to Sr alone. Heathcote et al. [15] claim that the Strouhal number is appropriate for characterizing the power requirements of the heave motion.

The experimental study by Heathcote et al. [15] also concludes that the effects of the Reynolds number are very small for the range $10,000 < Re < 30,000$. Comparisons with numerical studies showed that Navier-Stokes calculations were in good agreement with experimental data while both panel method [1] and Garrick theory [29] give overpredictions in the propulsive efficiency η.

Young and Lai [27] showed through Navies-Stokes simulations that leading edge vortices augment the surface pressures, thus requiring more power to move the airfoil and as a result reducing propulsive efficiency.

Young and Lai [14] achieved good correlation between Navier-Stokes simulations and experimental data from Heathcote [15]. It is also noted that an important factor in the efficiency being reduced for increasing Strouhal number is leading edge vortex shedding. The effect is reduced thrust, while lift, moment and power required to drive the airfoil remain mostly unaffected by the vortices. Flow separation and leadingedge shedding effects appear to be controlled by the reduced frequency by limiting the time available both for vortex formation and convection of the vortex over the airfoil surface.

Tuncer and Platzer [4] performed a numerical study of two NACA 0012 profiles in tandem configuration at Reynolds number of $3.0{\cdot}10^6$. The propulsive efficiency

[1] C.f. the book by Katz and Plotkin[28] for an introduction to the panel method

was found to increase by as much as 40% under certain conditions for the airfoil combination. The optimum separation distance was found to be 2 chord lengths. For an offset in the transverse direction, small changes were observed as long as the offset was less than the flapping amplitude. At offsets higher than the flapping amplitude, the thrust augmentation was reduced significantly.

They also showed that the average thrust coefficient increases as the reduced frequency k increases from 0, while the propulsive efficiency obtaines a maximum and then starts to decrease. This may be seen in Figure 1.6.

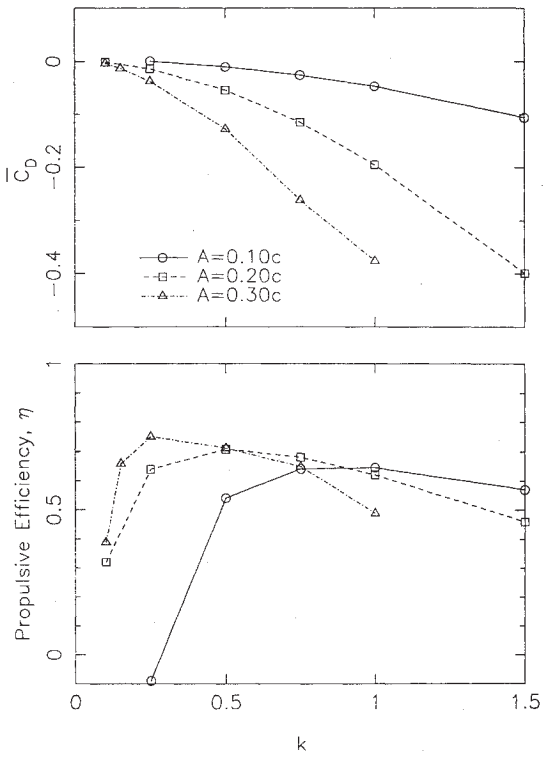

Figure 1.6: Results from Tuncer and Platzer [4] for a tandem setup, where C_D is the drag coefficient, A is the oscillation amplidute and k is the reduced oscillation frequency.

1.3 Airfoil selection

Two airfoils were investigated in this study, the NACA 0012 airfoil and the S809 airfoil. Brief presentations of the airfoils are given here.

The aerodnamics of flapping airfoils has been investigated mostly through experiments and numerical simulations with NACA airfoils, especially the NACA 0012 airfoil [18]. Since it is important for all CFD simulations to verify and validate the model setup, and experimental and numerically generated data is available for the NACA 0012 airfoil, this airfoil was a natural selection as the first airfoil investigated in this study.

The NACA 0012 airfoil was designed by the National Advisory Committee for Aeronautics (NACA). In the NACA XXXX series, the first two digits determine

the camber of the airfoil and the last two digits determine the maximum thickness as percentage of the chord length. The thickness is defined as the ratio between the maximum height of the airfoil and the chord length. The NACA 0012 is a symmetrical airfoil, and it is described by the following function:

$$y = \pm\frac{t}{0.2}C\left[0.2969\sqrt{\frac{x}{C}} - 0.1260\left(\frac{x}{C}\right) - 0.3516\left(\frac{x}{C}\right)^2 + 0.2843\left(\frac{x}{C}\right)^3 - 0.1015\left(\frac{x}{C}\right)^4\right], \tag{1.2}$$

where y is the half thickness at a given value of x, C is the chord length, x is the position along the chord from 0 to C and t is the thickness ($t = 12$ for NACA 0012). The NACA 0012 airfoil may be seen in Figure 1.7.

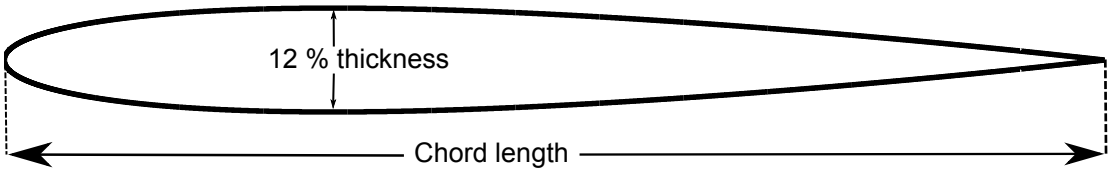

Figure 1.7: The NACA0012 airfoil. The thickness is given in % of the chord length.

Since few other airfoils have been as throroughly tested as the NACA 0012 airfoil, it was of interest to investigate another airfoil and compare the results of the two airfoils. As a second airfoil, the S809 airfoil was chosen. The S809 airfoil was designed for wind turbine blades. Although it has undergone extensive testing (c.f. [30]), its performance while flapping has to the author's knowledge not been thorougly investigated. It also offers insight in how asymmetrical airfoils affect the aerodynamics of flapping airfoils.

The Eppler design code was used to develop the S809 [30]. A set of coordinates describe the geometry, and interpolation between the points is needed to get a complete profile. A cubic spline interpolation scheme was used for this purpose. The S809 airfoil has a thickness of 21%.

Figure 1.8 shows the S809 airfoil as well as common airfoil notation.

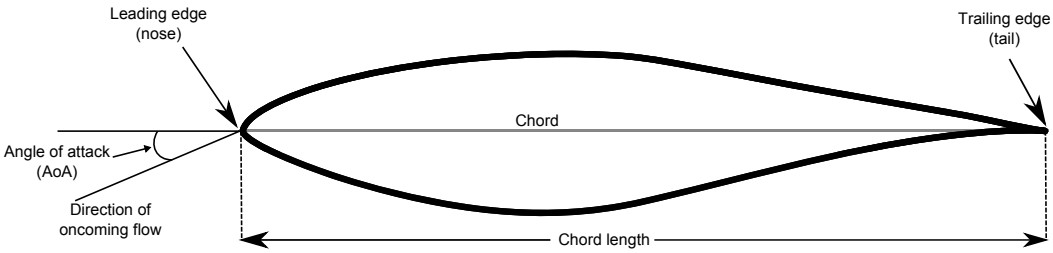

Figure 1.8: The S809 airfoil with selected airfoil notation.

Chapter 2

Theory

The topics covered in these sections are relevant for the physics involved in flow over airfoils. Detailed derivations and descriptions are not given, but rather an overview with focus on key aspects relevant to this study.

2.1 Introduction to CFD

Computational fluid dynamics (CFD), is the process of using numerical methods to solve fluid flow problems. The Navier Stokes equations, which describe the physics of fluid flows, cannot be solved analytically for most real-life flows. An approximate solution is then required. The most relevant equations are the conservation of mass

$$\frac{\partial \rho}{\partial t} + \nabla \cdot (\rho \mathbf{v}) = 0 \tag{2.1}$$

and the conservation of momentum

$$\rho \frac{\partial \mathbf{v}}{\partial t} + \rho \left(\mathbf{v} \cdot \nabla \right) \mathbf{v} = -\nabla p + \rho \mathbf{g} + \nabla \cdot \tau, \tag{2.2}$$

where ρ is the density of the fluid, $\mathbf{v}$ is the velocity vector, p is the fluids pressure, $\mathbf{g}$ is gravity and τ is the stress tensor. These equations are both coupled and non-linear. Solutions for complex flows can be obtained by discretizing the equations, and solving them through an iterative process. For the computer to be able to work with the equations, the computational domain, including the geometry involved, also needs to be discretized. The discrete model of the computational domain is called a grid or a mesh.

There are three steps in solving a CFD problem:

1. Create a grid for the geometry
2. Solve the desired equations using a solver
3. Post process the results

Apart from these steps it is also important to verify and validate the code. Verification of a code is the process of confirming that the code solves the model equations correctly. These results might not be physically correct, but limited by

the model itself. For instance, an inviscid model cannot capture viscous effects, but verification of the code is necessary to ensure that it captures the inviscid effects correctly. Validation of a code is the process of comparing the models results to experimental results, thus confirming (or disconfirming) that the model produces realistic results, i.e. that the code solves the right model equations.

2.2 Boundary layers

All viscous flows near walls develop boundary layers (BL). The boundary layer is defined by Schlichting [31] as the region in a flow close to the wall where the viscosity must be taken into account. A practical definition of an airfoil boundary layer is where the parallel velocity is less than 99% of the free stream velocity, or $u(y) < 0.99U_0$. At the wall, the no-slip boundary condition dictates that $u(y)|_w = 0$, while away from the wall it eventually reaches U_0. The relationship between the viscous stress $\mu\frac{d\overline{u}}{dy}$ and the Reynolds stress $-\rho\overline{u'v'}$, determines the transition process from zero velocity at the wall to free-stream velocity, and thus also the height and shape of the boundary layer. Figure 2.1 gives an example of the relationship between the two stresses, together they make up the shear stress. Near the wall, where the velocity approaches zero the Reynolds stresses also approach zero, and the viscous stresses dominate.

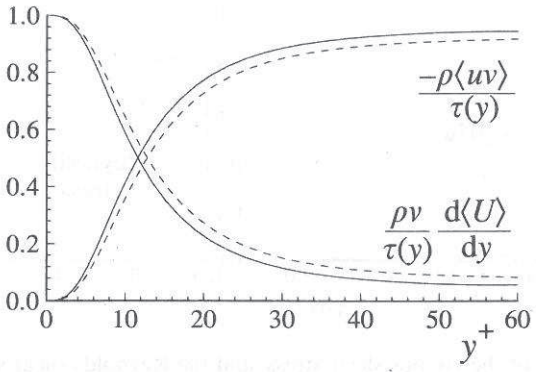

Figure 2.1: Profiles of the fractional contributions of the viscous and Reynolds stresses to the total stress. DNS data of Kim et al. (1987): dashed lines, Re = 5,600; solid lines, Re = 13,750. From Pope [5].

In highly viscous flows (laminar flows) the viscous stresses will dominate over a larger range, and boundary layers will be larger than in low viscous flows (turbulent flows).

2.3 Transition from laminar to turbulent flow

Transition from laminar to turbulent flow is an important phenomenon when considering turbulent flows, especially flow around airfoils. As the low-turbulence incoming flow reaches the airfoil, it slows down as a result of the no-slip condition and a laminar boundary layer is formed. Somewhere along the length of the airfoil,

the boundary layer will usually transform into a turbulent one. The shift from laminar to fully turbulent flow cannot happen instantaneously. Rather, there is a region where the flow is neither laminar nor fully turbulent.

The Reynolds number is an important parameter in determining the transition from laminar to turbulent flow. It is the ratio of inertial to viscous forces, and defined as

$$Re = \frac{UL}{\nu}, \tag{2.3}$$

where U is a characteristic velocity of the system, L is a characteristic length of the system and ν is the dynamic viscosity of the fluid.

As a rule of thumb, laminar flow occurs for low Reynolds numbers, while turbulent flow occurs for high Reynolds numbers. However, there is no universal critical Reynolds number that determines the transition point.

As the laminar flow reaches a certain Reynolds number, $Re_{x,\mathrm{crit}}$, it becomes unstable, and small disturbances in the flow get amplified. As the Reynolds number increases, more and more turbulent structures can be observed in the flow. Eventually the transitional Reynolds number, $Re_{x,\mathrm{tr}}$, is reached, and the flow becomes fully turbulent after this. An illustration of this process is given in figure (2.2).

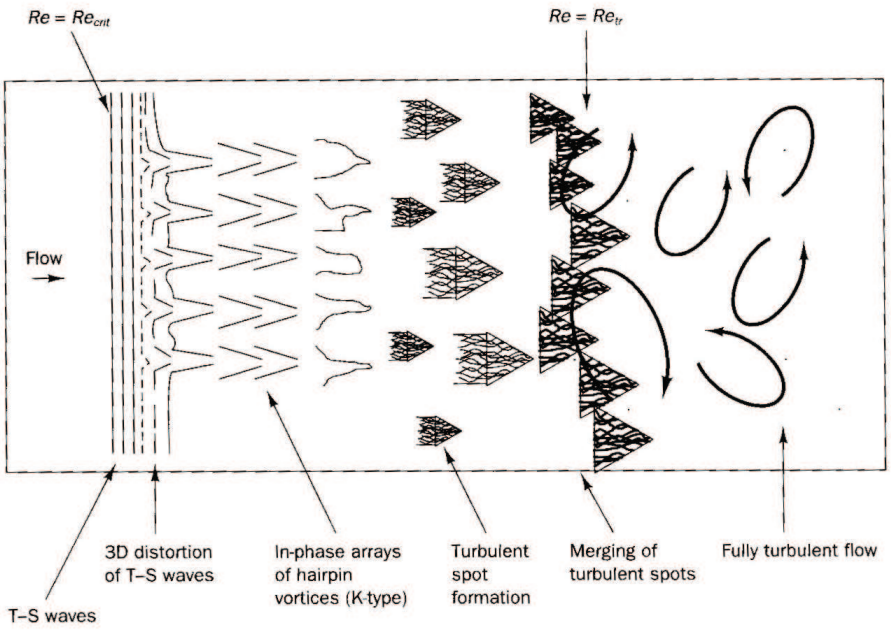

Figure 2.2: Sketch of the transition from laminar to turbulent flow on a flat plate. From Versteeg et al. [6].

Since turbulent flow increases skin friction, due to the high velocity gradients in a turbulent boundary layer, a laminar regime on some parts of the airfoil is desired. Figure 2.3 shows typical laminar and turbulent boundary layers. Laminar boundary layers separates from the wall for smaller adverse pressure gradients than turbulent boundary layers [32]; since turbulent boundary layers have higher kinetic energy than laminar boundary layers. The kinetic energy is used to over-

come the opposing pressure. Flow separation is not desirable on airfoils, due to increased probability of stalling[1].

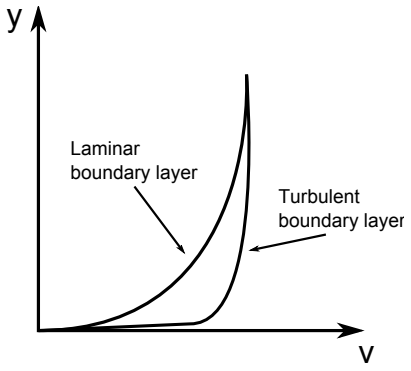

Figure 2.3: Typical laminar and turbulent bounadry layers.

Many turbulence models ignore transition. Thus the flow is modeled as either fully laminar or fully turbulent. Often the transition region is small in comparison to the size of flow domain of interest, and then the errors caused by ignoring transition can become very small. The flow over an airfoil is both laminar and turbulent, and modeling it as fully turbulent could be a significant source of error [32].

2.4 Law of the wall

Flow near walls can be divided into three different layers. An inner layer that is very close to the wall, an outer layer relatively far from the wall and a layer in between. The inner layer is dominated by viscous stresses and the outer layer is dominated by momentum transport due to Reynolds stresses. The relationship between the stresses is illustrated in Figure 2.1.

A velocity profile for a turbulent boundary layer is illustrated in Figure 2.4, where y^+ is the non-dimensional wall normal distance defined as

$$y^+ \equiv \frac{yu_\tau}{\nu}, \tag{2.4}$$

where

$$u_\tau \equiv \sqrt{\frac{\tau_w}{\rho}}, \tag{2.5}$$

is the friction velocity, ν is the kinematic viscocity, τ_w is the wall shear stress and ρ is the fluids density.

The law of the wall is valid in the log layer, with y^+ values approximately between 30 and 500 as given in Figure 2.4. However, the upper limit increases as the Reynolds number increases. The lower limit stays roughly the same for different Reynolds numbers.

Different turbulent models assumes that the first layer of computational cells are either in the log layer or in the viscous layer where $u^+ = y^+$ (and not in

[1] A stall is a reduction in the lift coefficient as the angle of attack increases.

the transition reguion in between). Since the y^+ values are dependent on flow characteristics they are not available during pre-processing. Thus it is important to analyze the y^+ values during post processing in order to control that they correspond with the needs of the turbulent model.

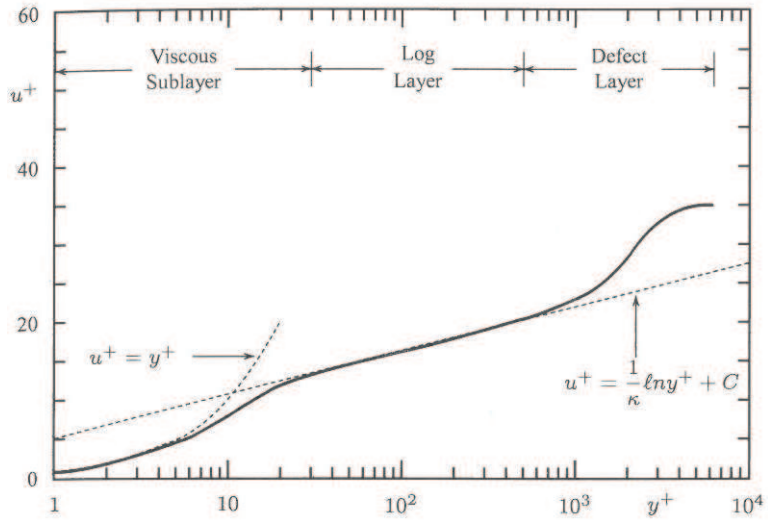

Figure 2.4: Typical velocity profile for a turbulent boundary layer. From Wilcox [7].

2.5 Turbulence modeling

The Transition SST turbulence model [33] was used in the turbulent simulations in this study. This was partly based on previous results by the author for steady RANS computations [34], partly based on results by others [35] and partly based on the Fluent Theory and User's Guide [12, 13]. The Transition SST model was developed by Menter et al. [33]and was introduced in Fluent v.12.0 (2009).

This section gives first a short description of the unsteady Reynolds-averaged Navier-Stokes equations and the Boussinesq approximation before the Transition SST model is presented in the last subsection (Section 2.5.3). Since the Transition SST model is based on the k-ω SST model, which in turn is based on the k-ω model, these models are also briefly discussed in this section.

2.5.1 Unsteady Reynolds-averaged Navier-Stokes (URANS) equations

The unsteady Reynolds-averaged Navier-Stokes equations (URANS) are the ensamble averaged Navier-Stokes equations. Turbulent flows are often described by the URANS for unsteady flows. More accurate descriptions of the turblence can be achieved by the use of large eddy simulations (LES) or direct numerical simulations (DNS), but these models have substantial higher computational demands.

The instantaneous velocity profiles of turbulent flows are not time-independent. In literature the velocity profiles are given as averaged velocity profiles, even

though it is normally not stated. In turbulent flow, the profiles differ significantly from the average profiles, and are usually not smooth, but change drastically in shape both along the wall-normal direction as well as with time. Figure 2.5 illustrates this.

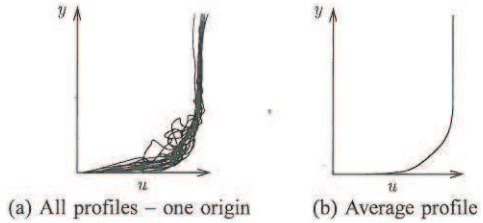

Figure 2.5: Instantaneous and average boyndary layer velocity profiles at the same distance from the leading edge of a flat plate. From Wilcox [7].

Reynolds-decomposition is used to mathematically describe this phenomenon:

$$\phi = \overline{\phi} + \phi'' + \phi, \tag{2.6}$$

where $\overline{\phi}$ is a time mean and the other quantities are given in Figure 2.6. The slow-varying curve with period t_p, also seen in Figure 2.6 may be expressed as a phase average:

$$< \phi >= \overline{\phi} + \phi''. \tag{2.7}$$

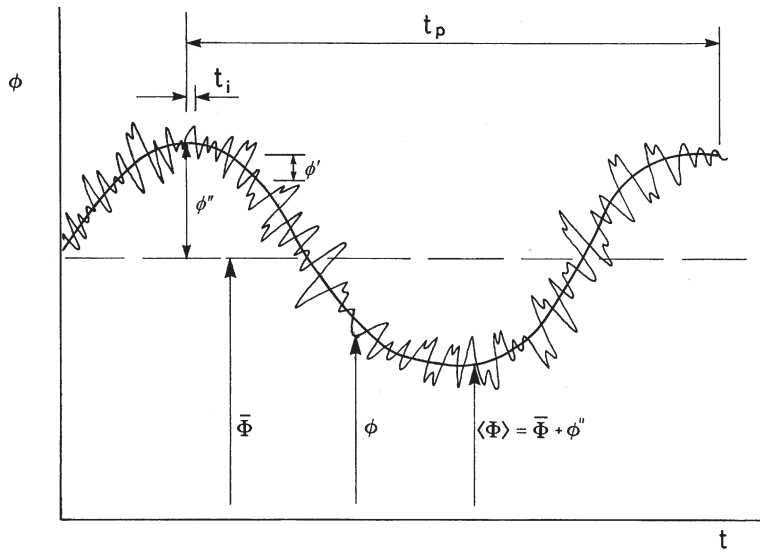

Figure 2.6: Charcteristic trace for the change in a general variable ϕ with time. $\overline{\phi}$ is the mean component, ϕ'' is the periodic component and ϕ' is the turbulent fluctuating component. From Tucker and Pan [8].

In URANS, the velocity components are assumed to vary as described above. The small scale variations are modeled through a turbulence model, while the larger scale variations are solved for in a time-dependent manner. When the fluid is incompressible and gravity is ignored, the equations for conservation of mass

and momentum are (in index notation):

$$\frac{\partial u_i}{\partial x_i} = 0 \tag{2.8}$$

$$\rho\frac{\partial u_i}{\partial t} + \rho u_j\frac{\partial u_i}{\partial x_j} = -\frac{\partial p}{\partial x_i} + \frac{\partial}{\partial x_j}(2\mu s_{ij}), \tag{2.9}$$

where s_{ij} is the strain rate tensor;

$$s_{ij} = \frac{1}{2}\left(\frac{\partial u_i}{\partial x_j} + \frac{\partial u_j}{\partial x_i}\right), \tag{2.10}$$

and $2\mu s_{ij}$ is the viscous stress tensor t_{ij}. Ensamble-averaging and rearranging these equations yields

$$\frac{\partial U_i}{\partial x_i} = 0 \tag{2.11}$$

$$\rho\frac{\partial U_i}{\partial t} + \rho U_j\frac{\partial U_i}{\partial x_j} = -\frac{\partial P}{\partial x_i} + \frac{\partial}{\partial x_j}\left(2\mu S_{ji} - \rho\overline{u_j' u_i'}\right), \tag{2.12}$$

where (2.11) and (2.12) are referred to as the unsteady Reynolds-averaged Navier-Stokes (URANS) equations. In the simplification of Equation (2.12), $\overline{p} = P$ and $\overline{s_{ij}} = S_{ij}$ have been used. Note that all the components are now dependent on both space and time.

The term $\rho\overline{u_j' u_i'}$ is the only term that distinguishes Equation (2.12) from the N-S equations, just with averaged velocities. This term is a time-average rate of momentum transfer due to the turbulence. It describes the complexity of turbulent flow and is the cause of the closure problem (defined below). The specific Reynolds stress tensor is defined as

$$\tau_{ij} \equiv -\rho\overline{u_j' u_i'}, \tag{2.13}$$

and is symmetric ($\tau_{ij} = \tau_{ji}$). The stresses that arise from this term are known as Reynolds-stresses, and they add six more unknowns to the system. With the previous four unknowns, three from the velocity components and one from the pressure, the total number of unknowns for turbulent flow is now ten. Since the number of equations is still only four, the system is not closed. This is referred to as the closure problem.

There are many different approaches to solve the un-closed set of equations, and they define the different turbulence models.

2.5.2 Boussinesq approximation

The Boussinesq eddy-viscosity approximation is the basis for the first-order closure turbulence models. Boussinesq proposed in 1877 that Reynolds stresses might be proportional to mean rates of deformation, i.e.

$$\tau_{ij} = -\rho\overline{u_i' u_j'} = \mu_t\left(\frac{\partial U_i}{\partial x_j} + \frac{\partial U_j}{\partial x_i}\right) - \frac{2}{3}\rho k\delta_{ij}, \tag{2.14}$$

where $k = \frac{1}{2}\sum_{i=1}^{3}\overline{u_i'^2}$ is the turbulent kinetic energy per unit mass and δ_{ij} is the Kronecker delta[2]. The assumption Boussinesq made was to assume that the proportionality constant, the eddy viscosity μ_t was an isotropic and time-independent scalar. For the general case, it would be a fourth rank tensor that could have both spatial and temporal variations, as well as being anisotropic.

The eddy-viscosity models, which all models presented in this study are, model the eddy-viscosity μ_t as a function of a length scale and a velocity scale,

$$\frac{\mu_t}{\rho} = \nu_t = \frac{1}{2} v_0 l_0. \tag{2.15}$$

There are multiple ways of determining the length scale l_0 and the velocity scale v_0, and the different approaches are what separate the different one- and two-equation models. One-equation models are not covered here.

2.5.3 Transition SST model

The Boussinesq approximation (2.14) reduces the number of unknowns from six down to two, K and another flow variable, for two-equation models. The two-equation models that are widely used include one equation for k and a second equation to describe the length scale l_0, or an equivalent variable. Two-equation models are complete, because for the previously given assumptions they provide a full mathematical description of the flow. A summary of the velocity scale, length scale and eddy viscosity as given by the Transition SST model [33] is given in Table 2.1.

Table 2.1: Viscosity and different scales as given by the Transition SST model.

Velocity scale	Length scale	Eddy viscosity
$u_0 = \sqrt{k}$	$l_0 = \frac{\sqrt{k}}{\omega}$	$\nu_t = \frac{k}{\omega}$

The k-ω model, which is the basis for the k-ω SST model and thus also the Transition SST model, was proposed in 1942 by Kolmogorov as the first two-equation model of turbulence. He used dimensional analysis to decide on the specific dissipation ω as the second closure variable. In Fluent, the k-ω model is based on the Wilcox (1998) version (and not the improved Wilcox (2006) version) and the two equations are given as:

$$\frac{D\rho k}{Dt} = \frac{\partial}{\partial x_j}\left(\Gamma_k \frac{\partial k}{\partial x_j}\right) + G_k - Y_k \tag{2.16}$$

and

$$\frac{D\rho \omega}{Dt} = \frac{\partial}{\partial x_j}\left(\Gamma_\omega \frac{\partial \omega}{\partial x_j}\right) + G_\omega - Y_\omega, \tag{2.17}$$

where Γ_k and Γ_ω are the effective diffusivities, G_k represents the generation of turbulence kinetic energy due to mean velocity gradients, G_ω represents the generation of ω, and Y_k and Y_ω represent the dissipation of k and ω, respectively,

[2] $\delta_{ij} = 1$ for $i = j$ and $\delta_{ij} = 0$ otherwise

due to turbulence. The model is suitable for complex boundary layer flows under adverse pressure gradient and separation, as found in external aerodynamics.

The k-ω SST (Shear-stress transport) model was introduced by Menter [36] to improve the standard k-ω model. It uses a blending function to make it behave as a k-ω model in the near-wall region and as a k-ϵ model [12] in the far wake region. Thus it aims to achieve the best of both models. The model is more accurate than the standard k-ω model for a wider class of flows, among them adverse pressure gradient flows, which occur in flow over airfoils. In Fluent the equations are given as:

$$\frac{D\rho k}{Dt} = \frac{\partial}{\partial x_j}\left(\Gamma_k \frac{\partial k}{\partial x_j}\right) + \widetilde{G_k} - Y_k \tag{2.18}$$

and

$$\frac{D\rho \omega}{Dt} = \frac{\partial}{\partial x_j}\left(\Gamma_\omega \frac{\partial \omega}{\partial x_j}\right) + G_\omega - Y_\omega + D_\omega. \tag{2.19}$$

$\widetilde{G_k}$ is similar to G_k, but has a slightly different definition. Notice the addition of a cross-diffusion term D_ω. This term is a result of the blending of the k-ϵ and the k-ω models.

One of the major drawbacks of the two-equation (U)RANS turbulence models is that they model the flow as fully turbulent. For flow over airfoils, a result of this is overprediction of the drag. In order to describe both laminar and turbulent regimes and to accurately predict the onset of transition, additional equations are needed. When the Boussinesq approximation is assumed valid, the additional equations are not required to solve the closure problem (Section 2.5.1). However, the transition models introduce quantities that aim at providing better descriptions of the laminar and laminar to turbulent transition regions.

In the Transition SST model, two new equations are introduced, which are coupled to the original k-ω equations from the k-ω SST model, thus making it a four-equation model. One equation for the intermittency γ and one equation for the transition onset Reynolds number $Re_{\theta t}$ are included. The intermittency determines the triggering of transition, while the $Re_{\theta t}$ equation is included to avoid additional nonlocal operations introduced by the quantities used in the experimental correlations. $Re_{\theta t}$ is treated as a scalar quantity, which lets the experimentally-corrected freestream value of $Re_{\theta t}$ diffuse into the boundary layer. This allows $Re_{\theta t}$ to depend on the local turbulent intensity, and not only the freestream turbulent intensity.

In Fluent, some of the Transition SST model's empirical correlations are slightly altered to improve the predictions of separated flow transition and natural transition. The intermittency function is coupled to the SST turbulence model in Fluent, as follows:

$$\frac{D\rho k}{Dt} = \widetilde{P_k} - \widetilde{D_k} + \frac{\partial}{\partial x_j}\left((\mu + \sigma_k \mu_t)\frac{\partial k}{\partial x_j}\right) \tag{2.20}$$

$$\widetilde{P_k} = \gamma_{eff} P_k \tag{2.21}$$

$$\widetilde{D_k} = \min(\max(\gamma_{eff}, 0.1), 1.0) D_k \tag{2.22}$$

$$\gamma_{eff} = \max(\gamma, \gamma_{sep}), \tag{2.23}$$

where $P_k = \widetilde{G_k}$ and $D_k = Y_k$ are the original production and destruction terms for the SST model and γ_{sep} is a modified value of γ to account for separation-induced transition. This coupling causes γ_{eff} to "turn on" the production term of the turbulent kinetic energy downstream of the transition point.

2.6 Coefficients

The net force acting on an airfoil is normally decomposed into two parts, the lift force, which is perpendicular to the free stream velocity, and the drag force, which is parallel to the free stream flow.

Drag is the sum of pressure forces and viscous forces acting on the airfoil in the direcion of the free stream flow. The viscous forces are always acting in the same direction as the free stream velocity, hence increasing drag. Thrust is defined as negative drag.

Lift is generated due to a pressure difference between the upper and lower side of an airfoil. The pressure is lower on the suction (normally upper) side, than on the pressure (lower) side.

For flapping airfoils, lift is both desired and undesired. A net lift is needed to keep the airfoil body from falling to the ground, when gravity is taken into account. While at the same time the lift tends to act in the direction opposite of the flapping motion, thus increasing the energy required to perform the motion. This energy demand is expressed as the input power coefficient C_{Power}, defined below.

Both lift and thrust can be non-dimensionalized into lift and thrust coefficients:

$$C_L = \frac{L}{\frac{1}{2}\rho U_0^2 C} \text{ and } \quad C_T = \frac{-D}{\frac{1}{2}\rho U_0^2 C}, \tag{2.24}$$

where L and D are the lift and drag forces per unit length in the spanwise z-direction, respectively, ρ is the fluid density, U_0 is the free stream velocity and C is the chord length. C_{Power} is defined as

$$C_{\text{Power}} = \frac{-C_L \dot{y}}{U_0}, \tag{2.25}$$

the negative sign is needed since the lift force acts in the direction opposite of the flapping motion, as stated earlier.

All three coefficients are time-dependent, and mean values can be calculated. The mean lift coefficient is not investigated in this study. The mean for C_T is defined as:

$$C_{T\text{mean}} = \frac{1}{T}\int_t^{t+T} C_T(t)\,\mathrm{d}t, \tag{2.26}$$

where T is the oscillation period and t is time. Similar definitions yield for the other coefficients.

The propulsive efficiency η is defined as

$$\eta = \frac{C_{T\text{mean}}}{C_{\text{Power-mean}}}, \tag{2.27}$$

and is a measure of how much of the energy put into the airfoil motion is converted into thrust. $\eta = 1$ means there are no losses, while $\eta \leq 0$ means no thrust is generated.

2.7 Flapping motion

Flapping motion can be either pure oscillating, pure pitching or a combination of these. These three modes are illustrated in Figure 2.7. Birds and insects use the combination mode, which indicates that this mode is the most efficient for flight and provides the highest propulsive efficiency, this has also been confirmed through experiments and numerical simulations [18]. However, this study limits itself to pure oscillating motion in order to limit its scope.

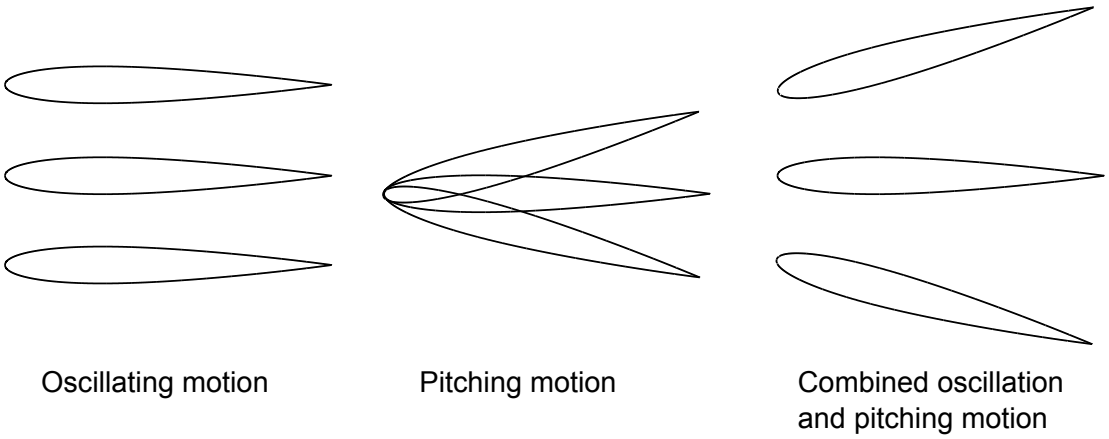

Figure 2.7: An illustration of three different modes of flapping motion. Snapshots of the moving airfoil are superimposed on each other.

In the literature regarding flapping airfoils an oscillating motion is sometimes referred to as a plunging motion. This report uses mostly the term oscillating motion, while plunging is used in the term plunge velocity, which refers to the maximum velocity reached during an oscillation motion.

The remaining sections in this chapter cover some theory related to airfoils in oscillating motion.

2.8 Strouhal number

The Strouhal number was defined in Section 1.2, the definition is repeated here for clarity:

$$Sr = \frac{fA}{U_0}, \tag{2.28}$$

where f is the oscillation frequency, A is a characteristic length and U_0 is the free stream velocity. The Strouhal number describes the oscillating motion of a flapping airfoil. When not considering oscillating airfoils, the length A is taken to be the wake width [37]. However, since this value is unknown before measurements

are made, A is taken to be equal to double the heave amplitude [38]:

$$Sr = \frac{2fa}{U_0}, \tag{2.29}$$

where a is the amplitude of the airfoil motion.

The Strouhal number is closely related to the maximum value of the oscillating velocity which equals ωa, where $\omega = 2\pi f$ is the oscillation frequency. This leads to

$$Sr = \frac{2fa}{U_0} = \frac{2\pi fa}{\pi U_0} = \frac{\omega a}{\pi U_0}, \tag{2.30}$$

and thus the Strouhal number can be seen as a measure of the non-dimensional plunge velocity.

Another often used parameter is the reduced frequency k, defined as:

$$k = \frac{\pi fC}{U_0}, \tag{2.31}$$

where C is the airfoil chord length.[3] With h being the non-dimensional amplitude of oscillation, the product kh is another way of expressing the Strouhal number:

$$Sr = \frac{2}{\pi}kh. \tag{2.32}$$

2.9 Vortex shedding

As early as 1908, Bénard [39] sketched the alternate shedding of vortices behind a circular cylinder. Flow around circular cylinders have been thoroughly investigated after that first observation in 1908 (cf. Zdravkovich [9] or Williamson [40] for reviews). Although this current study is on airfoils, which are normally not bluff bodies[4], theory about vortex shedding behind cylinders is first reviewed, and then comparisons are made to vortex shedding from stationary airfoils and flapping airfoils.

For Reynolds numbers above a critical value (dependent on the shape of the body/airfoil) the instabilities in the near wake region cause oscillations downstream of the body. As seen in Figure 2.8 the wavelength of the wake decreases as the Reynolds number increases. Simultaneously the amplitude of the crests and troughs [5] increases. Eventually this leads to a roll up of the free shear layer at the crests and troughs, and vortices are produced. In literature, the downstream traveling vortices are referred to as a Kármán vortex street.

As the vortices travel downstream, they increase somewhat in diameter. This is due to entrainment of flow particles that was not originally part of the Kármán vortex street, this flow will be referred to as external flow. The process is visualized in Figure 2.9, where the smoke that is released above and below the Kármán vortex street is eventually fully entrained into the vortices.

[3] Sometimes k is defined as $k = \frac{2\pi fc}{U_0}$, but that convention is not used in this study.

[4] However, at high enough angles of attack or high enough Reynolds numbers airfoils will behave as bluff bodies. The latter is explained by the increase in displacement thickness, which causes the apparent size of the airfoil to increase

[5] The crest being the highest point in a wave, and the trough being the lowest.

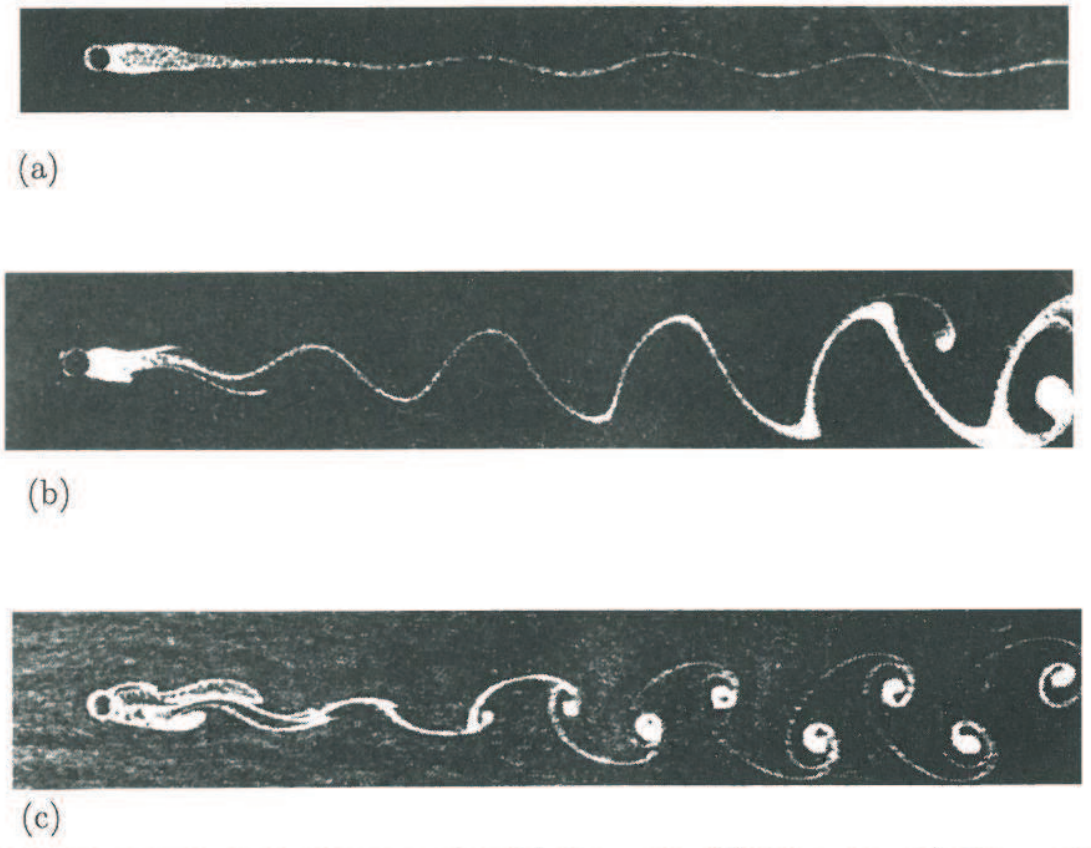

Figure 2.8: Periodic laminar wake behind a cylinder: (a) Re = 54, (b) Re = 65, (c) Re = 102. From Zdravkovich [9]

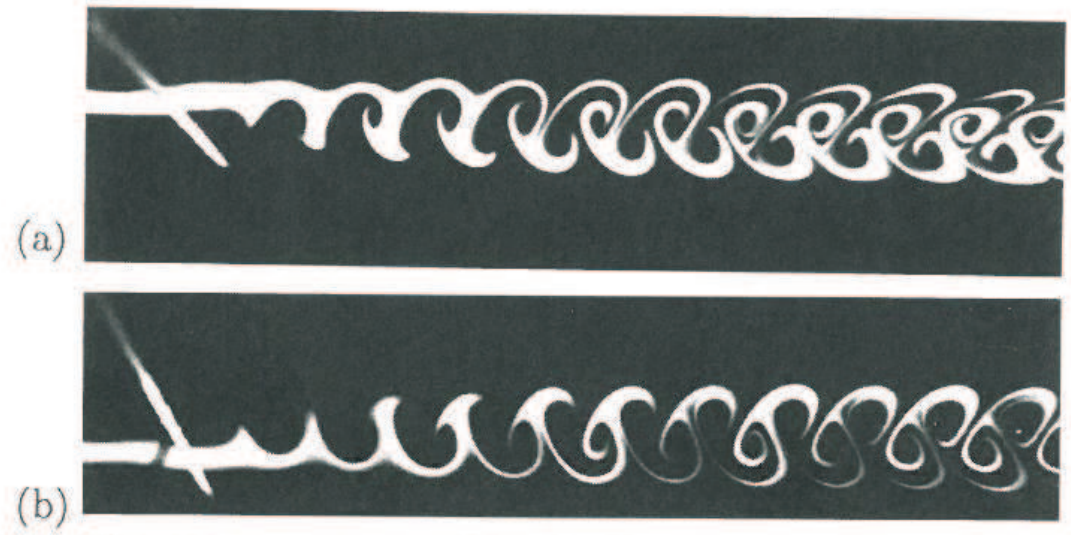

Figure 2.9: Entrainment across Kármán eddy street at Re = 100. (a) Smoke streakline released above the cylinder. (b) Smoke streakline released below the cylinder. From Zdravkovich [9]

The vortices are not shed directly from the cylinder in Figure 2.8, but are formed in the wake behind it. This mode of vortex shedding is referred to as low-speed mode [9]. The high speed mode of vortex shedding occurs for higher Reynolds numbers. Both modes are described below.

- Low speed mode, Figure 2.8. Vortices are formed in the wake, and caused by instabilities in the wake. They are formed by the roll up of free shear layers at crests and troughs of the oscillating wake. As the vortices travel downstream they grow in size because of entrainment by external flow.

- High speed mode, Figure 2.10. Vortices are formed and shed at the body. They grow to their maximum size at an almost fixed position. As the vortices travel downstream they diffuse and decay.

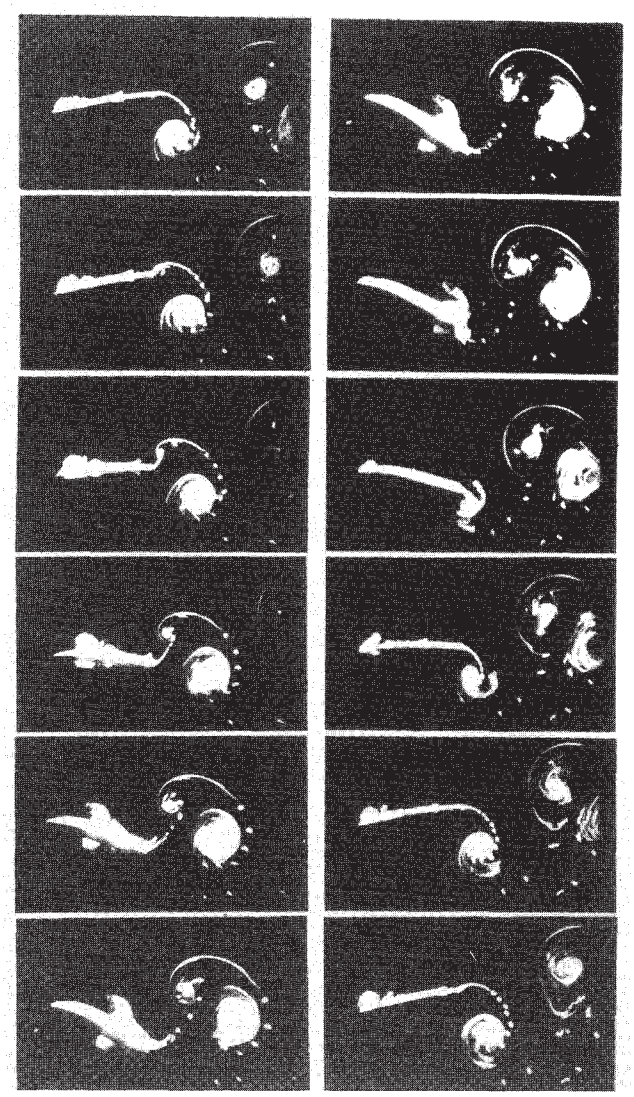

Figure 2.10: Airfoil in pure pitching motion around the $C/4$ chord axis, $Re = 12,000$. The sequence starts at the upper left, then continues downwards column by column. From Freymuth [10].

An important difference between these two modes is the way they entrain particles from the external flow. In the high speed mode the vortices are strong enough that they pull the shear layer across the wake, which cuts off the consecutive downstream vortex from supply of circulation and cuts off the streakline between them. In the low speed mode, the vortices are not as strong, and a streakline will connect all the vortices in the Kármán street. These phenomena may be seen in Figures 2.8 and 2.10. In Figure 2.10 a vortex in the upper row starts to become visible in the fourth frame. When it has reached its maximum size in the last frame, it has hardly moved downstream. There is also no streakline connecting it to the subsequent vortex in the last frame.

Vortex shedding for an airfoil will be discussed in the two following subsections.

2.9.1 Trailing edge vortex shedding

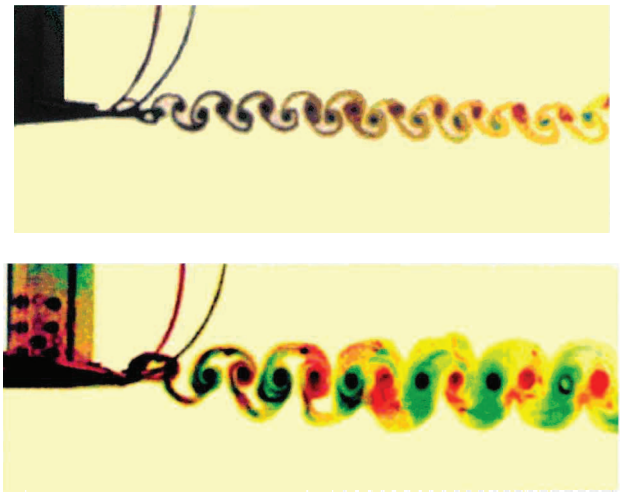

Figure 2.11: Vortex shedding for a stationary (upper frame) and oscillating at $Sr = 0.196$ and $k = 0.164$ (lower frame) NACA 0012 airfoil at $Re = 20,000$. From Lai and Platzer [11].

Despite the streamline shape of an airfoil, vortex shedding will still occur at the trailing edge for high enough Reynolds numbers. This may be seen in the upper frame of Figure 2.11 for a stationary airfoil and in the lower frame of Figure 2.11 for an oscillating airfoil, both for laminar flow. There are two indicators that this particular vortex shedding is of the low speed mode. The first indicator is that the streaklines connect the vortices, which implies that the vortex strength is too low to pull the shear layer across the wake. The second indicator is that the vortices grow in size, most notably in the beginning of the wake.

2.9.2 Leading edge vortex (LEV) shedding

Vortices can also be shed from the leading edge for flapping airfoils. The occurrence of leading edge vortex shedding is dependent on both the oscillation frequency and amplitude.

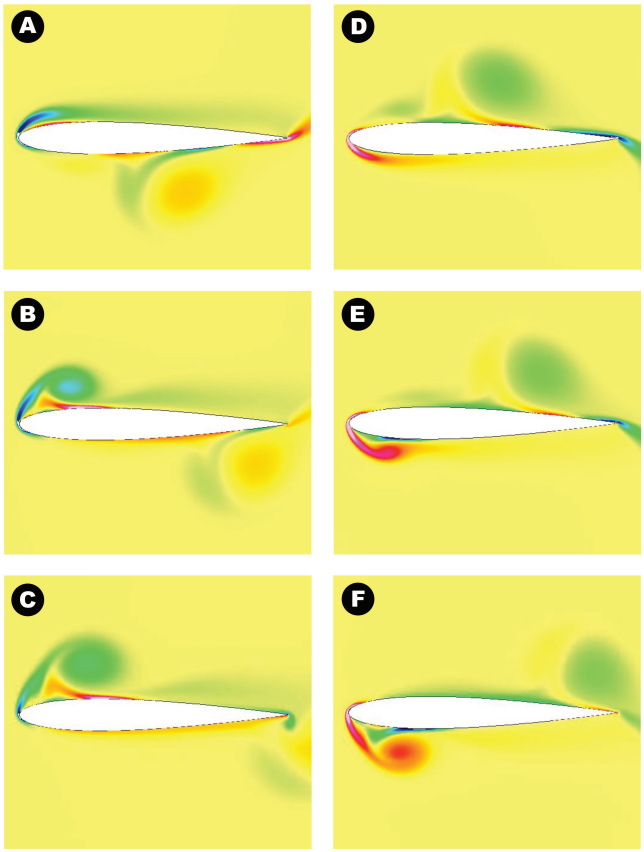

Figure 2.12: Leading edge vortex shedding for an airfoil in pure plunging motion during a downstroke. Sequence follows letters. From Guerrero [2].

For a given oscillation amplitude the oscillation frequency needs to be high enough so that the airfoil velocity perpendicular to the free stream is comparable to that of the free stream velocity. This will produce a high effective angle of attack, which causes the incoming flow to effectively see a bluff body (the nose of the airfoil can almost be modeled by a semi circle). If the oscillation frequency is too high, there will not be enough time for a vortex to form during one upward or downward stroke of the airfoil. Also, the oscillation amplitude needs to be high enough to allow for enough time for a vortex to form during one stroke.

The leading edge vortex shedding cannot be directly compared to the vortex shedding of a bluff body. There is usually only time for one vortex (if any) to form during each stroke and multiple vortices are needed to form a Kármán street. Also, the airfoil's body interacts with the vortex, so it will not travel downstream uninterrupted.

However, a few key comparisons can still be made. They are both related to the shedding mode resembling that of high speed vortex shedding. As may be seen in Figure 2.12 frames B and C, where the vortex grows to its final size almost without moving downstream. The other important feature is that the vortex does not grow, but instead it decays after it has started moving downstream. The free stream velocity determines the speed at which the vortex moves downstream.

The vortices will also interact with the Kármán vortex street from the trailing edge, if they have not decayed before they have moved past the airfoil.

2.9.3 The impact of vortex shedding on airfoil performance

A simple explanation for the generation of thrust by a flapping airfoil is based on the effective angle of attack the airfoil experiences as it moves perpendicularly to the incoming flow. A visualization of this may be seen in Figure 1.1 on page 2. When the airfoil moves in the opposite direction, the force vector will also point in the opposite direction, but it will still have a thrust generating component. For low plunge velocities, the effective angle of attack can be too low to generate a net thrust; viscous drag forces dominates.

For a better understanding of the flow and the physics involved, a more thorough investigation of the wake is needed. Although many complex wake structures exist, this section will focus on the most basic ones to explain how they relate to thrust and drag. These basic wakes are the Kármán vortex street (drag indicating), reverse Kármán vortex street (thrust indicating) and the neutral wake.

The drag indicating Kármán street will be generated for either a stationary airfoil or one with low plunging velocity (or Strouhal number), a visualization may be seen in Figure 1.4 on page 4. In this mode there are two rows of vortices, an upper and a lower. The vortices in the upper row rotate clockwise, while the vortices in the lower row rotate counterclockwise. This results in a velocity/momentum deficit in the middle of the wake, as compared to the free stream velocity. Parts of this momentum have been transferred to the airfoil, and is experienced as drag.

The thrust indicating reverse Kármán street will be generated for oscillating airfoils of sufficiently high Strouhal number; a visualization may be seen in Figure 1.5 on page 5. In this mode the vortices in the upper row rotate counterclockwise, while the vortices in the lower row rotate counterclockwise, which is the opposite of the drag producing wake. This results in a velocity/momentum excess in the middle of the wake. The wake now resembles a jet, whith a momentum excess in the middle of the wake.

In a small range of Strouhal numbers between the drag and the thrust indicating wakes, a neutral wake exists; a visualization may be seen in Figure 2.13. In this mode the two rows of vortices are aligned behind the airfoil and there is neither velocity/momentum deficit nor excess present.

One way of identifying the different wakes is to look at the way the mushroom-like shapes in the wake are tilted. For a drag producing wake the mushrooms are tilted upstream, for a thrust producing wake the mushrooms are tilted downstream and for a neutral wake the mushrooms are not tilted.

It should be noted that more complex wake structures exist which may be either drag producing, thrust producing or neutral.

For leading edge vortex shedding and its effect on airfoil performance, there are mainly two effects to consider: The change in pressure caused by the vortices as well as interaction with the trailing edge vortex shedding.

The low pressure in the vortex causes the leading edge vortex to increase both lift and thrust while it is in front of the thickest part of the airfoil. This is because the resulting force vector points normal to the airfoil surface, which points upwards and upstream. When the vortex is behind the thickest part of the airfoil, it increases both lift and drag on the airfoil. In this situation the normal

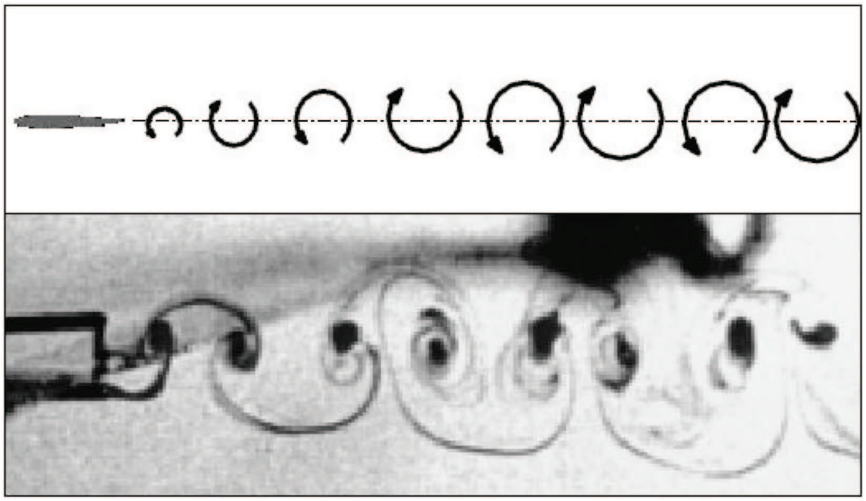

Figure 2.13: Neutral vortex street. From Jones et al. [3]

vector points upwards and downstream. An illustration of this may be seen in Figure 2.14. Because of this phenomenon, it is of much interest how fast the vortices decay, since these forces will greatly affect the airfoils performance.

The vortices may or may not progress past the trailing edge, and if they do they can greatly affect the vortices shed from the trailing edge as well as the wake in general.

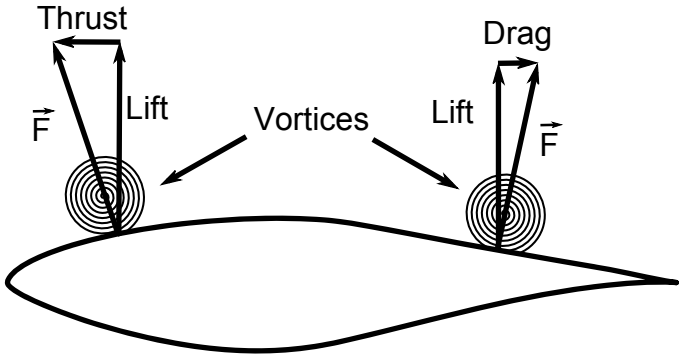

Figure 2.14: Forces generated by vortices on airfoils. The figure shows an S809 airfoil.

Chapter 3

Numerical methods

To achieve an accurate solution in CFD simulations it is not only important to have a good quality grid, but the choices of the numerical methods are also crucial. For this study the Ansys Fluent Version 13.0.0 software was used as the numerical solver, which allows for a wide set of parameters to be set by the user. This section covers both some theory behind the solver and different parameters, as well as arguments for parameter settings used. Many parameters were left at their default values, because in most cases they were not critical for this study and the default values were considered acceptable. In a few cases they were not properly investigated due to time limitations.

3.1 The finite volume method

There are different methods to convert the governing equations for fluid flow into discretized versions, most notably are the finite difference, the finite volume and the finite element methods. Fluent uses the finite volume method, and a short description is given here. The finite volume method involves discretization of the integral form of the Navier-Stokes equations. This results in discretized equations which a computer can handle. The key step of the method is the control volume integration, where a partial differential equation is integrated over a volume. Consider the convection-diffusion problem for a property ϕ

$$\frac{d}{dx}\left(\rho u \phi\right) = \frac{d}{dx}\left(\Gamma \frac{d\phi}{dx}\right), \tag{3.1}$$

where ρ is the fluid's density, u is the fluid's velocity and Γ is the diffusion coefficient. The left hand side in the equation is the convection term and the right hand side is the diffusion term. When integration over a control volume is performed, the equation becomes

$$\int_{CV} \frac{d}{dx}\left(\rho u \phi\right) \, \mathrm{d}V = \int_{CV} \frac{d}{dx}\left(\Gamma \frac{d\phi}{dx}\right) \, \mathrm{d}V \tag{3.2}$$

The above relation is true for an arbitrary control volume CV. Let the CV become the discrete 1D volume as shown in Figure 3.1. To get a discretized

equation the volume integrals need to be converted into surface integrals using the divergence theorem, $\int_V \boldsymbol{\nabla}\cdot\mathbf{F}\,\mathrm{d}V = \int_A \mathbf{n}\cdot F\,\mathrm{d}A$:

$$\begin{array}{rcl} \int_{\Delta V} \frac{d}{dx}\left(\rho u\phi\right)\,\mathrm{d}V & = & \int_{\Delta V} \frac{d}{dx}\left(\Gamma\frac{d\phi}{dx}\right)\,\mathrm{d}V \\ \left(\rho uA\phi\right)_e - \left(\rho uA\phi\right)_w & = & \left(\Gamma A\frac{d\phi}{dx}\right)_e - \left(\Gamma A\frac{d\phi}{dx}\right)_w \\ \left(\rho u\phi\right)_e - \left(\rho u\phi\right)_w & = & \left(\Gamma\frac{d\phi}{dx}\right)_e - \left(\Gamma\frac{d\phi}{dx}\right)_w, \end{array} \tag{3.3}$$

where the cross-sectional area of the control volume face, A, cancels in the last step and e and w are the east and west faces of the CV, as depicted in Figure 3.1. This equation has now a clear interpretation: The difference in the diffusive flux of ϕ between the east and west faces equals the difference in the convective transport of ϕ between the east and west faces. A similar interpretation yields for the convective mass flux per unit area, ρu. The finite volume method can be expanded to two and three dimensions using a similar approach.

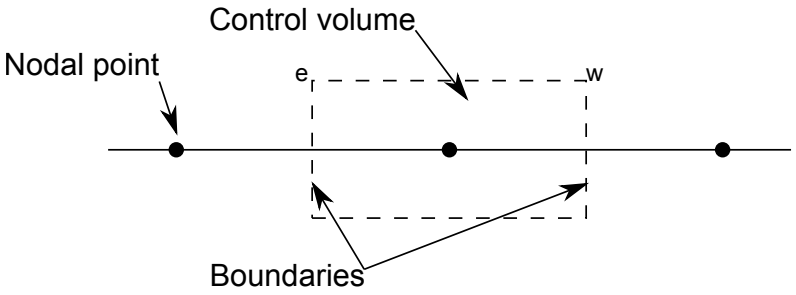

Figure 3.1: A one dimensional control volume. The east and west boundaries are marked by e and w, respectively.

3.2 General solver settings

Fluent has the option of being a density based or a pressure based solver. The default pressure based solver is used for all calculations in this study. In the pressure based solver a pressure equation is derived from the continuity and the momentum equations. This equation is solved to achieve the constraint of continuity. The steps taken in the pressure based solver are shown in Figure 3.2

The Reynolds numbers investigated in this study were $20,000$ and $3,000,000$, for the laminar flow and turbulent flow, respectively. These numbers were determined by the data used for validation and verification, which were generated at these Reynolds numbers. The fluid material was modeled as air, using default settings in Fluent. Table 3.1 gives an overview of material properties and other reference values.

3.2.1 Under-relaxation factors

Under-relaxation factors (URF) are factors that determine how big changes for the flow properties the solver takes in each iteration. For a variable ϕ the new value is given by

$$\phi = \phi_{\text{old}} + \beta\Delta\phi, \tag{3.4}$$

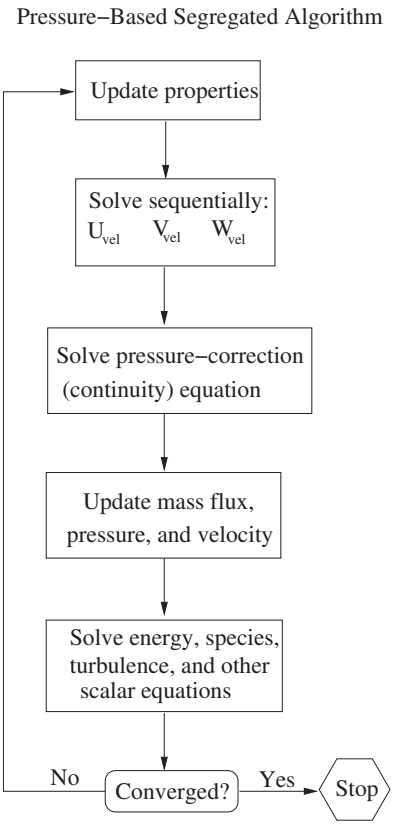

Figure 3.2: Overview of the steps taken in the pressure based solver.

Table 3.1: Reference values used in Fluent. The chord length determines the reference length and the inlet velocity determines the reference velocity. The density and viscosity are default material property values for air, given by Fluent

Reference values	
Length	1 m
Laminar velocity	0.29 $^{m}/_{s}$
Turbulent velocity	43.82 $^{m}/_{s}$
Density	1.225 $^{kg}/_{m^3}$
Dynamic viscosity	$1.7894 \cdot 10^{-5}$ $^{kg}/_{ms}$

where β is the under-relaxation factor and $\Delta\phi$ is the computed change in ϕ.

Too large increments in solution properties can sometimes cause divergence, and setting the URFs lower can thus aid in achieving convergence. For all of the laminar simulations the URFs were kept at their default values. For some of the turbulent simulations, the URFs were reduced in order to achieve a converged solution. The URF values do not in general affect the accuracy of the solution, but lower values require in general more iterations to arrive at the same solution. Since this study uses a limit on 20 iterations per time step, changes in the URFs might cause changes in the solution. Especially since the limit of 20 iterations is reached in almost all of the simulations performed in this study. Time constraints did not permit an investigation of the effects of changes in the URFs. The values used for the URFs are given in Table 3.2.

Table 3.2: Under-Relaxation Factors (URF) used in the study.

	Laminar simulations	Turbulent simulations	Reduced URFs
Pressure	0.3	0.3	0.2
Density	1	1	1
Body Forces	1	1	1
Momentum	0.7	0.7	0.5
Turbulent Kinetic Energy	N/A	0.8	0.5
Specific Dissipation Rate	N/A	0.8	0.5
Intermittency	N/A	0.8	0.8
Momentum Thickness Re	N/A	0.8	0.8
Turbulent Viscosity	N/A	1	0.8

3.3 Boundary conditions

Boundary conditions (BC) dictate the flow in the far-field regions as well as on the airfoils surfaces. Not all the BCs could be determined by data from either experiments or other comparable numerical simulations, and most of these conditions were left at their default values.

Since there were no symmetry or periodicity involved in this study, the BCs in the far-field regions (the outer boundaries of the computational domain) were set either as velocity-inlets or pressure-outlets.

The inlet velocity at the west face, upstream of the airfoils, was set at a constant magnitude, determined by the different Reynolds numbers. For the laminar simulations of Reynolds number of $10,000$, the inlet velocity was set to 0.29 $^{\mathrm{m}}/_{\mathrm{s}}$. For the turbulent simulations of Reynolds number of $3,000,000$, the inlet velocity was set to 43.82 $^{\mathrm{m}}/_{\mathrm{s}}$.

All other faces in the far-field regions were set as pressure outlets. This includes the edges that are created due to the relative motion between the two grid regions, as explained in Section 4.6.2. The backflow velocity directions were determined by the neighboring cells, in order to avoid as much as possible imposing external constraints on the flow when the grid is sliding.

The inlet turbulence was determined by a turbulent intensity (TI) of 1 %, a turbulence length scale of 1 m and an intermittency value of 1. TI of 10% or above is considered high, while modern wind tunnels may have values as low as 0.05 % [13]. The turbulence length scale is a physical quantity related to the size of the large eddies that contain the energy in turbulent flows. It is believed to be of the same order of magnitude as the length of the airfoils, which have chord lengths of 1 m. The intermittency value was kept at the default level of 1.

The conditions for turbulence levels for backflow were set to the same values as those for inlet turbulence.

No data for wall roughness from either the experimental or computational data used for comparison was available, and wall roughness was set to zero. The no-slip condition was assigned to the airfoil surfaces.

3.4 Spatial discretization

In the finite volume method property values are normally stored at the nodal points. An interpolation is then required to establish values at the faces (see Figure 3.3 for an illustrates.) The second order upwind scheme was used for all convection terms in the solution equations: Momentum, turbulent kinetic energy, specific dissipation rate, intermittency and momentum thickness.

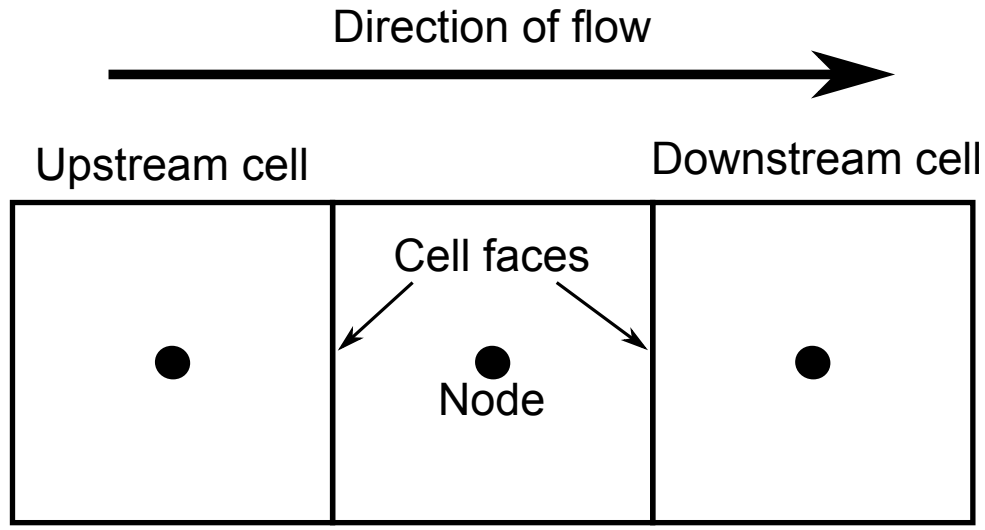

Figure 3.3: Illustration of nodal points, cell faces and upstream and downstream cells.

Information travels mostly in the direction of the flow, and a scheme that uses information from cells upstream of the cell in question, is preferred [6]. The upwind scheme uses node values of upwind cells for face values of the cell in question. Since the cells that are upstream vary with the direction of the flow, the nodes that determine the face value of the cell in question change with the direction of the flow.

The second order upwind scheme in Fluent uses a multidimensional linear reconstruction approach for quantities at cell faces [12]. The face value ϕ_f is

given by

$$\phi_f = \phi + \nabla\phi \cdot \mathbf{r}, \tag{3.5}$$

where ϕ is the node value of the upstream cell, $\nabla\phi$ is its gradient and $\mathbf{r}$ is the displacement vector from the node of the upstream cell to the face centroid.

Other discretization schemes were available, such as the QUICK scheme and Third-Order MUSCL scheme. These schemes were not investigated, as they will in general not provide significant improvements in accuracy [13]

3.4.1 Gradient scheme

Fluent has three options for evaluation of gradients and derivatives:

- Green-Gauss Cell-Based
- Green-Gauss Node-Based
- Least Squares Cell-Based

Both the Green-Gauss Node-Based and the Least Squares Cell-Based methods are superior in accuracy compared to the Green-Gauss Cell-Based method [12]. On irregular grids, the accuracy of the Least Squares Cell-Based method is comparable to that of the Green-Gauss Node-Based method, however the Least Squares Cell-Based method is faster to compute. Since parts of the grid will be irregular and computational time was an issue due to the many simulations required for this study, the Least Squares Cell-Based method was applied.

The Least Squares Cell-Based method assumes that the solution varies linearly. The method expresses the change in cell values between cell $c0$ and ci as

$$(\nabla\phi)_{c0} \cdot \Delta\mathbf{r_i} = (\phi_{ci} - \phi_{c0}), \tag{3.6}$$

where $c0$, ci and r_i are illustrated in Figure 3.4.

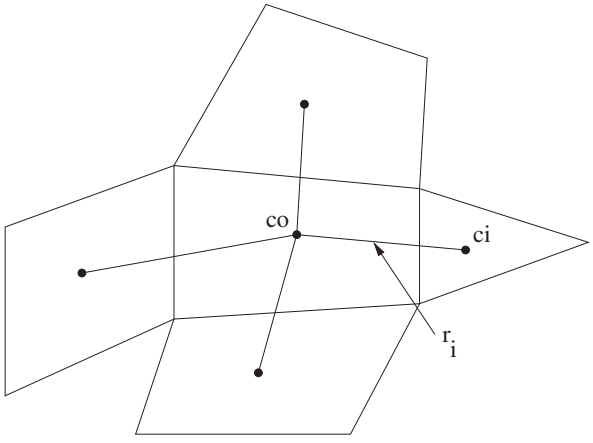

Figure 3.4: Schematic for the least squares cell-based gradient evaluation. From Fluent Theory Guide [12].

Equations are set up for all neighboring cells, and the resulting matrix is solved by solving the minimization problem for the system of the non-square coefficient matrix in a least squares sense.

3.4.2 Pressure interpolation scheme

Fluent offers five choices for the pressure interpolation scheme:

- Standard
- Linear
- Second order
- Body force weighted
- PRESTO! (PREssure STaggering Option)

The standard (default) scheme interpolates the pressure values at the faces using momentum equation coefficients [41]. The linear scheme computes the face pressure as the average of the pressure values in the adjacent cells. The second order, body force weighted and PRESTO! schemes are all more accurate than the linear and standard schemes. The body force weighted scheme works well if the body forces are known a priori and The PRESTO! scheme is well suited for flows with steep pressure gradients [12]. In this study the PRESTO! scheme was used. This scheme uses the discrete continuity balance for a staggered control volume about the face to compute the staggered pressure. This procedure is similar to the staggered-grid schemes used with strucutered grids.

3.5 Pressure velocity coupling

The solver, Fluent in this case, solves the continuity equation (2.1) and the momentum equations (2.2). Each of the velocity components has its own transport equation, and the velocity component also need to satisfy the continuity equation. The equations (2.1) and (2.2) are highly non-linear and intricately coupled. Thus there is no simple analytical solution. If the pressure is known, the momentum equations for u and v can be used to solve for the velocities. But it does not imply that continuity is satisfied, and the continuity equation cannot be used to solve for the pressure. To solve this problem, a pressure-velocity scheme is required.

In Fluent there are four different methods for the pressure velocity coupling, three segregated types: SIMPLE, SIMPLEC and PISO (Pressure-Implicit with Splitting of Operators) and one coupled method. The PISO method was used in this study.

The coupled algorithm was not used because it results in slower convergence. SIMPLEC and PISO are both modified versions of the SIMPLE algorithm. Detailed descriptions of all three models may be found in Versteeg and Malalasekera [6]. Only an outline of SIMPLE is given here. The SIMPLE algorithm consits of the following steps:

1. Start with initial values
2. Solve momentum equations to get u and v
3. Solve pressure correction equation, $p = p^* + p'$

4. Calculate correction terms p', u' and v'
5. Correct P, u and v
6. Repeat until solution has converged

Where in the third step p is the correct pressure, p' is the pressure correction term and p^* is the guessed pressure. u' and v' are the components of the velocity correction. To improve the efficiency of the SIMPLE method, the PISO algorithm performs two additional corrections: neighbor correction and skewness correction.

The neighbor correction (or momentum correction) involves moving the repeated calculation required by SIMPLE inside the solution stage of the pressure-correction equation. The skewness correction involves recalculating the pressure-correction gradient after the solution of the pressure-correction equation. This helps with convergence in skewed cells since the approximate relationship between the correction of mass flux at the cell face and the difference of the pressure-correction gradient along the cell faces are not known in advance.

The PISO algorithm is highly recommended for transient simulations [13] and the grids in this study had some degrees of skewness to them, which made PISO the preferred pressure-velocity coupling algorithm.

3.6 Time dependent calculations

The integral form of the transport equation for a variable ϕ takes the following form for time-dependent flows:

$$\int_V \frac{\partial \rho\phi}{\partial t}\,\mathrm{d}V + \oint \rho\phi\mathbf{v}\cdot\,\mathrm{d}\mathbf{A} = \oint \Gamma_\phi \boldsymbol{\nabla}\phi\cdot\,\mathrm{d}\mathbf{A} + \int_V S_\phi\,\mathrm{d}V, \tag{3.7}$$

where ρ is density of the fluid, $\mathbf{v}$ is velocity vector, $\mathbf{A}$ is surface area vector, Γ_ϕ is diffusion coefficient for ϕ, $\boldsymbol{\nabla}\phi$ is gradient of ϕ and S_ϕ is source of ϕ per unit volume. When using the pressure-based solver in Fluent, the value of ϕ at the next time step is evaluated through an implicit discretization of Equation 3.7:

$$\int_V \frac{\partial \rho\phi}{\partial t}\,\mathrm{d}V + \oint \rho^{n+1}\phi^{n+1}\mathbf{v}^{n+1}\cdot\,\mathrm{d}\mathbf{A} = \oint \Gamma_\phi^{n+1} \boldsymbol{\nabla}\phi^{n+1}\cdot\,\mathrm{d}\mathbf{A} + \int_V S_\phi^{n+1}\,\mathrm{d}V, \tag{3.8}$$

where $n+1$ indicates the next time level.

There are two sources of error related to the time-discretization: the choice of temporal discretization and the time-advancement scheme. The temporal discretization is described in Section 3.6.1 while a short description of the time advancement scheme is given here.

A splitting error is introduced due to the solving of equations one by one by the segregated solver. Fluent offers two time-advancement schemes that handle the splitting error differently.

In the iterative time-advancement scheme, all the equations are solved iteratively for a given time-step until the convergence criteria are met. A constraint on the number of iterations per time-step might deny the solver to reach the convergence criteria for a given time-step, this was often the case in this study, which

had a limit of 20 iterations per time-step. The non-linearity of the equations are fully accounted for, and splitting error is eliminated if enough iterations are performed. An overview of the scheme is given in Figure 3.5.

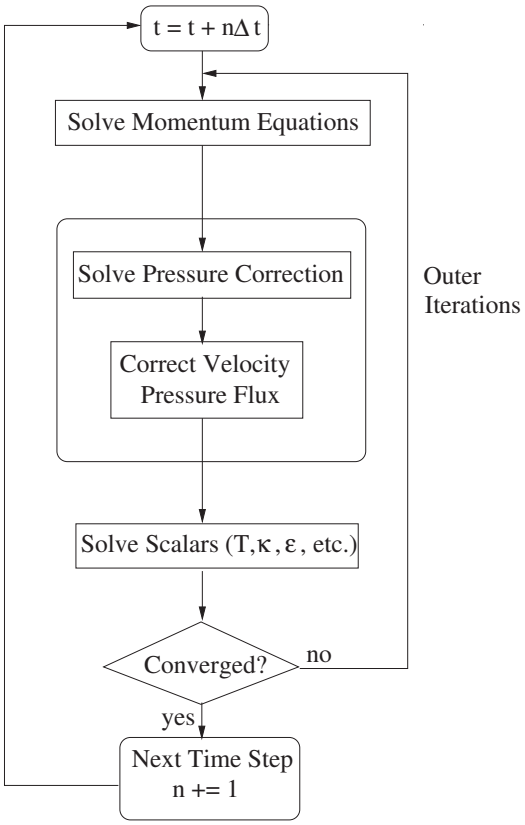

Figure 3.5: Overview of the steps taken in the iterative time advancement scheme.

The non-iterative time-advancement scheme (NITA) performs only a single outer iteration per time-step. Even though inner iterations may be performed for each of the individual sets of equations, the computational demand is significantly lowered, as compared to the iterative time-advancement scheme. It was not believed that NITA would provide the same level of accuracy as the iterative time-advancement scheme. A few cases were run with both schemes, and as NITA proved to have convergence difficulties. Therefore, the iterative time-advancement scheme was used in this study.

3.6.1 Temporal discretization

The second order backward differentiation formula implicit time scheme was used in this study. A short description of this scheme is given in this section.

Temporal discretization involves the integration of every term in the integral equations, like Equation 3.8 over a time step Δt. The time evolution of a variable ϕ is given by

$$\frac{\partial \phi}{\partial t} = F(\phi), \tag{3.9}$$

where the function F incorporates any spatial discretization. In Fluent, the second-order discretization is given by

$$\frac{3\phi^{n+1} - 4\phi^n + \phi^{n-1}}{2\Delta t} = F(\phi), \tag{3.10}$$

where ϕ is a scalar quantity, n indicates values at current time levels and $n+1$ and $n-1$ indicates values at next and previous time levels, respectively. $F(\phi)$ may be evaluated explicitly or implicitly. However, the pressure based solver only allows for implicit time integration, which is given as

$$\frac{3\phi^{n+1} - 4\phi^n + \phi^{n-1}}{2\Delta t} = F(\phi^{n+1}), \tag{3.11}$$

as opposed to the explicit method, where $F(\phi^{n+1})$ would have been replaced by $F(\phi^n)$. The implicit equation is solved iteratively at each time level until the convergence criteria are met (or the limit of iterations is met). The implicit scheme is unconditionally stable with respect to time step size for linear problems.

By introducing bounding of certain variables, the scheme provides better stability while keeping the level of accuracy [13]. Bounding involves setting upper and lower bounds for certain variables, to ensure that they never exceed their limits, e.g. the volume fraction has a lower bound of 0 and an upper bound of 1.

3.7 User-defined functions

In order to assign a sine-shaped velocity profile to the moving grid, user-defined functions (UDFs) are applied. A UDF is a function that can be dynamically loaded with the Fluent solver to enhance the standard features of the code. Fluent offers many predefined macros that may be adapted to fit the user's needs, and these are used to generate UDFs.

To define the grid motion, the macro DEFINE_ZONE_MOTION was used. A separate UDF was written for each of the motions investigated. The macro defines the different rotational and translational velocity components for a given grid zone. See Appendix B for a description of the macro and an example of the UDF. This macro was used for both the moving reference approach and the sliding grid approach, as described in Section 4.6.

Chapter 4

Grid generation

4.1 Introduction

When the geometry of a problem is defined, the grid (or mesh) is a discretization of the geometry, which spans the computational domain. Without a good quality grid, the solver will provide inaccurate solutions no matter how good the solver is. Grid generation for airfoils has been documented numerous times, and this study uses results from other articles as a starting point. Grid quality is dependent on many factors, such as the shape of the airfoil, the flow phenomena to be modeled and Reynolds number, among others. Thus a grid should not be created carelessly, but carefully to address the case at hand. This chapter covers basics of grid generation and descriptions of the grids used in this study.

The grid generation software Gambit version 2.4.6 was used to create all the grids in this study.

4.2 Structured and unstructured grids

A grid can be either structured, unstructured or hybrid (a combination of structured and unstructured regions). Examples of these grids may be seen in Figure 4.1. In a structured grid the cells can be represented in either a 2D (or a 3D) array, since all the cells have clearly defined neighbors. A structured grid in 2D is built up of quadrilateral (quad) cells and in 3D it is built up of hexahedra cells. A structured grid requires in general far less memory to store than an unstructured grid. The solver (e.g. Fluent) also requires in general less memory and computation time when working with structured grids than with unstructured grids; as the connectivity of the grid points given by the indices of structured grids can be more efficiently used than the connectivity lists of unctructured grids. A typical 2D unstructured grid consists of triangular (tri) cells, but quad cells can also be used. When an unstructured grid is stored, the connectivity between the cells needs to be explicitly stated, which requires more memory.

Even though structured grids have many benefits over unstructured ones, unstructured grids are still widely used. In practical engineering problems, the geometry defining the computational domain rarely fits with a structured grid (this is especially true for 3D problems). The advantage of an unstructured grid

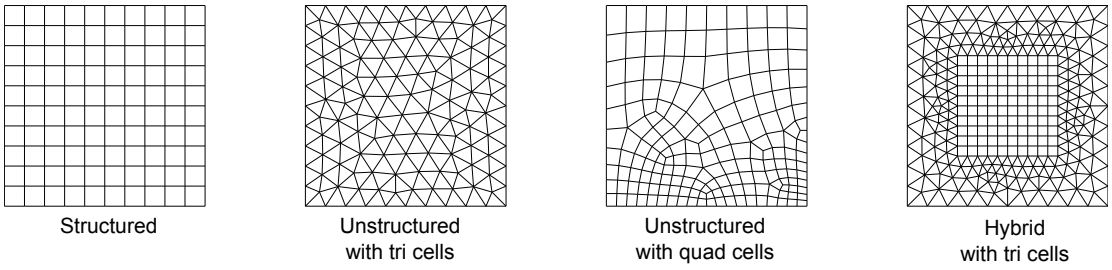

Figure 4.1: Four different grid types, generated by Gambit. The structured grid shown is a cartesian grid.

is the ease of fitting the cells to the geometry. The tri cells in a 2D grid can follow a complex shape without the need to consider the geometry in other areas of the domain. The unstructured grid also gives much better control in sizing the cells, while the structured grid often produces an abundance of cells in some areas. Thus, unstructured grids are well suited for local grid adaptation, whereas structured grids are not.

4.3 Grid quality

The quality of the grid is crucial for the accuracy of the final results. A low quality grid might not give convergence at all, or the converged solution could be far away from the actual solution of the problem. There are no absolute criteria to determine the quality of a grid. In general, a grid that gives results that coincide with experimental data is a good grid. In many cases experimental data is not available, and other metric properties are needed to evaluate the quality of the grid. Discussions of grid resolution and two important metric properties are given in this section.

In general a finer grid (high resolution) gives better results than a coarser grid. However, a coarse grid is faster to generate, requires less computational time and in general it converges more easily. Thus a coarse grid will often be used to quickly get initial results, and then a finer grid would be generated, based on results and knowledge gained from the coarse grid simulations.

A grid is coarse when the cells are too large to capture the effects of the smallest scales of interest. Vortex shedding, for example, involves vortices which requires cells of a certain scale to be described properly. If the cells are too large, the vortices might not be captured by the solver at all, or they might diffuse unnaturally because of numerical diffusion.

The aspect ratio is defined for a single cell and is given as the ratio of the longest and shortes sides of a cell; see Figure 4.2 for examples of cells with different aspect ratios. An ideal grid has only cells with an aspect ratio of 1. In most cases this is neither practical nor necessary.

Since a given quantity might have a different rate of change in one direction of the flow as compared to another, the cells can have different sizes (resolution) in these different directions. A flat plate boundary layer, for example, has large gradients in the direction normal to the plate, while there is little change in any

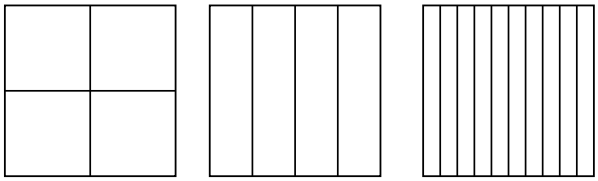

Figure 4.2: Examples of cells with different aspect ratios. Aspect ratios from left to right: 1, 4, 10.

direction parallel to the plate. The grid thus needs to be finer in one direction, compared to the others. As a rule of thumb, the aspect ratio should not exceed 10 in areas of interest, but in regions where the flow has a dominant direction (e.g. close to walls), a much higher aspect ratio is acceptable.

There are many ways to measure the skewness of a cell, one is the EquiAngle Skew Q_{EAS}, which ranges from 0 for equilateral cells to 1 for degenerate cells. A detailed description may be found in the Gambit User's Guide [42]. Examples of cells with different Q_{EAS} may be seen in Figure 4.3. Values below 0.25 are considered of excellent quality, while values above 0.75 are considered poor quality [42].

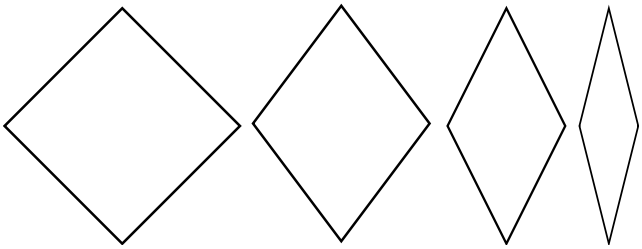

Figure 4.3: Examples of cells with different cell skewness. From left to right: $Q_{\text{EAS}} = 0$, $Q_{\text{EAS}} = 0.25$, $Q_{\text{EAS}} = 0.50$, $Q_{\text{EAS}} = 0.75$

4.4 The O-grid

The O-grid gets its name from the circular shape of the structured grid that encompasses the airfoil, as may be seen in Figure 4.4. Another grid type used for airfoils is the C-grid, which gets its name from the C-shape that encompasses the airfoil, as may be seen in Figure 4.5. Since the C-grid is the preferred grid type in many studies (c.f [27, 4, 26]), some comparisons are made between the O-grid and the C-grid.

There are two main reasons for using the O-grid in this study. First, previous work done by the author [34] showed that the O-grid gave more accurate results than the C-grid for a single airfoil at Reynolds number of $2 \cdot 10^6$. Secondly, the C-grid is not compatible with the sliding mesh technique used to model relative motion between two airfoils (see Section 4.6.2), since the technique requires vertical boundaries separating the two airfoils (two C-grids do not easily connect to one another in the horizontal direction).

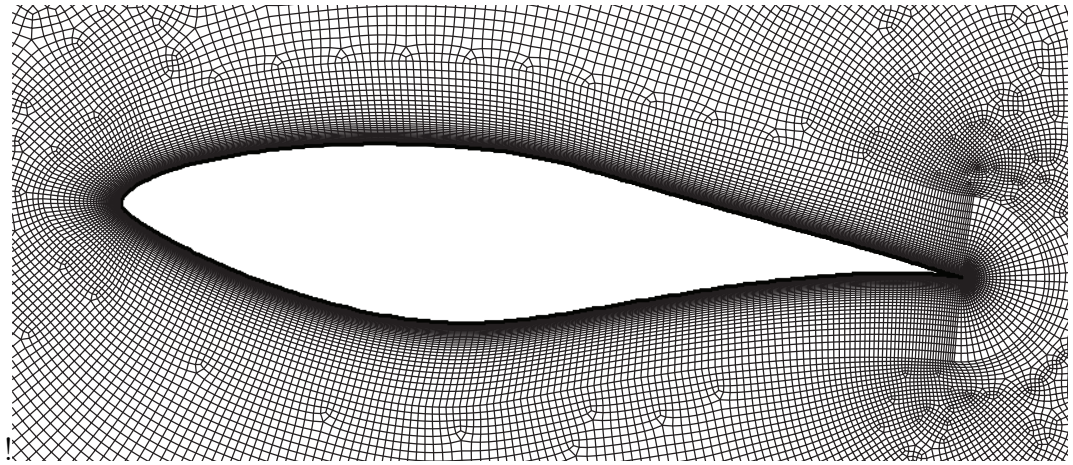

Figure 4.4: A close up view of the airfoil in the O-grid.

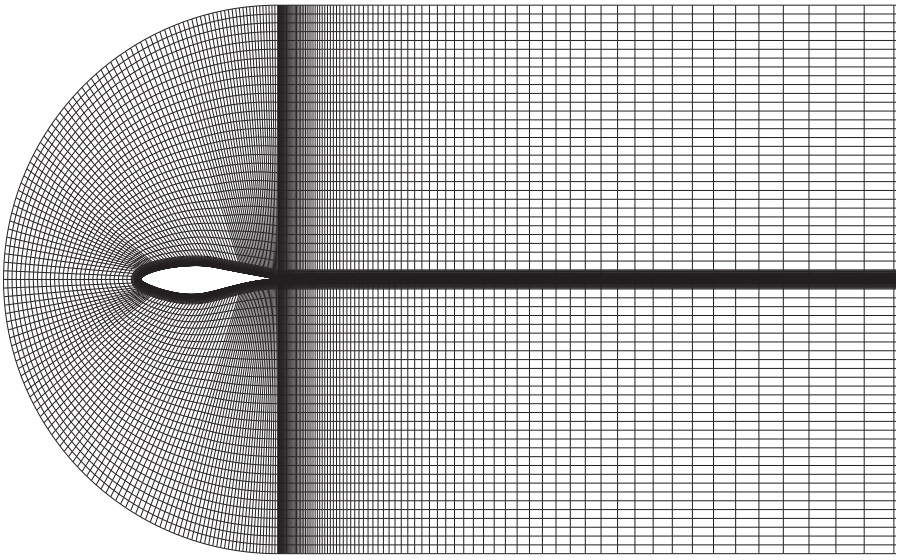

Figure 4.5: An example C-grid.

The O-grid used here consists of a structured part within the "O" to resolve the boundary layer. The outer region can be structured, unstructured or hybrid. In order to achieve more control of the grid in the regions far away from the airfoil, the unstructured or hybrid versions of the O-grid can be used. In these versions, there is a region of unstructured cells outside of the "O" (as seen in Figure 4.4), which is able to connect to any shape desired further away from the airfoil. As a result these versions of the O-grid will in general consist of fewer cells than the C-grid.

The unstructured cells could have high skewness, which is a disadvantage of the O-grid. Another disadvantage of the O-grid is that it requires more time and effort to generate, as it consists of more regions, often of different cell types, and thus more input parameters are required. Also, it is more computationally demanding for a grid generator to produce an unstructured grid than a structured grid; the C-grid, on the other hand, is usually structured.

The O-grid gives the ability to form a rectangular boundary of the domain (see Figure 4.6), which makes the assignment of far field boundary conditions easier than for the C-grid. The vertical boundary upstream will always be an inlet, the vertical boundary downstream will always be an outlet and the horizontal boundaries above and below the airfoil will be either inlets or outlets, depending on the direction of the flow.

4.5 Grid characteristics

This section presents the grids used to model both one and two airfoils. First an overview is given, and then details are discussed in the two following subsections, while the third and last subsection discusses the grid for two airfoils in relative motion.

An overview of the grid may be seen in Figure 4.6. The airfoil may be seen in the middle, with the grid boundary layer surrounding it. There is an unstructured region outside the grid boundary layer, and eight structured regions build up the wake and far-field regions.

The total number of cells for the O-grid used in the study of a single oscillating airfoil was 294,185. This is a fairly high number of cells, as compared to typical numbers found in the literature for comparable grids. The reason for this is the need for a lot of cells in the area downstream of the airfoil to properly resolve the wake structures that occurs for oscillating airfoils.

4.5.1 Grid boundary layer

The number of cells within the airfoil grid boundary layer (BL) is determined by previous work done by the author [34], and a summary is given here. It should be noted that the grid BL is the region of structured cells closest to the airfoil (the "O"), and is different from the physical BL. The grid BL is notably larger than the physical one, in order to provide a good quality grid in the region of the physical BL. The grid BL characteristics used for all grids in this study are summarized in Table 4.1

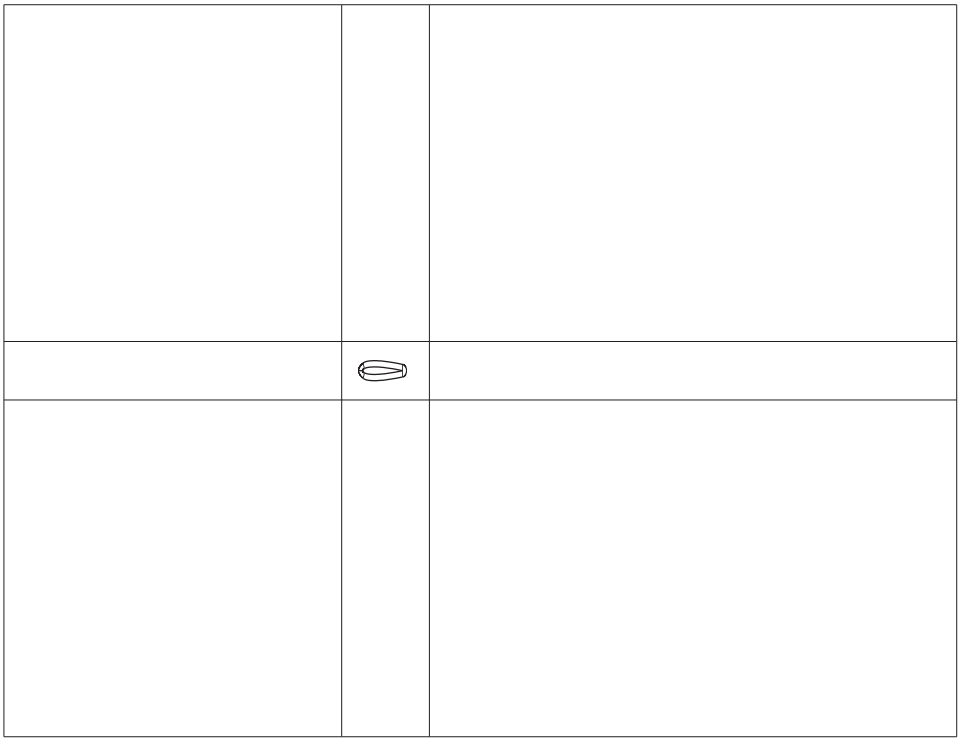

Figure 4.6: An overview of the O-grid used for a single airfoil.

Table 4.1: Overview of the grid boundary layer around the airfoil for the O-grid used in this study. Heights are given with respect to the chord length C of 1 m.

Grid boundary layer	
Total cells	$26,950$
Nodes on airfoil	340
BL height	$0.10C$
Rows in BL	55
Growth factor	1.14
Height of first cell	$3{\cdot}10^{-5}C$
Max aspect ratio	567
Max cell skewness	0.92

On the airfoil surface, 340 nodes were found to be sufficient. The nodes were not evenly distributed, but more nodes were placed near the nose of the airfoil and near the trailing edge, since the gradients are normally higher in these areas than along the middle of the airfoil, especially for oscillating airfoils. This distribution leads to a maximum aspect ratio of 567, which is also the highest aspect ratio of the entire grid. This is believed to be acceptable, since the dominant flow direction is along the length of the cells (i.e. low gradients along the length of the cells). Leading edge vortex shedding (see Section 6.3.1) will produce higher gradients along the length of the cells, but the number of nodes on the airfoil was still kept at this number, partly based on results in the literature (cf. [26]). Results showed no clear indication that more nodes were needed, indicating that 340 nodes were sufficient.

The maximum cell skewness of 0.92 would be unacceptable high if this number was representative for the grid. However, this level of skewness is found in the 150 "pizza slice" shaped cells next to the trailing edge, which are a result of all the grid lines from the outer edge of the BL terminating in a single point at the trailing edge. It was not believed that these few low quality cells would have any significant impact on the flow. Except for these few cells, the maximum cell skewness in the grid BL was 0.18.

The grid BL height was set to be high enough to ensure that the physical BL for attached flow would always be well within its boundaries and low enough for practical reasons concerning connecting the grid BL to the rest of the domain as well as being able to model two airfoils close to each other. The growth factor and number of rows were determined by the need for at least ten cells to cover the physical BL as well as to give the cells in the outer layer an aspect ratio close to one.

The height of the first cell was determined by a grid independence study for turbulent flow and it is believed to be sufficiently small for laminar flow, which should in general have less strict requirements as the gradients are lower for a laminar BL. A few random cases from this study were investigated, and they were all found to have more than 20 cells covering the physical BL.

Wall treatment in the turbulence models places additional constraints on the near wall grid. The Fluent User's Guide recommends y^+ values (see Section 2.4) to be less than 1 for the first layer of cells next to a wall when the Transition SST turbulence model is used. This is in order to resolve transition regions. The y^+ values are dependent both on the grid as well as the flow. Thus, to achieve a grid with desired y^+ values, it might need to be adapted after simulations are run. Since time constraints do not allow for such grid refinements to be performed for every case setup the same near-wall resolution was used in all simulations. The values of y^+ for the first layer of cells ranged from averages of the entire airfoil of around 1.7 for most cases to around 3 for some cases.

4.5.2 Outer grid

The outer grid, meaning the grid except for the grid boundary layer, was determined by a grid independence study (see Section 5.1.1). Some grid characteristics are given in Table 4.2

Table 4.2: Overview of the grid outside of the grid boundary layer for the O-grid used in this study.

Outer grid	
Cells	267,235
Max aspect ratio	137
Max cell skewness	0.87

There were 61,335 cells in the unstructured region encompassing the airfoil grid boundary layer and 120,000 cells in the structured wake region downstream of the airfoil. The cells in the area a few chord lengths behind the airfoil were typically around $0.01C$ times $0.01C$ in size. These values were in consistence with cell sizes found by both Young [26] and Guerrero [2], who found that cells of $0.0176C$ and $0.0167C$, respectively, where sufficient to describe the physics of similar laminar flows. It should be noted that neither [26] nor [2] used Ansys Fluent to perform their simulations.

To achieve a high resolution of cells in the near wake region of the airfoil, the cells in the structured region were not evenly distributed, but concentrated close to the airfoil. This gave the cells next to the downstream outer edge of the domain a length of $0.17C$. This was considered acceptable, as these cells where around $19C$ away from the airfoil, and thus also far away from the regions of interest.

The maximum aspect ratio in the outer grid of 137 is found in a few cells next to the outer boundaries of the grid. The aspect ratios of the cells quickly drop further away from the outer boundaries. In the unstructured region, as well as the area a few chord lengths behind the airfoil, all the cells have aspect ratios of less than 2. This is a clear advantage of the O-grid as compared to the C-grid, as a C-grid would typically have aspect ratios a few orders of magnitudes higher in the area behind the airfoil.

The maximum cell skewness of 0.87 was found in the unstructured grid outside of the grid BL. Some cells with high cell skewness easily occur in unstructured grids when there is significant change in the grid geometry or sizing of the cells. There were 24 (0.04% of the unstructured cells) cells with values of cell skewness above 0.50 and 5166 (8.42% of the unstructured cells) cells with values of cell skewness above 0.25 for the grid of a single airfoil. Similar values were found for the grids for the tandem setup.

Even though the majority of cells had low cell skewness values (< 0.25), the cells with high levels of cell skewness are considered to be a disadvantage of the O-grid, as compared to the C-grid, which will typically have almost all the cells with cell skewness values below 0.25.

4.5.3 Grids for tandem setup

When creating the grids for the tandem airfoil setup, the same grid characteristics as for the grid of a single airfoil were used. An overview of a sample grid may be seen in Figure 4.7 and a close up of a sample grid with the NACA 0012 profile may be seen in Figure 4.8. Figure 4.8 also defines the distance X_{shift}, which is the distance between the trailing edge of the leading airfoil and the leading edge of the

trailing airfoil, X_{shift} is used throughout the report to refer to this distance. The grids were not extended lengthwise when two airfoils were included. This resulted in the trailing airfoil having a shorter distance to the end of the grid than was the case for the single airfoil grid. The single airfoil grid provided 19 chord lengths of grid behind the airfoil, while the two airfoil grid with the airfoils separated two chord lengths apart provided 16 chord lengths of grid behind the trailing airfoil. This was not believed to affect the solution significantly.

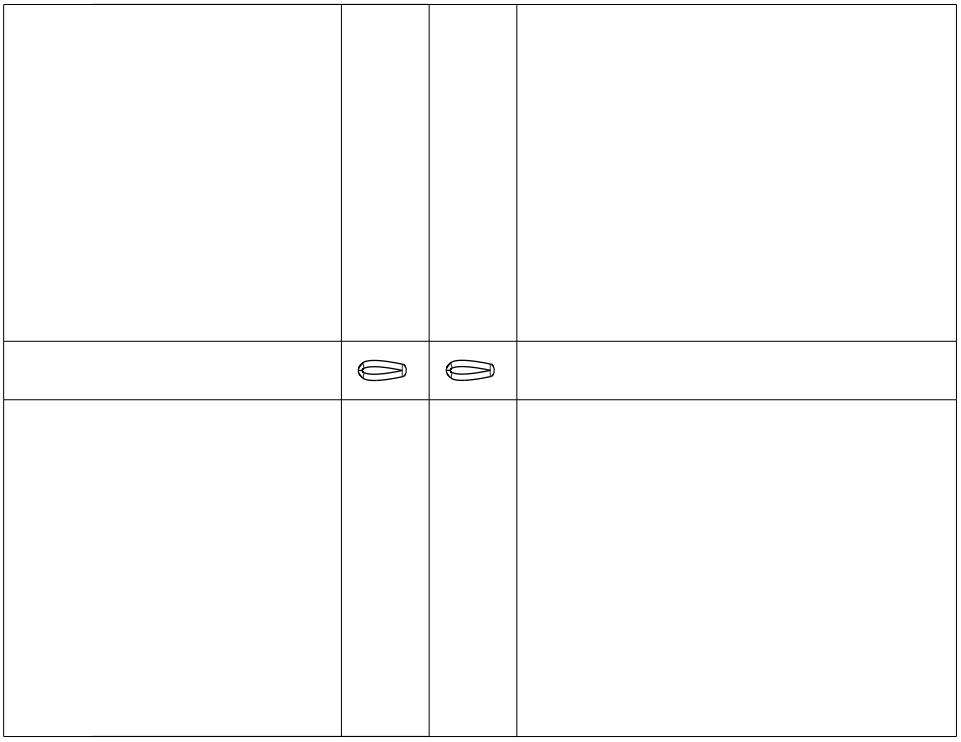

Figure 4.7: Overview of a sample grid used for the tandem setup.

Table 4.3 gives an overview of some of the characteristics for the different grids. As can be seen, there is not much differentiating the four different grids. The number of cells increases slightly for X_{shift} values of 2. This is due to the requirement of a fine grid in the area between the airfoils, which gets extended as the airfoils are placed further apart. The maximum aspect ratios and cell skewness are all found within the grid boundary layer, and are therefore very similar for all grids. Section 5.1.1 presents a grid independence study which determined the grid resolution in the wake region.

4.6 Moving reference frames and sliding grids

To model the airfoil as oscillating a moving reference frame was used for the cases with a single airfoil and the sliding grid technique was used in the tandem airfoil setup. This section provide descriptions of the two different methods.

For both of the methods, the motion was described by user-defined functions (UDF), which are described in Section 3.7.

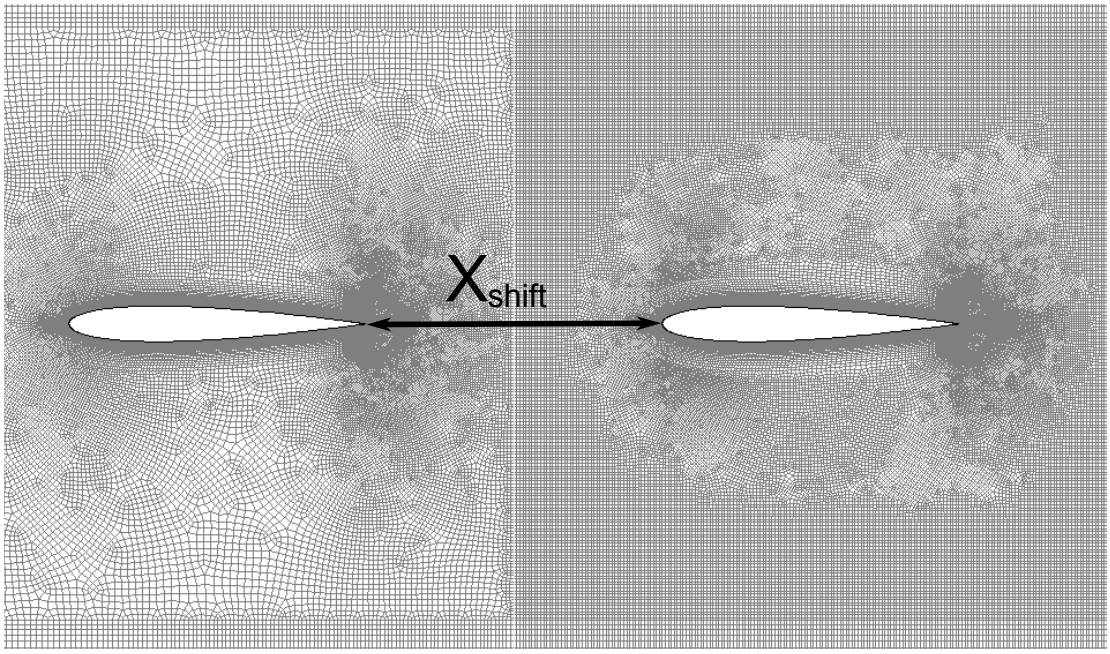

Figure 4.8: A close up view of a sample grid for the tandem setup for two NACA 0012 profiles. The distance X_{shift} between the two airfoils is marked.

Table 4.3: Grid characteristics for grid of two airfoils. X_{shift} is the distance between the airfoils, given in chord lengths C.

	NACA 0012		S809	
X_{shift}	$1C$	$2C$	$1C$	$2C$
Cells	$338,696$	$351,225$	$342,970$	$354,620$
Nodes on airfoil	340	340	340	340
Maximum aspect ratio	567	567	582	582
Maximum cell skewness	0.98	0.98	0.98	0.98

4.6.1 Moving reference frames

To model a single oscillating airfoil, the entire grid was set as a moving reference frame. The velocity specification was set to absolute, which specifies the velocities relative to the inertial reference frame, as opposed to the moving reference frame.

The relationship between the velocities in the moving and inertial reference frames is given as

$$\mathbf{v} = \mathbf{v}_r + \mathbf{u}_r, \tag{4.1}$$

where $\mathbf{v}$ is the velocity in the inertial frame, $\mathbf{v}_r$ is the velocity in the moving frame and $\mathbf{u}_r$ is the velocity of the moving frame. With this formulation, the governing equations of fluid flow can be written as follows when there is no angular velocity in the moving reference frame, conservation of mass:

$$\frac{\partial \rho}{\partial t} + \boldsymbol{\nabla} \cdot \rho \mathbf{v_r} = 0 \tag{4.2}$$

and conservation of momentum:

$$\frac{\partial}{\partial t} \rho \mathbf{v} + \boldsymbol{\nabla} \cdot \rho \mathbf{v_r} \mathbf{v} = -\boldsymbol{\nabla} p + \boldsymbol{\nabla} \cdot \tau + \mathbf{f}, \tag{4.3}$$

where ρ is the density, p is the pressure, τ is the viscous stress tensor and $\mathbf{f}$ are external forces.

4.6.2 Sliding grids

To model the tandem setup with the leading airfoil oscillating and the trailing airfoil stationary with respect to the inertial reference frame, the sliding grid technique was used. As with the moving reference frame, the velocity specification was set to absolute.

In the sliding grid technique two or more cell zones must be specified, each with at least one interface boundary. The zones move relative to each other along the interface boundaries, and the grid is updated by Fluent during each time-step. A sliding grid is illustrated in Figure 4.9. The new boundary zones that occur can be assigned any boundary condition, just as any other boundary zone. When the two cell zones move relative to each other, the grid becomes non-conformal, cf. Section 4.6.3.

There are certain changes to the equations in the solver as a result of the sliding grid. The integral form of the conservation equation for a general scalar, ϕ, on an arbitrary control volume, V, is given in Fluent as

$$\frac{d}{dt} \int_V \rho \phi \, \mathrm{d}V \int_{\partial V} \rho \phi \left(\mathbf{v} - \mathbf{v}_r \right) \cdot \mathrm{d}\mathbf{A} = \int_{\partial V} \Gamma \boldsymbol{\nabla} \phi \cdot \mathrm{d}\mathbf{A} + \int_V S_\phi \, \mathrm{d}V, \tag{4.4}$$

where ρ is the density, ϕ is a general scalar, $\mathbf{v}$ is the flow velocity vector, $\mathbf{v}_r$ is the grid velocity of the moving grid, Γ is the diffusion coefficient, S_ϕ is the source term of ϕ and ∂V represents the boundary of the control volume V.

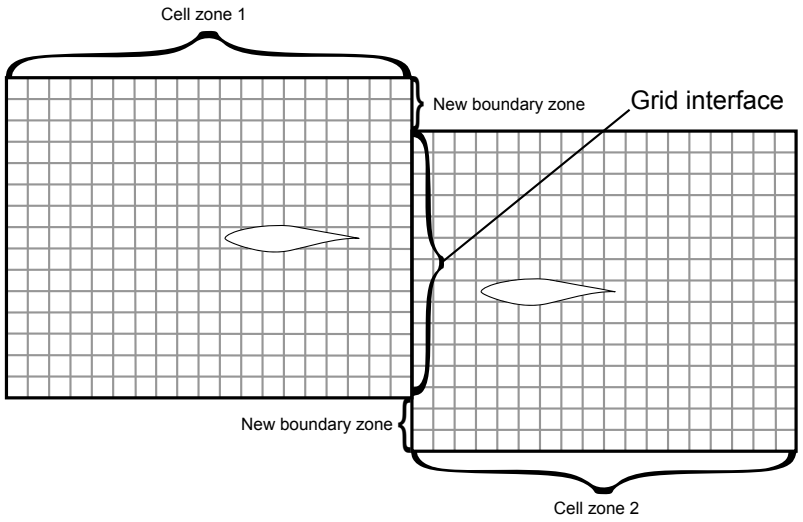

Figure 4.9: An illustration of a sliding grid. Not to scale.

4.6.3 Non-conformal grids

When two cell zones move relative to each other, the cells on each cell zone boundary will not necessarily align. This is always true if the cells are not uniformly spaced, and also true when the relative distance the grids shifts during each time-step is not equal to exactly one cell height. An example of a non-conformal grid may be seen in Figure 4.9, where the cells do not align along the grid interface.

Figure 4.10 shows a more detailed example of a non-conformal grid interface. Fluent calculates fluxes across the grid interface using cell faces that result from the intersection of the two zones, and not from the original zone boundaries. Thus the fluxes through face D-E into cell IV in figure 4.10 is calculated by using faces d-b and b-e, and not face D-E. This allows for an arbitrary number of cells from one cell zone to align to an arbitrary number of cells in an adjacent cell zone.

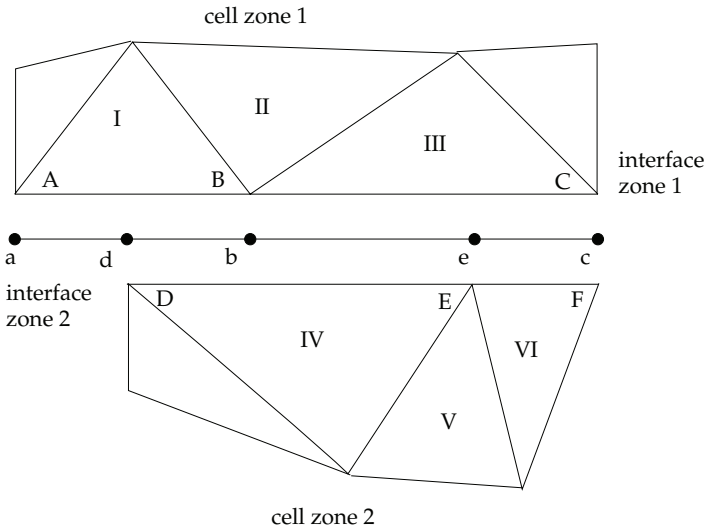

Figure 4.10: A detailed example of a non-conformal grid interface. From Fluent User's Guide [13]

Chapter 5

Model verification and validation

It is important to know if the results generated from the solver are accurate and the level of error in the results. Both model verification and validation are performed in order to assess this. Verification is defined as:

> The process of determining that a model implementation accurately represents the developer's conceptual description of the model and the solution to the model. (AIAA G-077-1998)

and validation is defined as:

> The process of determining the degree to which a model is an accurate representation of the real world from the perspective of the intended uses of the model. (AIAA G-077-1998)

Where both definitions are given by the American Institute of Aeronautics and Astronautics (AIAA).

The verification process controls that the model and the code solve the equations and problem setup as intended by the software and the user. A common verification method is to solve a problem where the analytical solution is known, and then compare the results to the analytical solution. As it is not believed that there are any major coding errors in Fluent, this part of the verification is skipped, and focus is on the model setup of the case to be investigated in this study.

The validation process compares the CFD results to experimental data, in order to investigate how well the simulations describe the real world system. There are limited experimental data available for cases investigated in this study. Flow visualizations and data for propulsive efficiency for different Strouhal numbers are available for the laminar setup, but no experimental data is available for the turbulent setup.

This chapter is divided into two parts, the first for validation and verification of the laminar setup and the second for verification of the turbulent setup. Focus is on grid independence and time-step independence.

5.1 Laminar flow

5.1.1 Grid independence study

A grid independence study was performed to determine the grid in the wake region. Two parameters were varied in order to find the optimal grid, based on both the quality of the results as well as computational time. First the number of cells along the edge α, as given in Figure 5.1, was varied. And afterwards the number of cells along the edge β. To compare the results of the grids, vorticity contour plots were investigated. It should be noted that plots of particle tracks were also used in order to compare the different grids, but as the plots of vorticity contours provided better means to compare and differentiate them, plots of particle tracks are not included in this section.

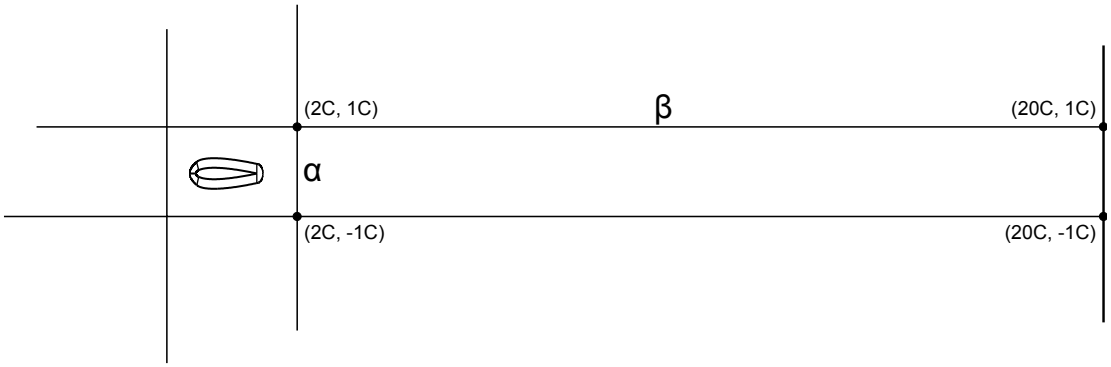

Figure 5.1: Definitions of the edges α and β used in the grid independent study. C is the airfoil chord length.

When the number of cells on α was varied, the number of cells on the edges forming the box encompassing the airfoil, as seen in Figure 5.1, was also varied. This was done in order to make the cells in the corners of the box close to quadratic. The resolution on α would also dictate the resolution of the unstructured grid, as the cells would grow in size as the distance from the airfoil increased. Thus the region of interest is from the trailing edge to one chord length downstream of the airfoil, as this is where α affects the grid quality the most.

Table 5.1: The different grids used in the first part of the grid independence study. The edge α is defined in Figure 5.1. The deviation of th velocity modulus on $y = 0$ is compared at a time instant.

	Nodes on edge α	Height of cells on edge α	Average deviation from Grid C	Max deviation from Grid C
Grid A	100	$0.020C$	3.8%	16.1%
Grid B	200	$0.010C$	1.9%	7.8%
Grid C	300	$0.007C$	0%	0%

The three different grids investigated in the first part of the grid independence study are summarized is Table 5.1.

Vorticity contour plots generated from the grids with different resolutions in the unstructured region may be seen in Figure 5.2. In grid A there is a clear diffusion of vorticity, which is not seen in the same extent in grids B and C. By a visual inspection of Figure 5.2, there seem to be small differences between grid B and grid C.

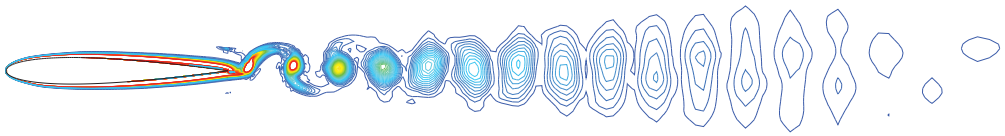

(a) Grid A. 100 nodes on α, cell heights of $0.020C$.

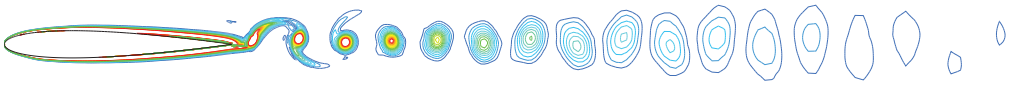

(b) Grid B. 200 nodes on α, cell heights of $0.010C$.

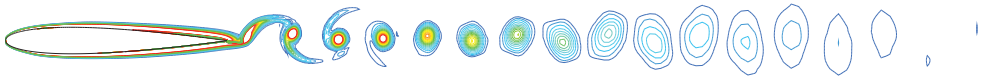

(c) Grid C. 300 nodes on α, cell heights of $0.007C$.

Figure 5.2: Comparison of vorticity contour plots after 10 periods for grids with different resolution in the unstructured region, which ends one chord length downstream of the airfoil. The edge α is defined in Figure 5.1. $Re = 20,000$, $k = 7.8$ and $h = 0.0125$ ($Sr = 0.15$).

Figures 5.3 and 5.4 compare velocity magnitudes, plotted along the symmetry axis of the airfoil, for the different grids after ten periods. There are clear differences in the plots. Grid A has a maximum deviation from grid C of 16.1% and an average deviation of 3.8%. Grid B has a maximum deviation from grid C of 7.8% and an average deviation of 1.9%.

Grid B, with 200 nodes on α was chosen for further work. Grid independence was not achieved, and a grid even finer than grid C might produce somewhat different results. However, due to time constraints, 200 nodes on α were chosen, since the number of cells in the entire grid (and thus computational time) was greatly reduced as compared to 300 nodes and the average deviation between the two grids was less than 2% (Table 5.1).

With the grid in the unstructured region determined, five grids with different resolution in the structured region downstream were compared. Different resolutions were achieved by altering the amount of nodes on edge β. A uniform distribution would remove the need for further investigation, but in order to reduce the number of cells (and thus save computational time), the cells where concentrated closer to the airfoil. Table 5.2 summarizes the deviation of $|\mathbf{v}(x, y = 0, t)|$ after ten periods for the five different grids

Vorticity contour plots generated from the grids with different resolutions in the structured region may be seen in Figure 5.5. In grid B there is a clear diffusion

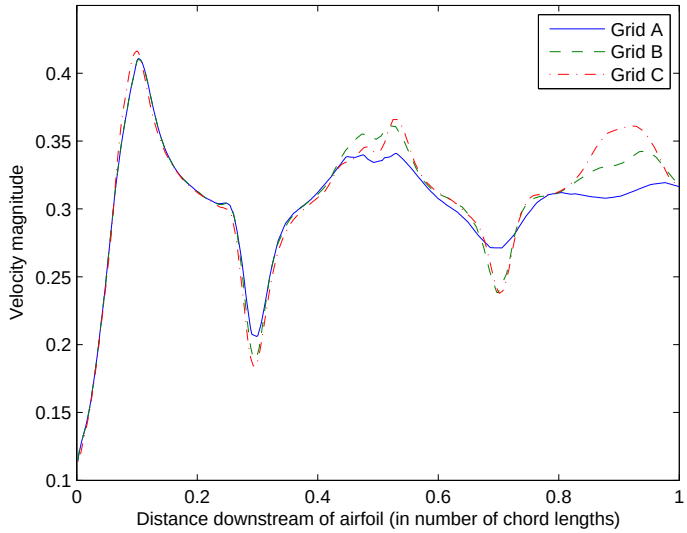

Figure 5.3: Velocity magnitude plotted along the symmetry axis of the airfoil.

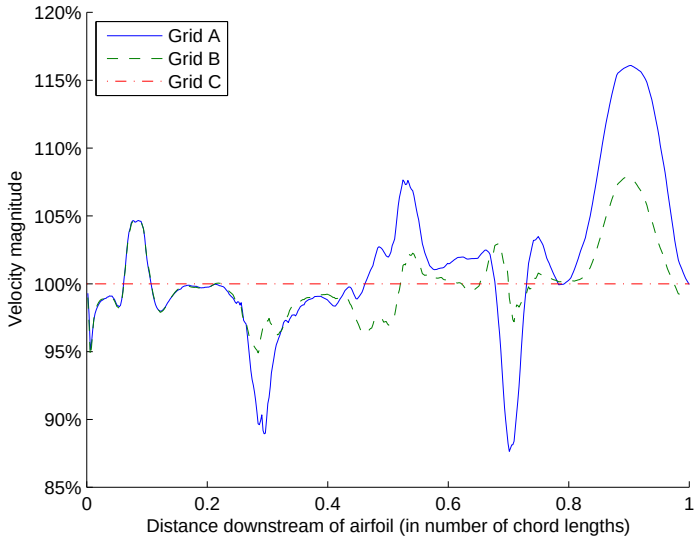

Figure 5.4: Velocity magnitude in percent plotted along the symmetry axis of the airfoil with grid C set as a reference.

Table 5.2: The different grids used in the second part of the grid independence study. Grid B is identical to Grid B in Table 5.1. The edge β is defined in Figure 5.1. The deviations of the velocity on $y = 0$ are compared after ten periods.

	Nodes on edge β	Average deviation from Grid G	Max deviation from Grid G
Grid B	200	5.2%	10.9%
Grid D	400	3.1%	7.1%
Grid E	600	1.2%	5.0%
Grid F	800	0.7%	2.9%
Grid G	1000	0%	0%

of vorticity, and there is less diffusion as the number of cells is increased in Grid D through G. By visual inspection of Figure 5.5 Grid E, F and G provide similar results up to about three chordlengths downstream of the airfoil.

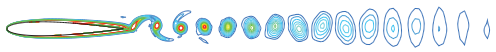

(a) Grid B. 200 nodes on edge β.

(b) Grid D. 400 nodes on edge β.

(c) Grid E. 600 nodes on edge β

(d) Grid F. 800 nodes on edge β.

(e) Grid G. 1000 nodes on edge β.

Figure 5.5: Comparison of vorticity contour plots after 20 periods for grids with different resolution in the region downstream of one chord length. The edge β is defined in Figure 5.1. $Re = 20,000$, $k = 7.8$ and $h = 0.0125$ ($Sr = 0.15$).

Figure 5.6 and 5.7 compare velocity magnitudes, plotted along the symmetry axis of the airfoil, for the five different grids. There are clear differences in the plots. Grids B and D deviate significantly from the three finest grids, as seen in Figure 5.6, while there are small differences between Grid E, F and G up to about four chord lengths downstream of the airfoil. Grid E has a maximum deviation from grid G of 5.0% and an average deviation of 1.2%. Grid F has a maximum deviation from grid C of 2.9% and an average deviation of 0.7%.

The results indicate that grid independence could be achieved had the grid been refined even further. However, in order to limit computational demand, the number of cells needed to be limited. Grid E was chosen to determine the grid characteristics of grids used in this study. It significantly reduced computational time, while providing comparable accuracy.

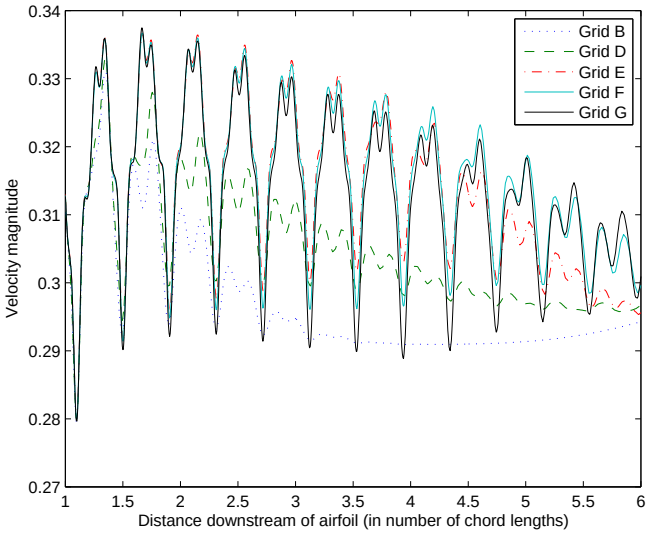

Figure 5.6: Velocity magnitude plotted along the symmetry axis of the airfoil.

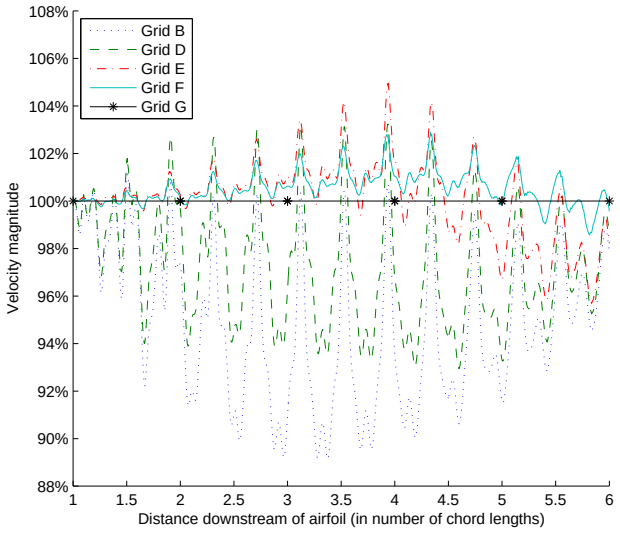

Figure 5.7: Velocity magnitude in percent plotted along the symmetry axis of the airfoil with grid G set as a reference.

5.1.2 Residual criteria

In transient implicit simulations there are three factors that determine the number of iterations performed during each time step. The first is the size of the time-step Δt, the second is the residual criterion and the third is the user-set limit of maximum number of iterations. For smaller time-steps, the residual criterion is met quicker, since there are smaller changes in the solutions, as compared to higher time-steps. In order to determine the residual criteria that would give solutions independent of the criteria, multiple simulations with different residual criteria were evaluated for a $Re = 20,000$ (laminar flow). The different residual criteria, for continuity, x-velocity and y-velocity, were all set to the same levels in this investigation. The residuals for continuity were the ones to reduce at the slowest rates for all laminar cases, while it was the turbulent dissipation rate ω for the turbulent cases.

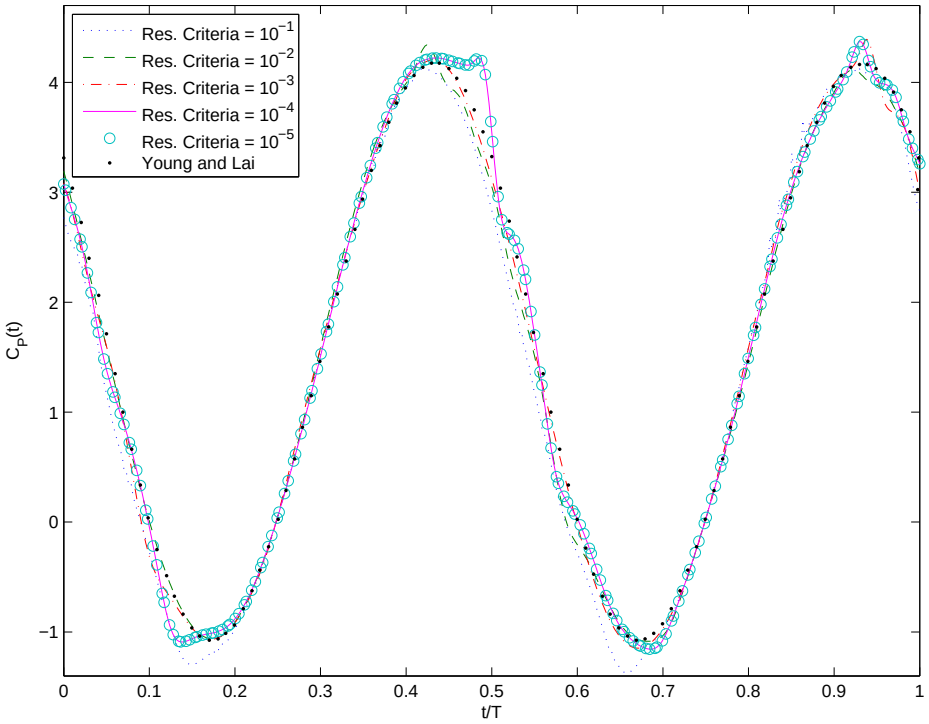

Figure 5.8: Comparison of power coefficient C_{Power} for different residual criteria and numerical results from Young and Lai [14].

As seen in Figure 5.8 the different residual criteria produce different results. The data presented are of the power coefficient C_{Power}, similar plots for the lift coefficient C_L and the thrust coefficient C_T were also generated, but are not included here as they produced similar results.

When the criteria were set to 10^{-4} or lower, a significant change in the results occurred. Most notably are the changes in the C_{Power} peaks when the residual criteria are set to 10^{-4} or lower. The peaks in C_{Power} might be explained by leading

edge vortex shedding, although time constraints prohibited a proper investigation. It was believed that the finer residual criteria provided the more accurate results.

As may be seen in Figure 5.8 the results from residual criteria of 10^{-4} and 10^{-5} are identical. This was also the case for the 10^{-6} criteria, but these data were excluded from the plot in order to make it more readable. They all provided the same results because the limit of 20 iterations per time-step were met throughout the simulations for all these cases. To save computational time the limit of 20 iterations per time-step was not increased.

Throughout the study residual criteria of 10^{-4} were used for all cases, laminar as well as turbulent. This would result in the limit of 20 iterations per time-step being met for virtually all simulations.

5.1.3 Validation

To validate the laminar setup, comparisons are first done to experimental data generated by Heathcote et al. [15] and then flow visualizations are compared to experiments performed by Lai and Platzer [11].

In Figure 5.9 data from this study is compared to experimental data generated by Heathcote et al. [15]. The experimental data was generated at $Re = 10,000$, $20,000$ and $30,000$. However, as there were little dependency on Reynolds number in the data, all experimental data points are plotted on the same graph in Figure 5.9. The un-evenness in the experimental data for low Strouhal numbers are due to different Reynolds numbers being the source for the different data points.

The trend in all graphs is the same and the finer time-steps matches the experimental data better than the coarser time-steps. There was an over-prediction in the numerical data for Sr larger than 0.10, and there was an under-prediction in the numerical data for Sr smaller than 0.10. The numerical simulations provide negative η for Sr of 0.05. A simulation for this value of Sr was not performed for the time-step of $0.001s$ due to a high demand for computational time for this case.

The peak in the experimental data occurs around $Sr = 0.10$, while it is at $Sr = 0.15$ for the numerical data. For the time-step of $0.01s$ the peak is at $Sr = 0.15$ and $\eta = 0.285$ while the highest η is at $Sr = 0.11$ and $\eta = 0.277$ for the experimental data.

Particle tracks (streak lines) were generated for some of the laminar simulations for a single oscillating airfoil. The particle tracks for the the case of amplitude $h = 0.0125$, reduced frequency $k = 7.8$ and $Re = 20,000$ may be seen in the upper frame of Figure 5.10. The particle tracks of this study resemble closely those generated numerically by Young [26] (middle frame) as well as those generated through experiments by Lai and Platzer [11] (lower frame). This indicates that the solver generates reliable results for the laminar cases.

The airfoil experiences an average drag (as opposed to thrust) in this setup, which should produce upstream tilting "'mushrooms"' (as explained in Section 2.9.3). The particle tracks by Young [26] clearly shows this phenomenon for both the upper and lower mushrooms. In both this study as well as the experiments of Lai and Platzer [11], the upper row of mushrooms are not tilted while the lower rows are tilted upstream. Towards the end of the particle tracks generated in this

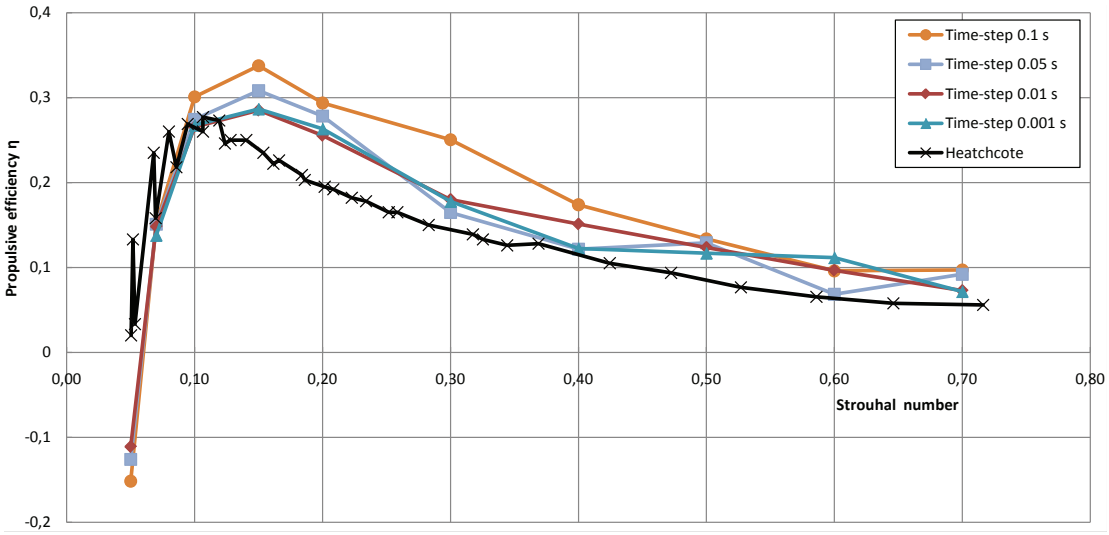

Figure 5.9: Plot of propulsive efficiency η vs Strouhal number for different time-steps. Experimental data from Heathcote et al. [15].

study the upper row is tilted downstream, indicating thrust production, this is most likely caused by the start up effects which are clearly visible to the far right in the upper frame of Figure 5.10.

5.1.4 Time-step size

Different time-step sizes were investigated in order to determine the time-step necessary for a solution independent of time-step size. In the time histories in Figure 5.11 time-steps of $0.1s$ and $5 \cdot 10^{-2}s$ show deviations from the other time histories near the peaks. Time-steps of $1 \cdot 10^{-2}s$ and $1 \cdot 10^{-3}s$ give similar results to each other except for some artifacts in the $1 \cdot 10^{-2}s$ time-step.

Figure 5.12 shows a clear improvement in the vorticity contour plots when the time-step is decreased, however, the trend ends for the finest time-step of $1 \cdot 10^{-3}s$. For this time-step, the numerical diffusion seems to increase rather abruptly. Also, some artifacts in the plot can be observed around the airfoil. This same trend is visible in the particle tracks in Figure 5.13; the quality increases until the finest time-step is reached. For this time-step, the particle tracks do not look natural, indicating that something is wrong with the model.

The reasons for the apparent model breakdown of the finest time-step of $1 \cdot 10^{-3}s$ were not found, and a thorough investigation was not conducted as the time-step of $1 \cdot 10^{-2}s$ was considered sufficient. Any time-step significantly finer than $1 \cdot 10^{-2}s$ would also result in a substantial increase in computational time.

5.2 Turbulent flow

For the turbulent flow ($Re = 3,000,000$), the grids used were the same as those used for the laminar flow ($Re = 20,000$). The grid close to the airfoil had been verified and validated to be of acceptable accuracy during previous work [34] at $Re = 2,000,000$. The far-field grid which made up the wake region could have

(a) Particle tracks (streak lines) from numerical simulations in this study

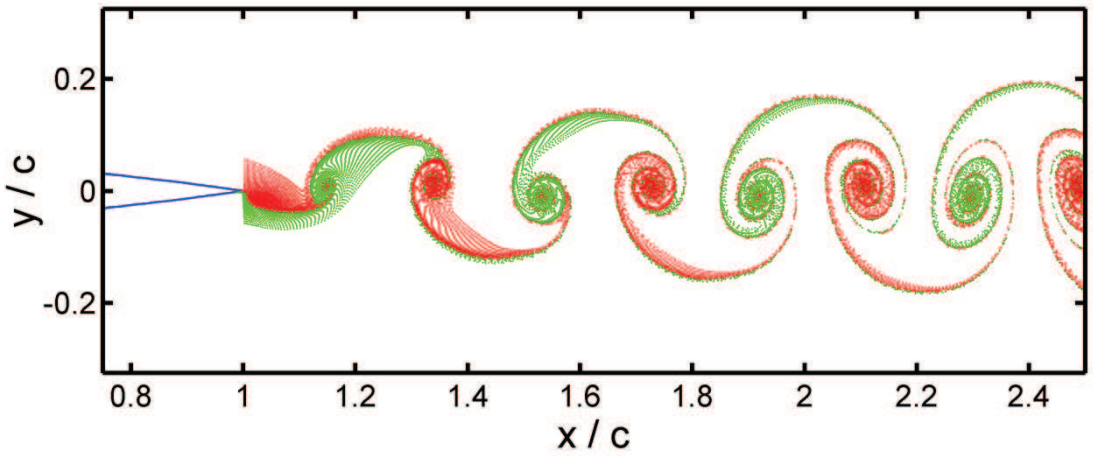

(b) Particle tracks (streak lines) from numerical simulations performed by Young (2005) [26].

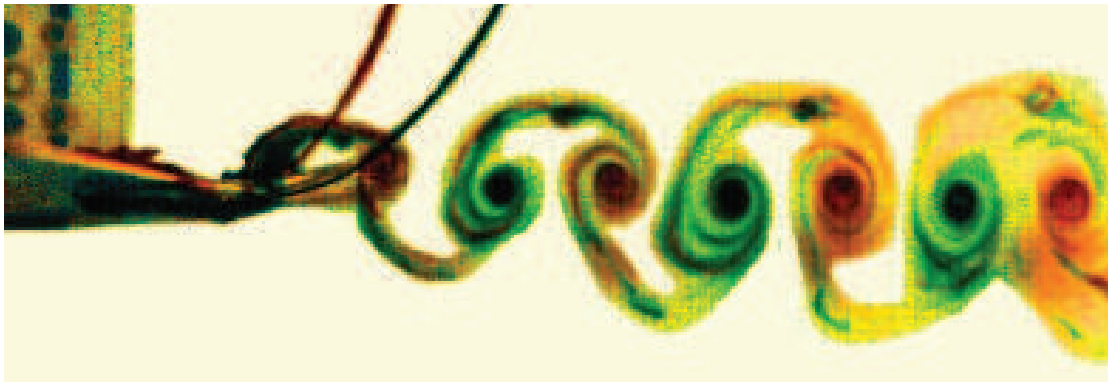

(c) Dye flow visualization from experiments performed by Lai and Platzer (1999) [11].

Figure 5.10: Vortex patters for single oscillating airfoil at $h = 0.0125$, $k = 7.8$ and $Re = 20,000$.

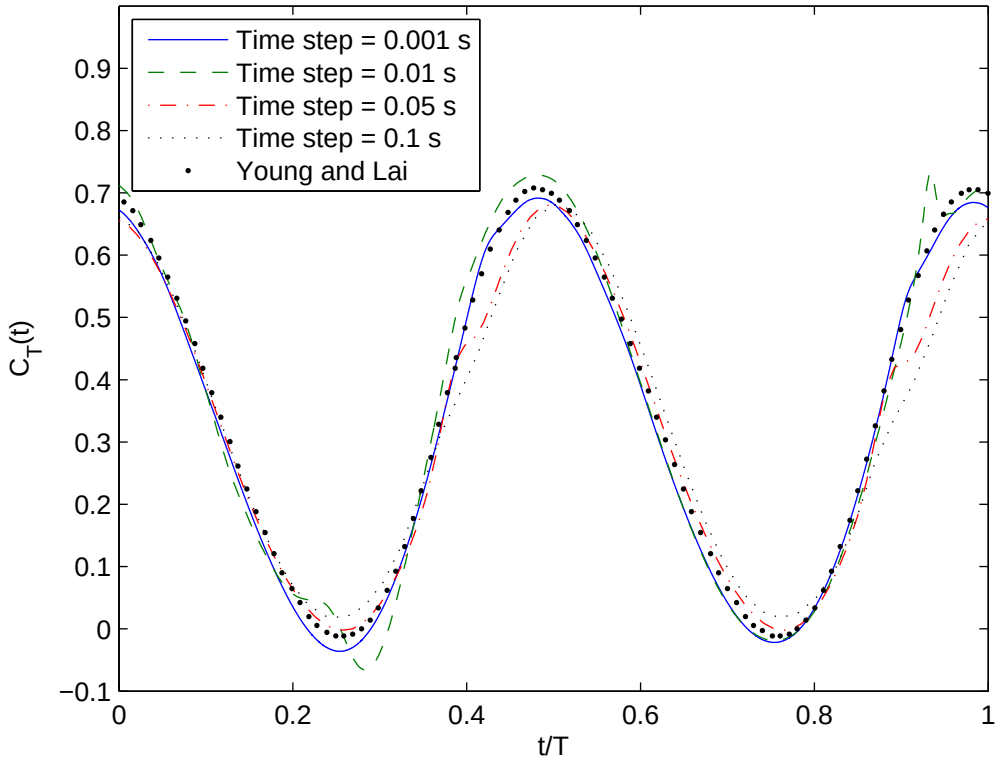

Figure 5.11: Time histories of thrust coefficient for different time-step sizes for single oscillating airfoil at $h = 0.175$, $k = 2.9$ and $Re = 20,000$. Numerical data for comparison from Young and Lai (2007) [14].

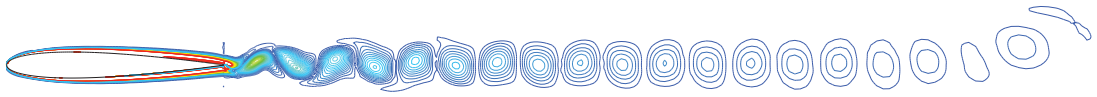

(a) Time-step set to $0.1s$.

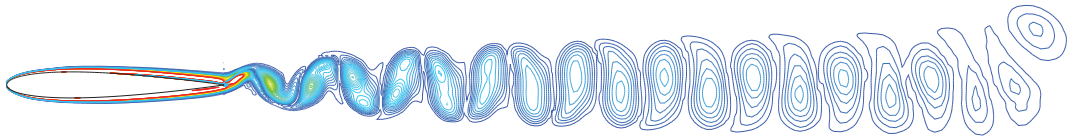

(b) Time-step set to $5{\cdot}10^{-2}s$.

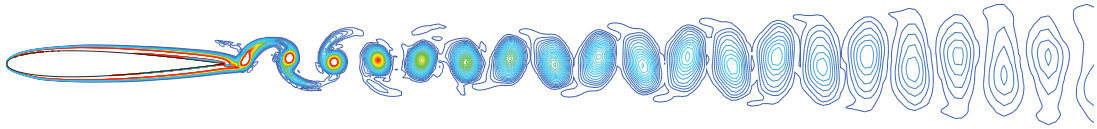

(c) Time-step set to $1{\cdot}10^{-2}s$.

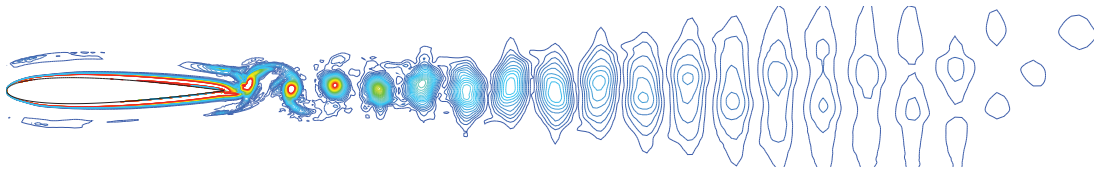

(d) Time-step set to $1{\cdot}10^{-3}s$.

Figure 5.12: Vorticity contour plots for single oscillating airfoil at $h = 0.0125$, $k = 7.8$ and $Re = 20,000$ for different time-steps.

(a) Time-step set to $0.1s$.

(b) Time-step set to $5{\cdot}10^{-2}s$.

(c) Time-step set to $1{\cdot}10^{-2}s$.

(d) Time-step set to $1{\cdot}10^{-3}s$.

Figure 5.13: Particle tracks for single oscillating airfoil at $h = 0.0125$, $k = 7.8$ and $Re = 20,000$ for different time-steps. The deformed wake structures to the far right in the figures are due to start-up effects of the simulations.

had different requirements for the laminar and the turbulent flows. However, time constraints would not allow for a significant increase in number of cells, and thus a grid independence study for the wake region for the turbulent flow was not performed. Results did not show any obvious signs of a too coarse grid, indicating that the grid used was of acceptable resolution and quality also for the turbulent flow.

5.2.1 Time-step size

In order to determine the time-step required for the turbulent flow, the number of iterations per oscillation period for the highest frequency for the laminar flow was used as a starting point. This resulted in a time-step of $2.8{\cdot}10^{-4}s$, and time-steps of $1{\cdot}10^{-2}s$, $5{\cdot}10^{-3}s$, $2{\cdot}10^{-3}s$ and $1{\cdot}10^{-3}s$ were investigated for the highest frequency for the turbulent flow. As seen in Figure 5.14 there are slight changes in the time-history plots for the different time-steps. For the two finest time-steps of $2{\cdot}10^{-3}s$ and $1{\cdot}10^{-3}s$ there are no clear differences, and thus a time-step of $2{\cdot}10^{-3}s$ was regarded as sufficiently fine. Time-histories of C_L, C_{Power} and C_T were all investigated for both the leading and trailing airfoils. But the results are not presented here as they showed the same trends as those seen in Figure 5.14.

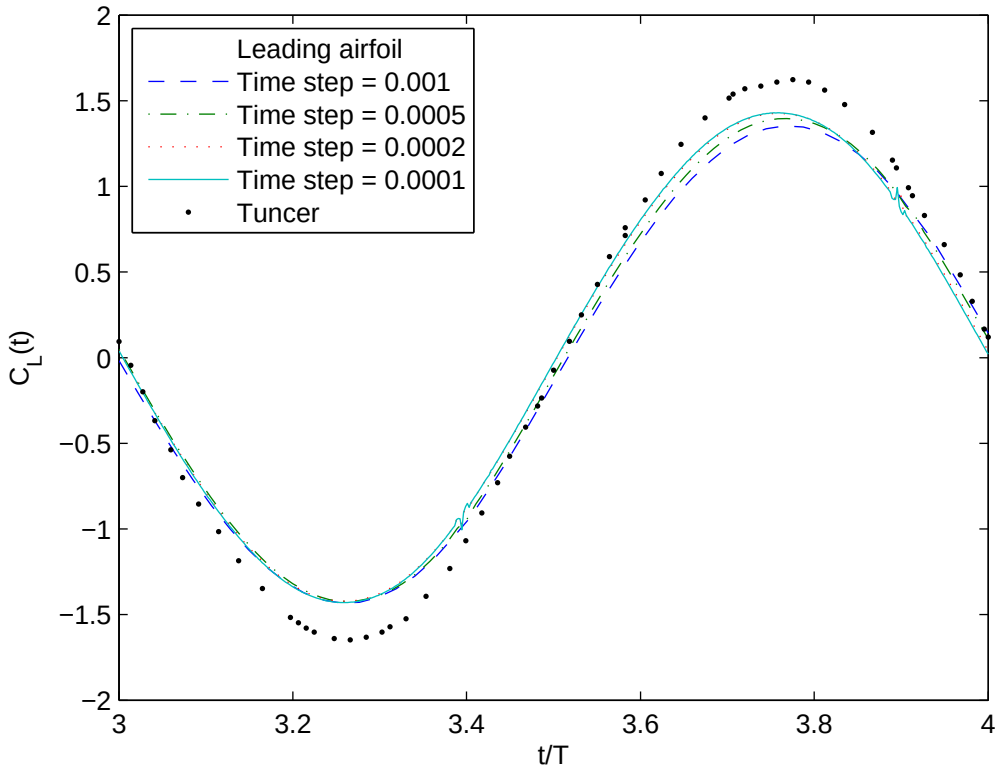

Figure 5.14: Time histories of lift coefficient for different time step sizes for tandem setup with leading airfoil oscillating at $h = 0.01$, $k = 1.5$ and $Re = 3,000,000$. Numerical data for comparison from Tuncer and Platzer (1996) [4].

Figures 5.15, 5.16, 5.17 and 5.18 present time-histories for one period of C_L

and C_T for both the leading and trailing airfoils. Comparisons are made with numerical studies performed by Tuncer et al. [4]. Since focus in this section is on model verification and validations, a thorough discussion of these results is not presented here. However, comparisons with other numerical studies are presented for the sake of verification of the model.

All four plots show similar behavior between the current study and that of Tuncer et al. [4]. Apart from the time history of the lift coefficient for the trailing airfoil (Figure 5.16) there are only quantitative differences in the plots. Tuncer et al. [4] used only at the pressure distributions to compute the lift and thrust, this can explain the high thrust values they achieved, as compared to this study. The cause of the artifacts in C_L near $t/T = 3.4$ and $t/T = 3.9$ for both the leading and trailing airfoil were not investigated.

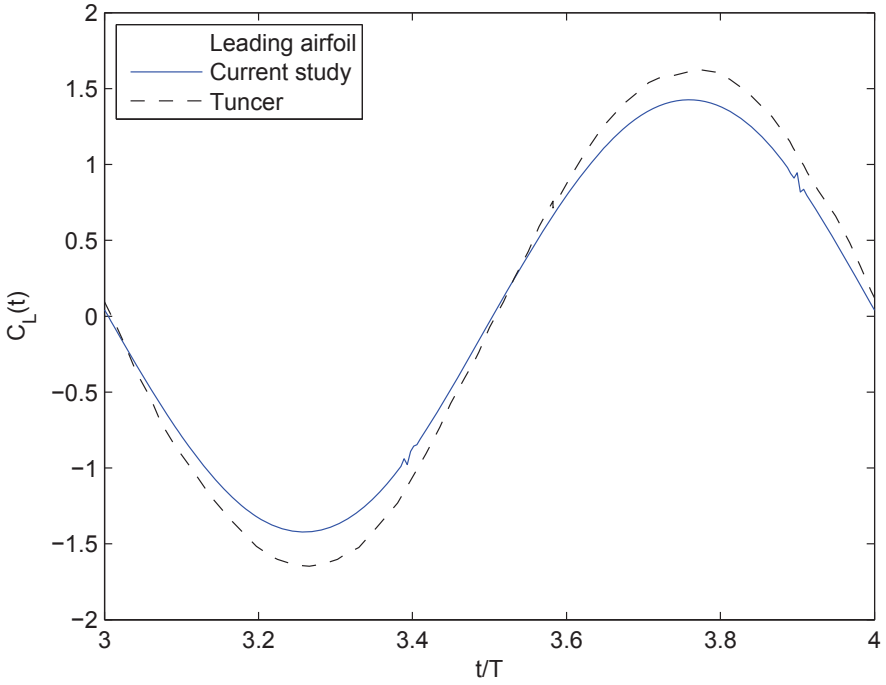

Figure 5.15: Time histories of lift coefficients for leading airfoil for tandem setup with leading airfoil oscillating at $h = 0.01$, $k = 1.5$ and $Re = 3,000,000$. Numerical data for comparison from Tuncer et al. (1996) [4].

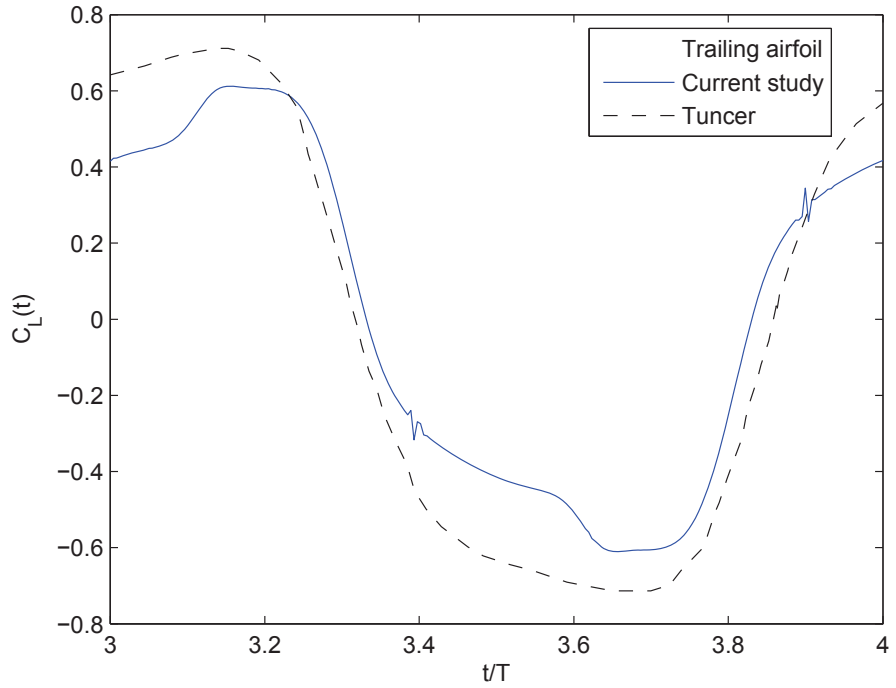

Figure 5.16: Time histories of lift coefficients for leading airfoil for tandem setup with leading airfoil oscillating at $h = 0.01$, $k = 1.5$ and $Re = 3,000,000$. Numerical data for comparison from Tuncer et al. (1996) [4].

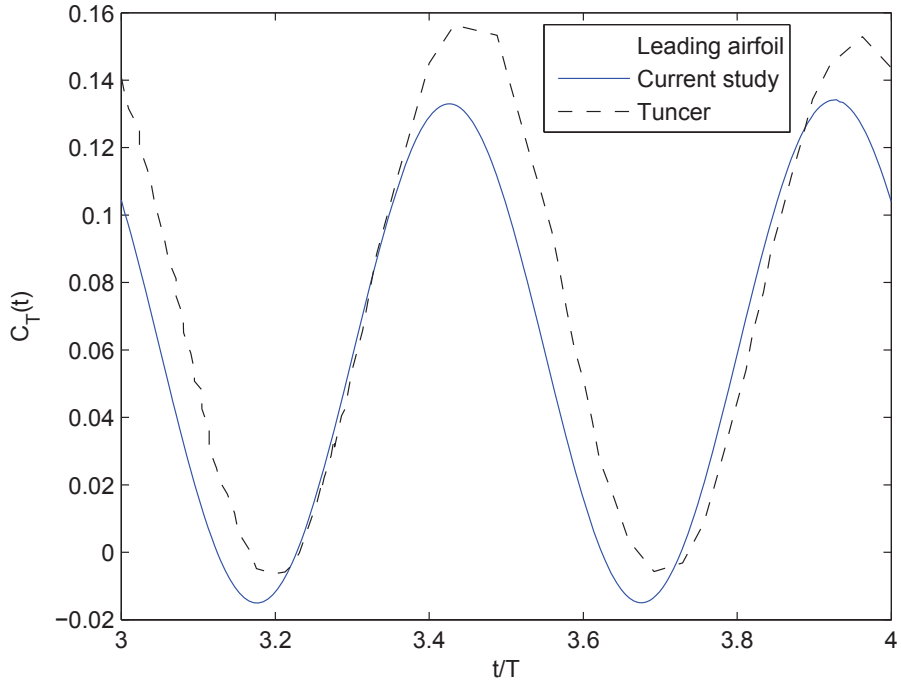

Figure 5.17: Time histories of thrust coefficients for leading airfoil for tandem setup with leading airfoil oscillating at $h = 0.01$, $k = 1.5$ and $Re = 3,000,000$. Numerical data for comparison from Tuncer et al. (1996) [4].

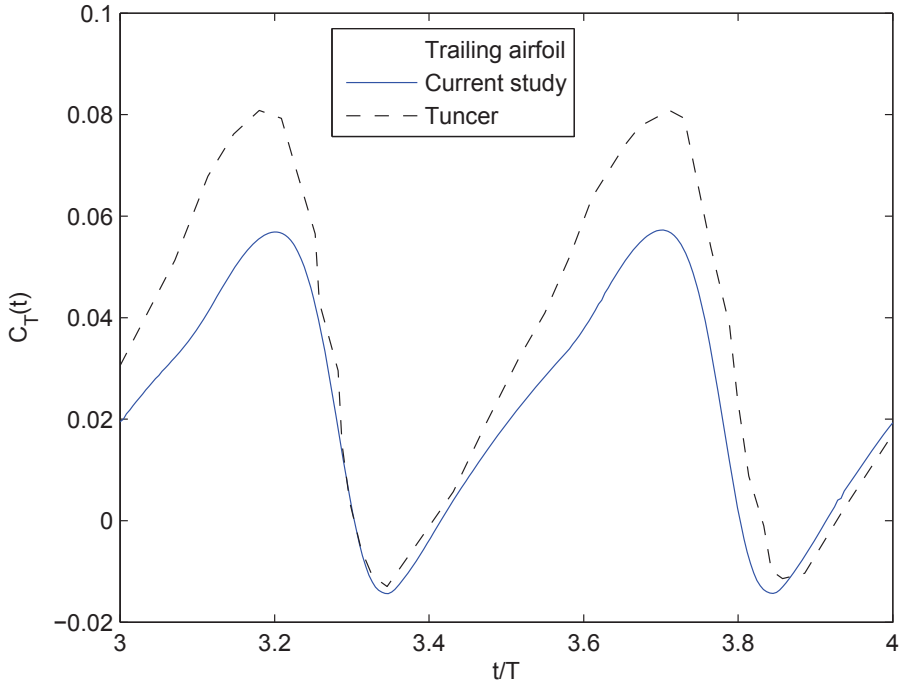

Figure 5.18: Time histories of thrust coefficients for trailing airfoil for tandem setup with leading airfoil oscillating at $h = 0.01$, $k = 1.5$ and $Re = 3,000,000$. Numerical data for comparison from Tuncer et al. (1996) [4].

Chapter 6

Results and discussion

6.1 Case setup

Several cases were investigated for the tandem setup with $X_{\text{shift}} = 1$ and $X_{\text{shift}} = 2$ at $Re = 3,000,000$. These parameters were set to match the numerical simulations performed by Tuncer and Platzer [4]. The reduced frequency k and the amplitude h for the initial simulations were also determined by the same study. In order to compare the performance of the NACA 0012 airfoil to the S809 airfoil, all cases were run for both airfoils. All cases presented in this chapter were run for ten periods of oscillation. This resulted in 2,390 iterations for the highest frequency and 17,923 iterations for the lowest frequency.

Initially, nine cases were investigated for four different setups: $X_{\text{shift}} = 1$ and 2 for both airfoils. The 36 cases provided information about where in the k-h plane more data were needed. After investigating the results, several extra simulations were performed, first for $X_{\text{shift}} = 1$ and then for $X_{\text{shift}} = 2$. These included more values of k for each investigated h value and in addition h was increased to achieve higher Sr numbers and to investigate the region in the k-h plane of maximum propulsive efficiency. For $X_{\text{shift}} = 1$, 37 additional cases were run for each airfoil, and for $X_{\text{shift}} = 2$, 6 additional cases were run for each airfoil.

To achieve a more detailed understanding of the results, three cases with $X_{\text{shift}} = 1$ where chosen for detailed investigations. The first had a Strouhal number in the lower range, the second a Strouhal number which gave close to optimal propulsive efficiency, and the third a Strouhal number in the upper range. An overview of the characteristic parameters for these three cases may be seen in Table 6.1. In these investigations, extensive data were extracted in time intervals equal to a tenth of a period; the data were gathered after the ninth period of oscillation.

Table 6.1: Values of k, h and Sr for the three cases chosen for detailed investigation.

	h	k	Sr
Case 1	0.3	0.20	0.038
Case 2	0.5	0.40	0.127
Case 3	0.9	0.60	0.344

6.2 Parameter dependency

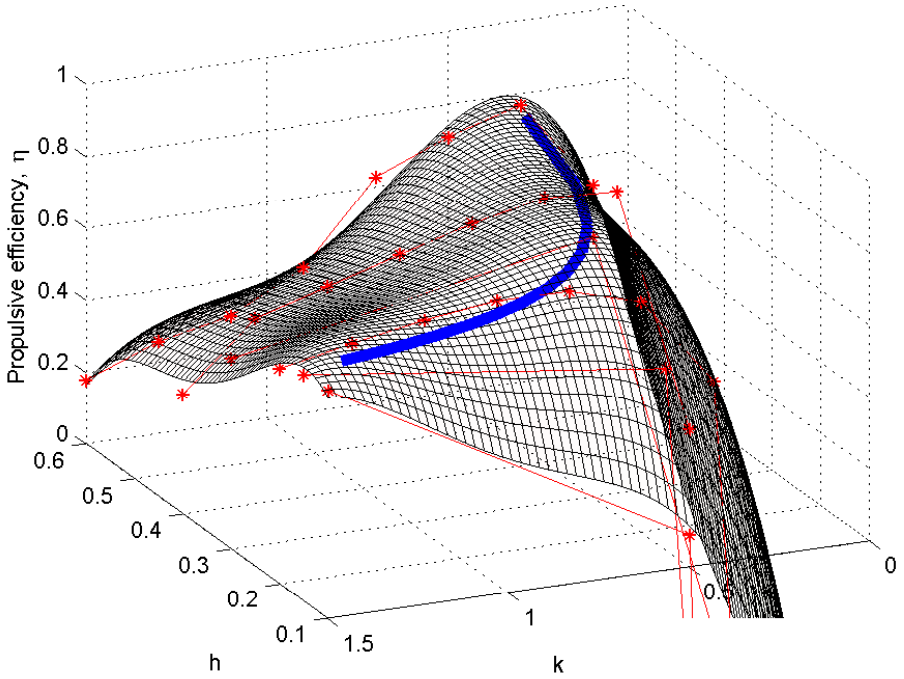

Figure 6.1: Plot of propulsive efficiency η (the red stars) vs. reduced frequency k and amplitude h for NACA 0012 tandem setup with $X_{\text{shift}} = 1$ at $Re = 3,000,000$. A fourth order regression surface and a line of Strouhal number of 0.1 (blue) are also included. Values below zero are not shown.

Figures 6.1 and 6.2 present the propulsive efficiency of all cases run for $X_{\text{shift}} = 1$ at $Re = 3,000,000$. There were less data available for the NACA 0012 airfoil than for the S809 airfoil, since some of the simulations diverged. Specifically, there was no data available for the NACA 0012 airfoil for any of the $h = 0.5$ cases nor for some of the $h = 0.3$ cases. The highest Sr values are found in the left part of the figure and the lowest Sr values are found in the right part of the figure. The blue lines follow an Sr value of 0.1 and an η value of 0.7. This line was added to visualize the partial dependency on the Sr number. In the area near this line, all the highest η values are found, for both airfoils. However, there is a trend of increasing η along this line, for increasing h and decreasing k. A global maximum for η was not found for either of the airfoils. The propulsive efficiency drops off for Sr values both above and below 0.1, as may be seen to the left and right of the blue line, respectively.

For $Sr < 0.03$ for the NACA 0012 airfoil and $Sr < 0.02$ for the S809 airfoil, the propulsive efficiency was negative, because drag, instead of thrust, was produced. Since the focus in this study was on thrust producing setups, these data points are not explicitly shown in any of the figures in this chapter.

The equations for the fourth order regression surfaces shown in Figure 6.1 and 6.2 were generated by use of the statistical analysis software Minitab 16.1.1. The

[1]Complete descriptions of the different R^2 values and the P values may be found in the Minitab software's StatGuide [43].

Table 6.2: Key results from the regression analysis performed on the data points in Figure 6.1 and 6.2. P values above 0.05 are in italic. The R^2(adj) and R^2(pred) values measures how well the model fits the data, the P value measures if the given term has a coefficient that is significantly different from zero.[1] Terms with P values below 0.05 are considered to have coefficients significantly different from zero. The higher the P value, the less important the given term is to the total fit of the model.

	NACA 0012	S809
R^2(adj)	94.6%	96.4%
R^2(pred)	69.1%	87.4%
Term	P	P
Constant	0.000	0.000
k	0.001	0.000
h	0.004	0.000
k^2	0.000	0.000
h^2	0.030	0.000
$k \cdot h$	*0.232*	0.000
k^3	0.000	0.000
h^3	*0.106*	0.000
$k \cdot h^2$	*0.242*	0.021
$k^2 \cdot h$	*0.810*	0.002
k^4	0.000	0.000
h^4	*0.230*	0.001
$k \cdot h^3$	0.034	0.021
$k^2 \cdot h^2$	*0.156*	*0.685*
$k^3 \cdot h$	*0.276*	0.001

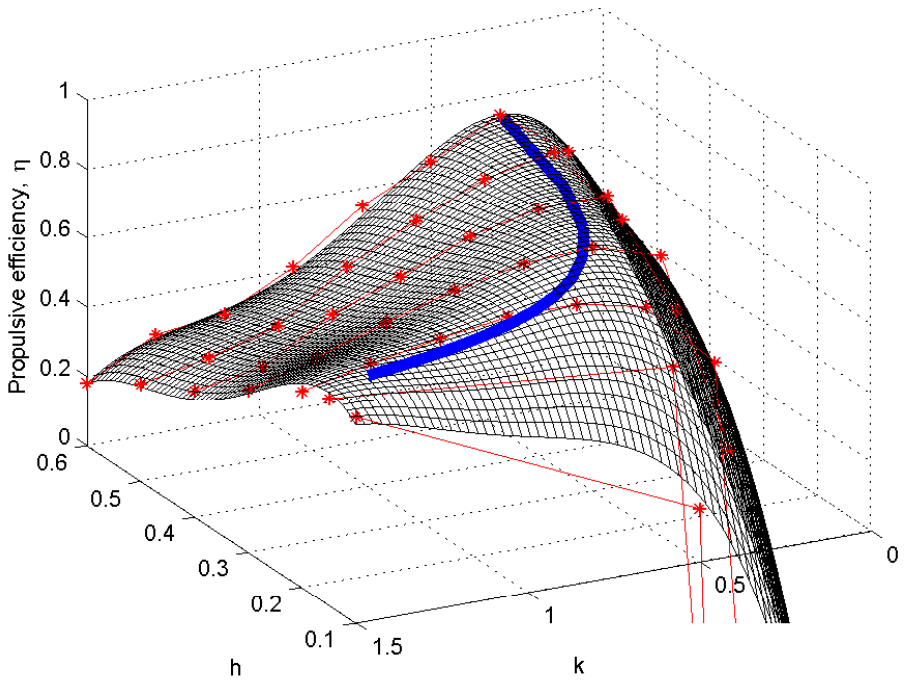

Figure 6.2: Plot of propulsive efficiency η (the red stars) vs. reduced frequency k and amplitude h for S809 tandem setup with $X_{\text{shift}} = 1$ at $Re = 3,000,000$. A fourth order regression surface and a line of Strouhal number of 0.1 (blue) are also included. Values below zero are not shown.

full output from the regression analysis is given in Appendix C, key aspects of the results are presented in Table 6.2.

For the S809 airfoil, all terms in the regression analysis, except the $k^2{\cdot}h^2$(which is proportional to Sr^2) term, have P values below 0.05. For the NACA 0012 airfoil all terms of order three or higher, except the three terms k^3, k^4 and $k{\cdot}h^3$, have P values above 0.05. Both airfoils show a fourth order dependency in the pure k terms, while in the pure h terms the S809 airfoil shows a fourth order dependency and the NACA 0012 airfoil shows only a significant second order dependency. The S809 data show a significant dependency in the Strouhal number term $k{\cdot}h$ while the NACA 0012 data do not significantly show this dependency.

Figure 6.3 shows η values for three different k values that all correspond to $Sr = 0.1$. This illustrates both the need to specify k (or h) in addition to Sr, as well as the increase in η for decreasing k for similar Sr. The reasons for the latter will be discussed in detail in Section 6.3.1.

Figures 6.4 and 6.5 show the same data as depicted in Figure 6.1 and 6.2, only in two dimensions with different h values plotted along the same k axis. It is evident in these figures how the peak in η for the different h move towards lower k values as h increases. The highest propulsive efficiency was found for $k = 0.3$ and $h = 0.6$ ($Sr = 0.11$) for both airfoils with $\eta = 0.766$ for the NACA 0012 airfoil and $\eta = 0.742$ for the S809 airfoil.

Figure 6.6 shows only $h = 0.2$ and includes data from Tuncer and Platzer [4]. The trends in their data are the same as the trends in the data from this study. The peak η values are close to each other, but there is a shift in the k dependency.

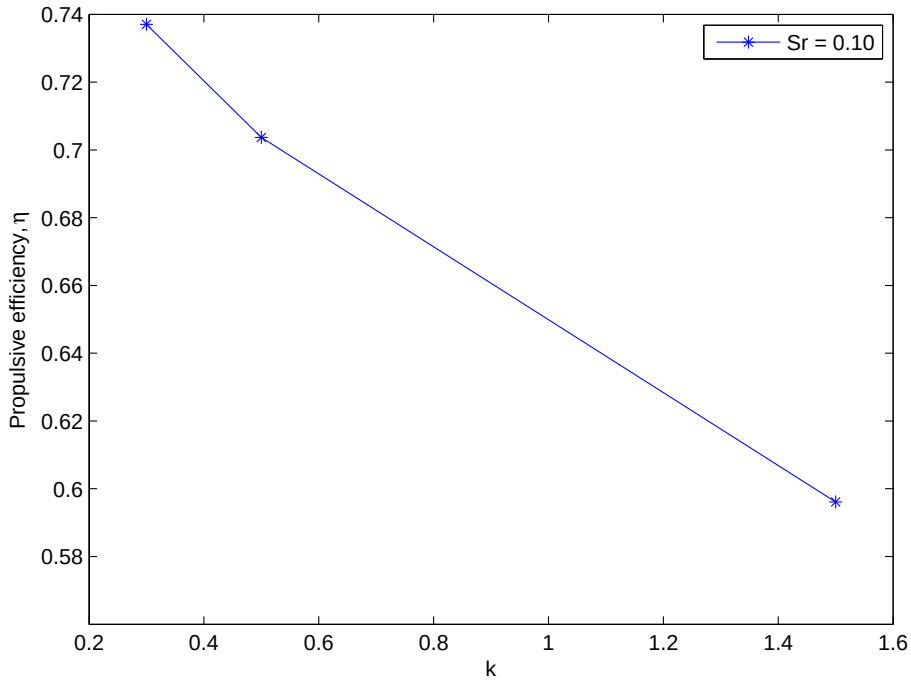

Figure 6.3: Propulsive efficiency η vs. reduced frequency k for $Sr = 0.1$ for the S809 tandem setup with $X_{\text{shift}} = 1$.

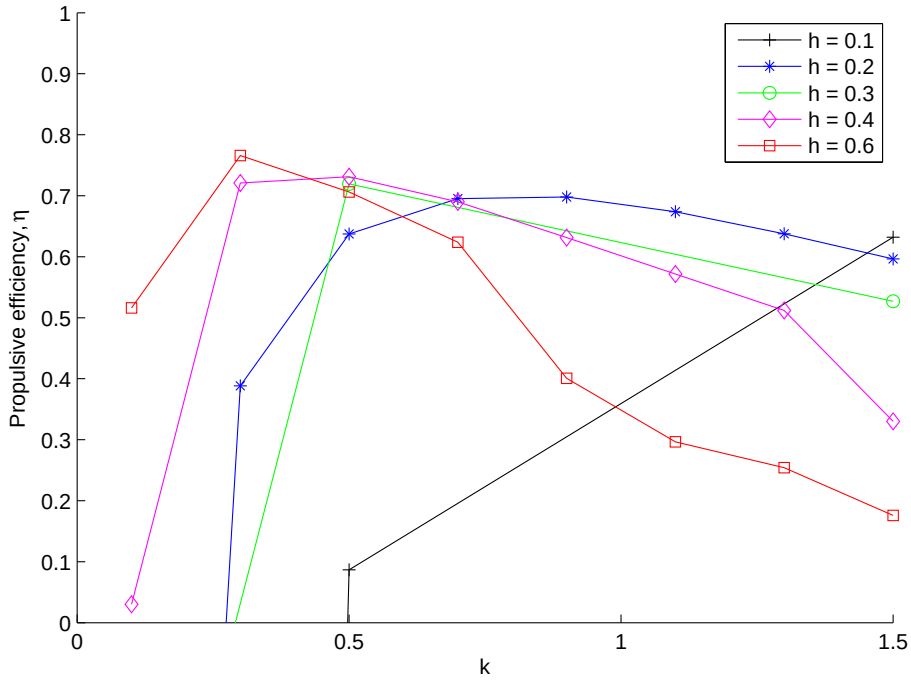

Figure 6.4: Plots of propulsive efficiency η vs. reduced frequency k for different amplitudes h for NACA 0012 tandem setup with $X_{\text{shift}} = 1$ at $Re = 3,000,000$. Values below zero are not shown.

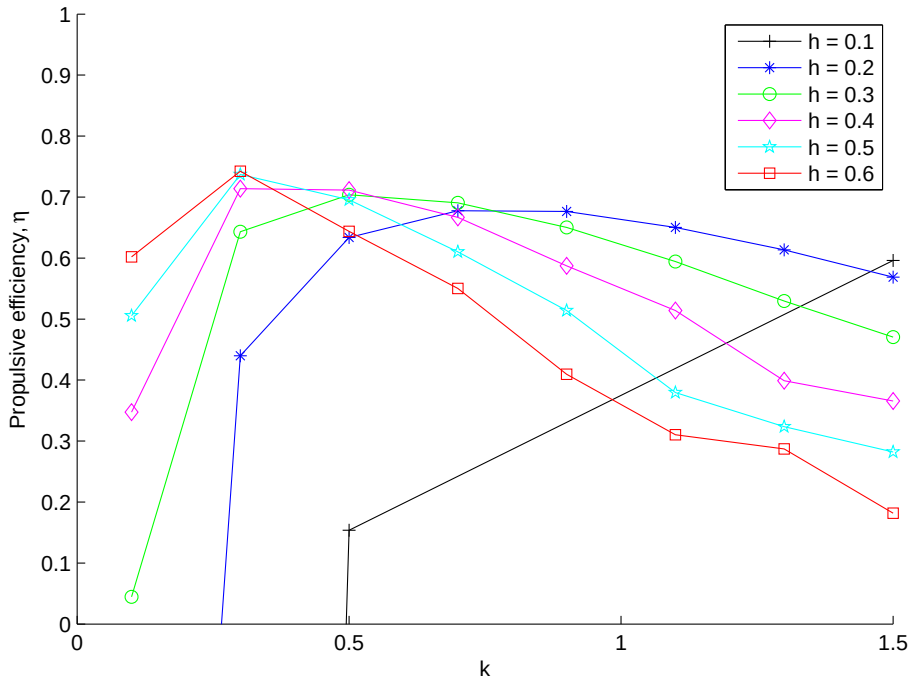

Figure 6.5: Plots of propulsive efficiency η vs. reduced frequency k for different amplitudes h for S809 tandem setup with $X_{\text{shift}} = 1$ at $Re = 3,000,000$. Values below zero are not shown.

Tuncer and Platzer achieved positive η for $k = 0.1$, while the present study obtained negative η values for the same k. This figure also shows the similarity in the results from the NACA 0012 airfoil and the S809 airfoil.

Figure 6.7 shows the same data as presented above with η as a function of Sr and not k and h, thus showing that the Strouhal number can be used as a describing parameter. For the $X_{\text{shift}} = 1$ data, all points to the right of the blue line in Figure 6.1 and 6.2 are in Figure 6.7 to the left of $Sr = 0.1$ and all the data to the left of the blue lines are to the right of $Sr = 0.1$. The plots have jagged shapes due to similar (or even identical) Strouhal numbers producing significantly different η values. These data points were generated from different k and h values, but their product $k \cdot h$ (and thus also Sr) is close to the same. The jagged shape demonstrates how the Strouhal number is not the only describing parameter necessary.

The data for $X_{\text{shift}} = 2$ show the same trends as the $X_{\text{shift}} = 1$ data. The efficiency increases quickly from negative values as Sr increases from zero, reaches a peak and then more slowly approaches zero for higher Sr values. As was the case for $X_{\text{shift}} = 1$, the peak occurs for $k = 0.3$ and $h = 0.6$ ($Sr = 0.11$) for both airfoils, with $\eta = 0.760$ for the NACA 0012 airfoil and $\eta = 0.736$ for the S809 airfoil. A higher h value than 0.6, might produce even higher η values, but the k-h combinations were chosen to match those that were investigated for $X_{\text{shift}} = 1$.

The NACA 0012 airfoil achieved higher values in efficiency than the S809 airfoil for both X_{shift} values. Also, the $X_{\text{shift}} = 1$ cases gave higher η values than the $X_{\text{shift}} = 2$ cases for both airfoils.

Tuncer and Platzer [4] found for $k = 0.75$ and $h = 0.2$ ($Sr = 0.10$) that there

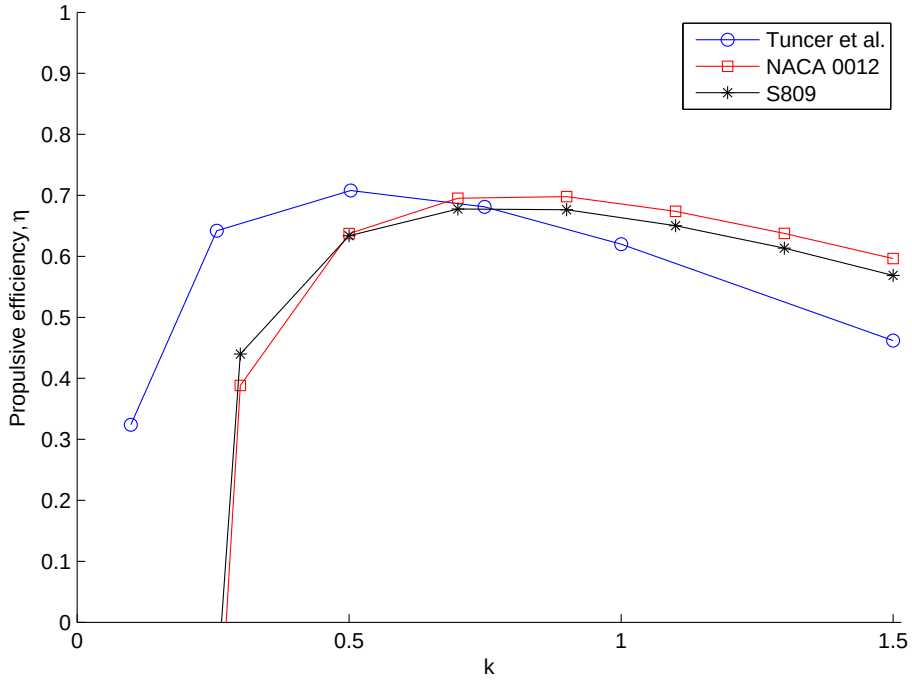

Figure 6.6: Plots of propulsive efficiency η vs. reduced frequency k for amplitude $h = 0.2$ for tandem setups with $X_{\text{shift}} = 1$ at Reynolds number of $3,000,000$. Values below zero are not shown.

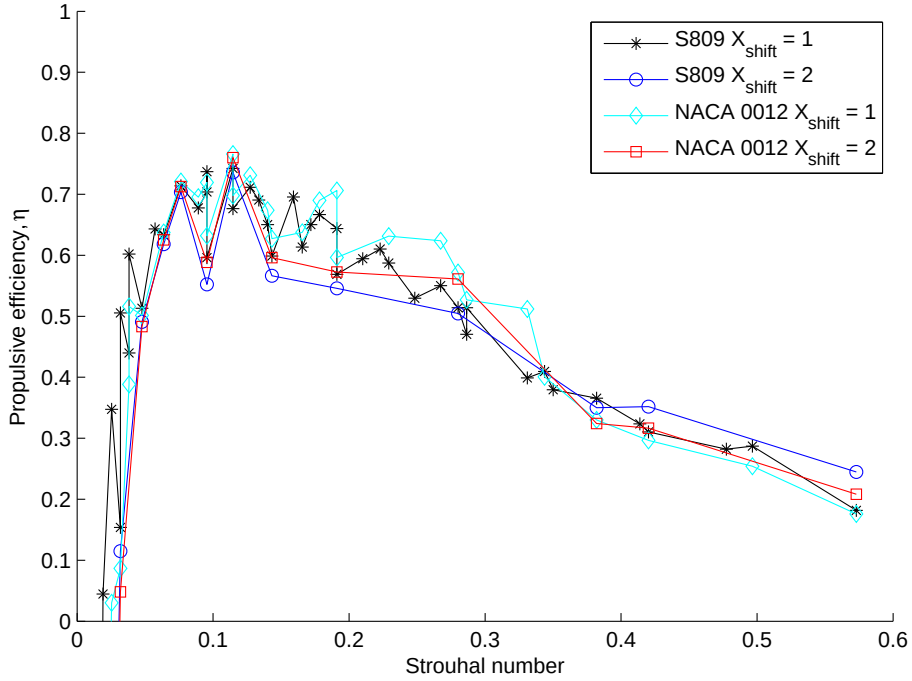

Figure 6.7: Propulsive efficiency η vs. Strouhal number for the four different tandem setups. Values below zero are not shown.

were small differences between $X_{\text{shift}} = 0.65$, 1, 1.5, 2 and 3, with $X_{\text{shift}} = 2$ giving the highest η. The results from this study supports that there are not big differences in η for different X_{shift} values, but a peak η for $X_{\text{shift}} = 1$ and not $X_{\text{shift}} = 2$ was achieved.

6.2.1 Comparison of airfoils

Both airfoils investigated in this study showed similar results. The NACA 0012 airfoil achieved a slightly higher maximum propulsive efficiency ($\eta = 0.766$) than the S809 airfoil ($\eta = 0.742$). This is believed to be connected to the symmetry of the setup. The NACA 0012 airfoil does not distinguish between an upstroke and a downstroke while the S809 airfoil is designed specifically for positive angles of attack, and will not behave optimally for negative angles of attack. This is backed up by time-histories of the thrust coefficient, as seen in Figure 6.10 where the S809 airfoil reaches a smaller thrust during the upstroke, where negative angles of attack occur, than during the downstroke.

According to the regression analysis (results shown in Table 6.2 and Appendix C), the S809 airfoil was dependent on more parameters than the NACA 0012 airfoil. This is assumed to be mostly because of more data points being available for the S809 airfoil.

The regression analysis was not performed in a rigerous manner, as this would be beyond the scope of this study. The surfaces that fitted the data best are presented here. These surfaces could be overfitted, which would lead to too high order dependencies in the data.

6.3 Tandem setup performance

In order to investigate the tandem setup in detail, three cases for the S809 airfoil were chosen for analysis. These cases were presented in Table 6.1 and their results are presented and discussed in the remainder of this chapter.

Table 6.3: Comparisons of propulsive efficiencies for tandem setup to single airfoil setup.

k	h	Sr	Single	Tandem	Increase
0.3	0.4	0.038	0.465	0.439	-5 %
0.5	0.4	0.127	0.552	0.711	29 %
0.9	0.6	0.344	0.301	0.407	35 %

As seen in Table 6.3, the tandem setup was able to outperform the single airfoil setup. Details about the effect of the second, trailing, airfoil may be found in Section 6.4, while this section focuses on the overall performance of the setup.

Figure 6.8 shows how the leading airfoil experiences an apparent angle of attack due to its oscillating motion. The free stream velocity is horizontal, while the velocity vectors near the airfoil's nose is pointing in a diagonal direction. In the lower right corner of the figure, it can be seen how there is a sudden change in the direction of the velocity vectors. This is a result of the airfoil "pulling" the

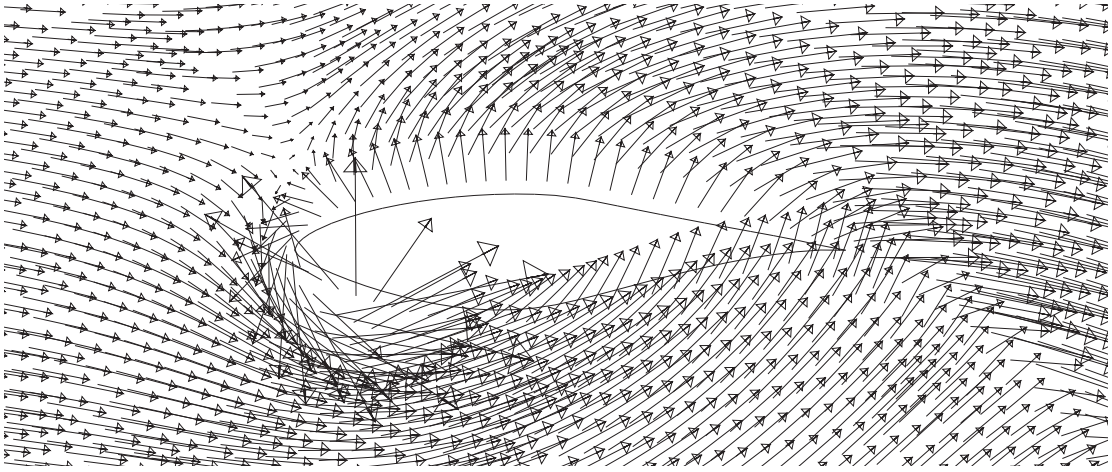

Figure 6.8: Selected velocity vectors for leading airfoil at $Sr = 0.344$ halfway through an upstroke.

fluid elements upwards as it performs its upward stroke. Thus the fluid elements' velocity vectors get a vertical component in addition to their origial horizontal component. This "wake edge" will eventually hit the trailing airfoil (discussed later). The LEV near the airfoil's nose may also be seen in the same figure.

Figures 6.1 and 6.2 indicate that the global maximum propulsive efficiency was not found in this study. A higher η value could be expected for a higher amplitude h, than the maximum of 0.6 investigated in this study. Figure 6.7 indicates that the global maximum η might have been found. But as is also evident in the figure, there are jumps in η for Sr values close to each other, and no conclusion can be made about the global maximum η for this setup. However, the global maximum will have at least $\eta = 0.742$ for the S809 airfoil and at least $\eta = 0.766$ for the NACA 0012 airfoil according to this study.

Figure 6.9 shows different coefficients for the S809 airfoil tandem setup; the η plot may be seen in greater detail in Figure 6.7, but is redrawn in this figure for clarity. The figure shows the steady increase in C_{Power} as Sr increases. However, the thrust coefficient C_T reaches a maximum close to $Sr = 0.5$ and declines for higher Sr. More data for high Sr values would be needed to confirm a global maximum for the C_T coefficient. It is evident from Figure 6.9 that a C_T value of 2.32 can be achieved for this setup if power requirements are not a constraint. In contrast, the thrust coefficient was 0.21 for the Sr with maximum η.

The quick drop in η for low Sr values is a result of C_T reaching zero and becoming negative for low Sr values. Since C_T slowly approach zero for higher values of Sr, there is a slow decline in η in the region to the right of maximum η. The decline in η is due to C_{Power} increasing at a higher rate than C_T.

Figures 6.10, 6.11 and 6.12 show time-histories for the tenth period of oscillation for different Strouhal numbers. The thrust and lift coefficients for $Sr = 0.038$ are not plotted, as they were both close to constant.

A high degree of periodicity was found in the time-histories of C_L, C_T and C_{Power}, and thus time-histories for only one period of oscillating motion are shown here.

Both the leading and trailing airfoil at $Sr = 0.344$ produce higher thrust

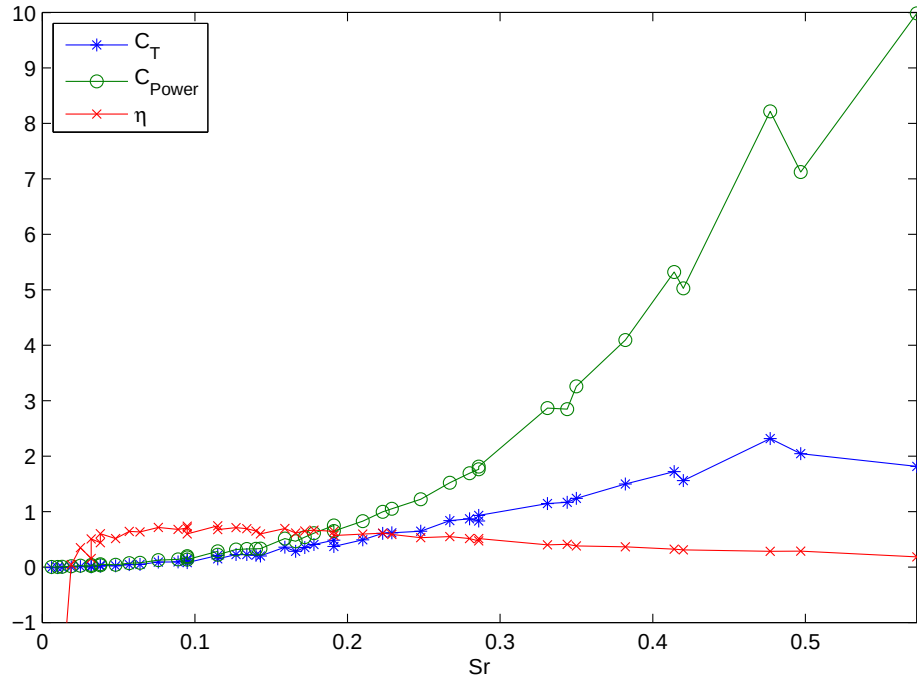

Figure 6.9: Plots of thrust coefficient C_T, power coefficient C_{Power} and propulsive efficiency η for the S809 $X_{\text{shift}} = 1$ data. Values below -1 are not shown.

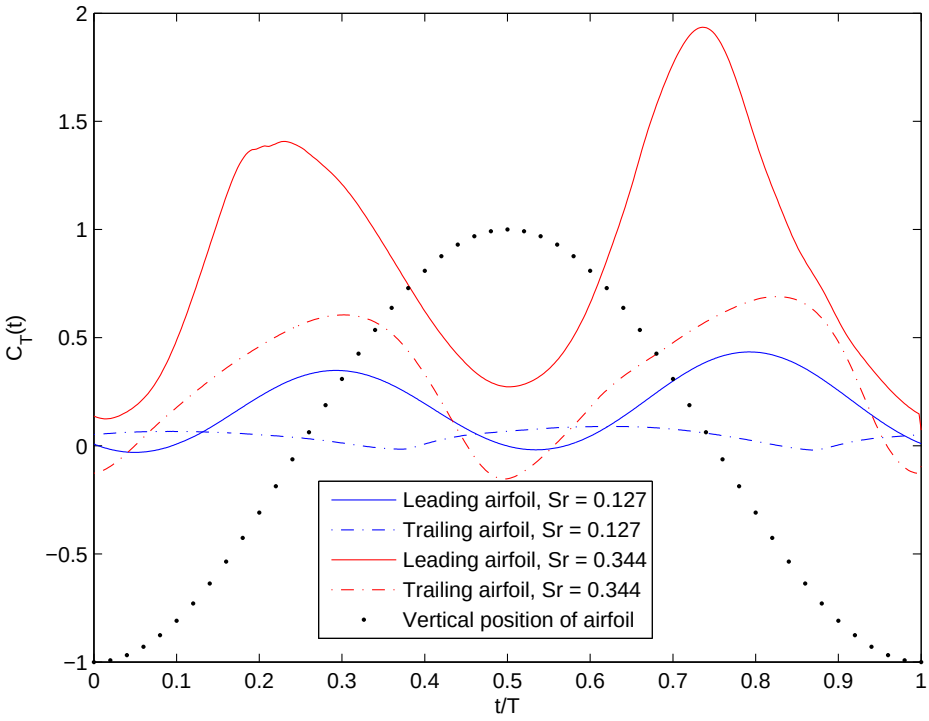

Figure 6.10: Time histories for thrust coefficients for the S809 airfoil. Data for the tenth period of simulation is shown.

than both the airfoils at $Sr = 0.127$. Thrust is produced during the upstroke and the downstroke, and reaches its peaks during the maximum plunge velocity for the leading airfoil. The peaks in thrust for the trailing airfoil do not occur simultaneously, but are offset by a shift that is dependent on the Strouhal number. For both Sr, the peaks are higher during the downstroke than during the upstroke.

The periodicity in the lift coefficient follow that of the oscillating motion; negative lift is generated during the upstroke and positive lift is generated during the downstroke. The same trends observed for the thrust coefficient are evident in the lift coefficient plot: The amplitudes for $Sr = 0.344$ are higher than those for $Sr = 0.127$ and the peaks for the trailing airfoils are offset from the peaks for the leading airfoils.

Figure 6.12 shows time-histories of C_{Power}, defined as

$$C_{\text{Power}} = -C_L \frac{y_{\text{vel}}}{U_0}, \tag{6.1}$$

only for the leading airfoil, since the trailing airfoil is stationary. The C_{Power} follows the periodicity of the thrust, i.e. twice the frequency of the oscillation frequency. In this figure, it is evident that the power requirements to move the airfoil increases drastically as the Sr value increases.

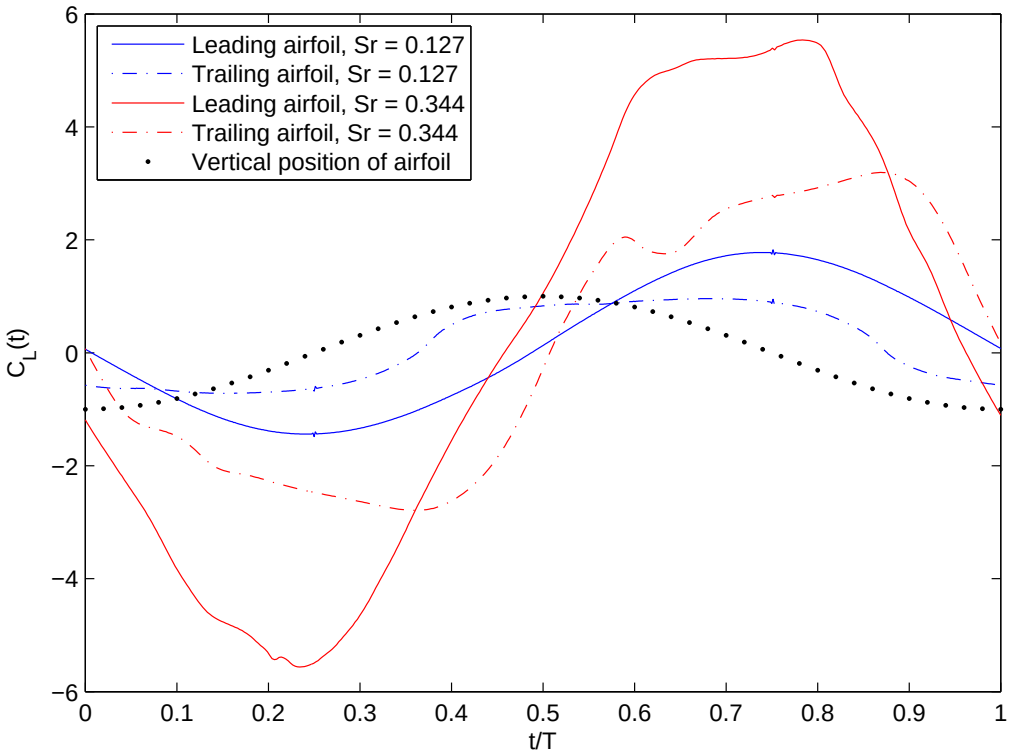

Figure 6.11: Time histories for lift coefficients for the S809 airfoil. Data for the tenth period of simulation is shown.

Table 6.4 shows the viscous drag forces as compared to pressure forces for peak thrust values during an upstroke. As seen, the viscous and pressure forces are of comparable magnitudes for low Sr, while the pressure forces dominates for the high Sr.

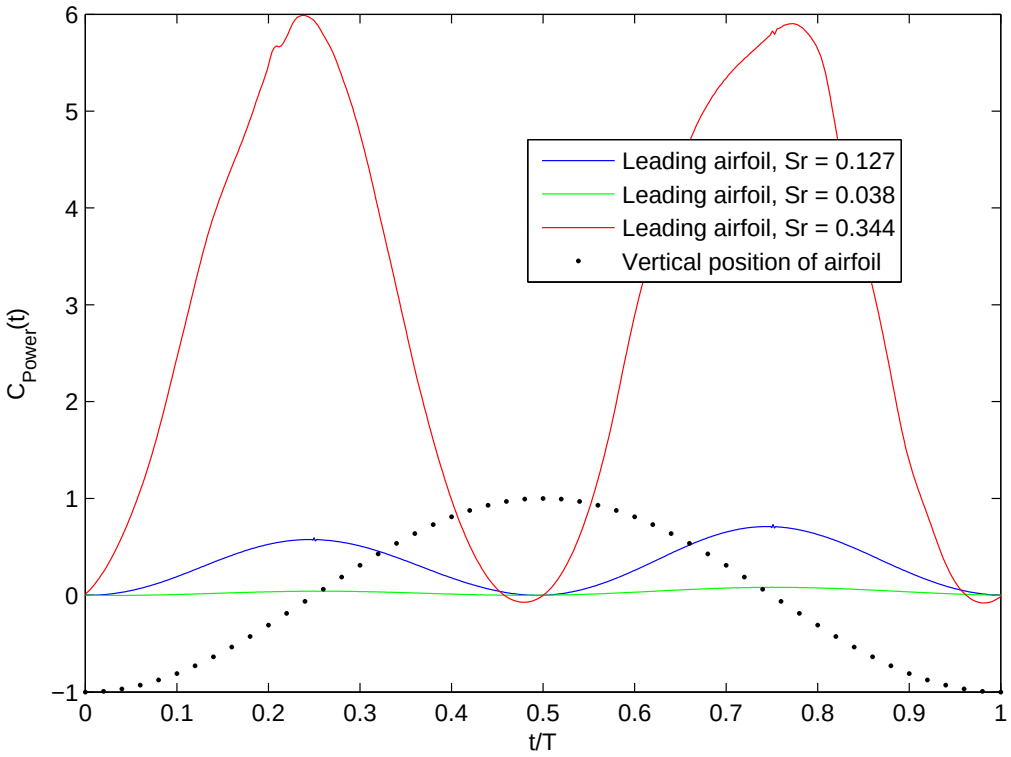

Figure 6.12: Time histories for power coefficients for the S809 airfoil. Data for the tenth period of simulation is shown.

Table 6.4: Force coefficients in negative x-direction for leading and trailing airfoils for different Sr. Positive values for thrust, negative values for drag. Data extracted when the two airfoils were aligned in the vertical direction during an upstroke.

	$Sr = 0.038$		$Sr = 0.127$		$Sr = 0.344$	
	Leading	Trailing	Leading	Trailing	Leading	Trailing
Pressure	0.027	−0.004	0.310	0.047	1.399	0.539
Viscours	−0.005	−0.005	−0.006	−0.007	0.006	−0.007
Total	0.023	−0.009	0.304	0.040	1.406	0.532

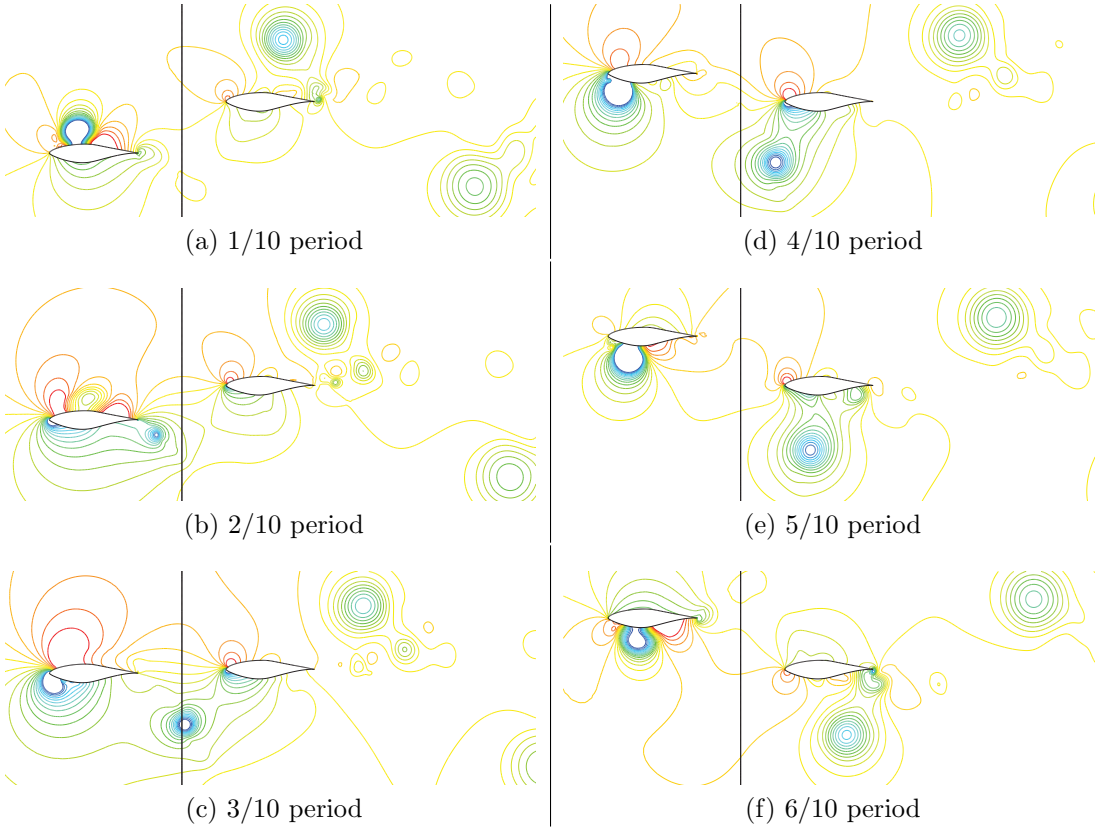

(a) 1/10 period (d) 4/10 period

(b) 2/10 period (e) 5/10 period

(c) 3/10 period (f) 6/10 period

Figure 6.13: C_{Pressure} contour plots for an upstroke for the S809 airfoil. $k = 0.9$ and $h = 0.6$ ($Sr = 0.344$). Colored by magnitude: Dark blue = -5 and red = 2.

6.3.1 Leading edge vortex (LEV) shedding

The shedding of vortices had a profound effect on the tandem setups performance. The leading edge vortex (LEV) shedding of the leading airfoil had the highest impact on both the leading airfoil itself as well as the tandem setup as a whole. The trailing edge vortex (TEV) shedding, on the other hand, of the leading airfoil was important for the performance of the trailing airfoil. This section discusses LEV shedding, while TEV shedding is discussed in Section 6.4.1.

Figure 6.13 and 6.14 show C_{Pressure} contour plots and C_{Pressure} plots, respectively, for an upstroke of the leading airfoil. In the first two frames of Figure 6.14 the LEV on the upper side of the airfoil, that was formed during the preceding downstroke, is seen as a large bump in the pressure distribution. This LEV may also be seen in Figure 6.13. In the third frame, this LEV and its effects on the airfoil have vanished.

The LEV formed during the upstroke starts to form in the second frame of both figures. As a result there is a suction peak at the nose of the airfoil (close to $x/C = 0$). The LEV shedding is of the high-speed vortex shedding mode (explained in Section 2.9): The vortex reaches its maximum size while almost not traveling downstream and decays as it starts to travel downstream after its peak in size is reached. This may be observed in Figure 6.14 and 6.13. These are desired effects, since both the highest thrust as well as the highest thrust-to-lift ratios are achieved for suction close to the airfoil nose. These effects are results of

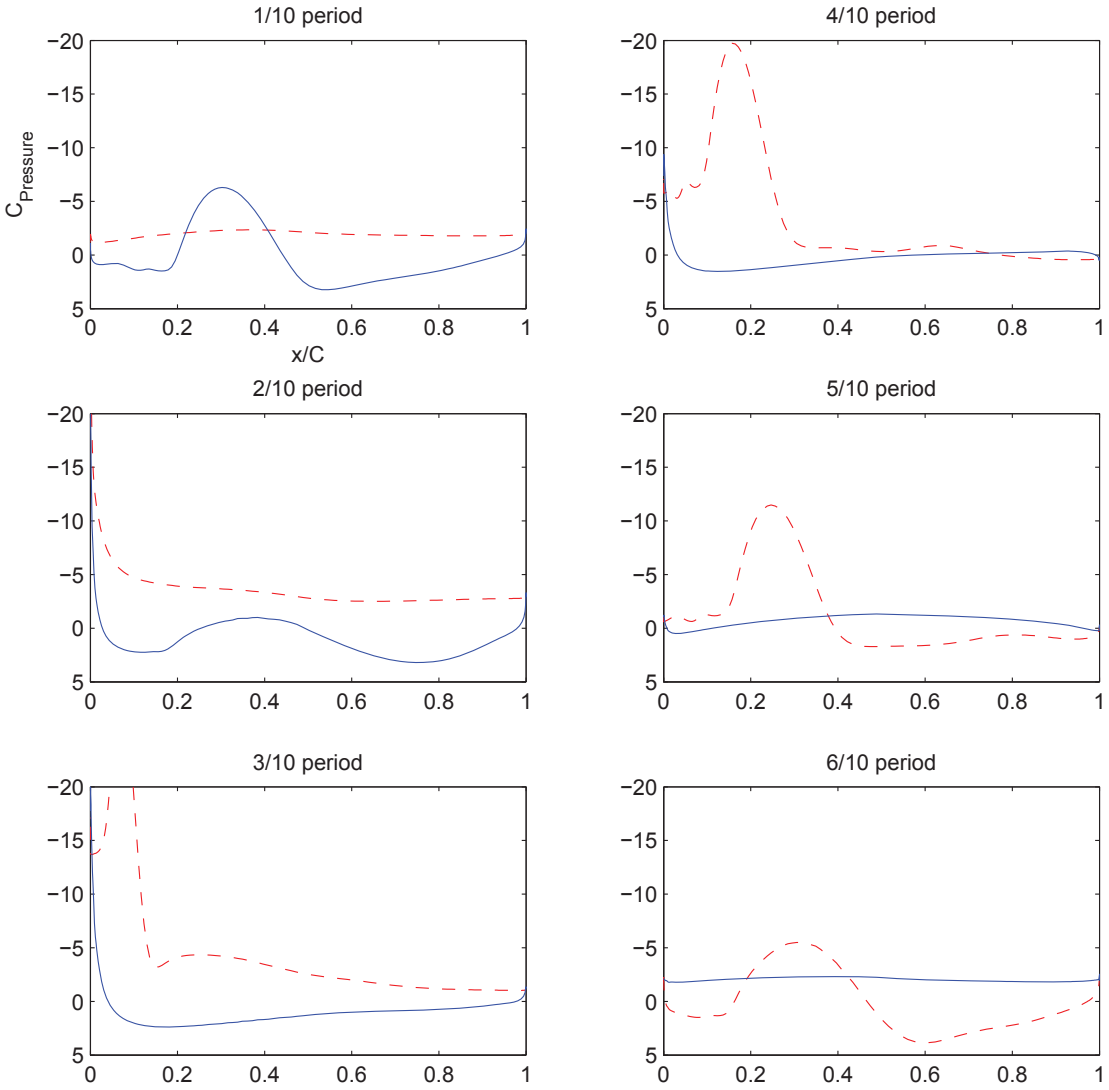

Figure 6.14: Plots of pressure coefficients for the leading airfoil. $k = 0.9$ and $h = 0.6$ ($Sr = 0.344$). Solid line: Upper side of airfoil, dashed line: Lower side of airfoil.

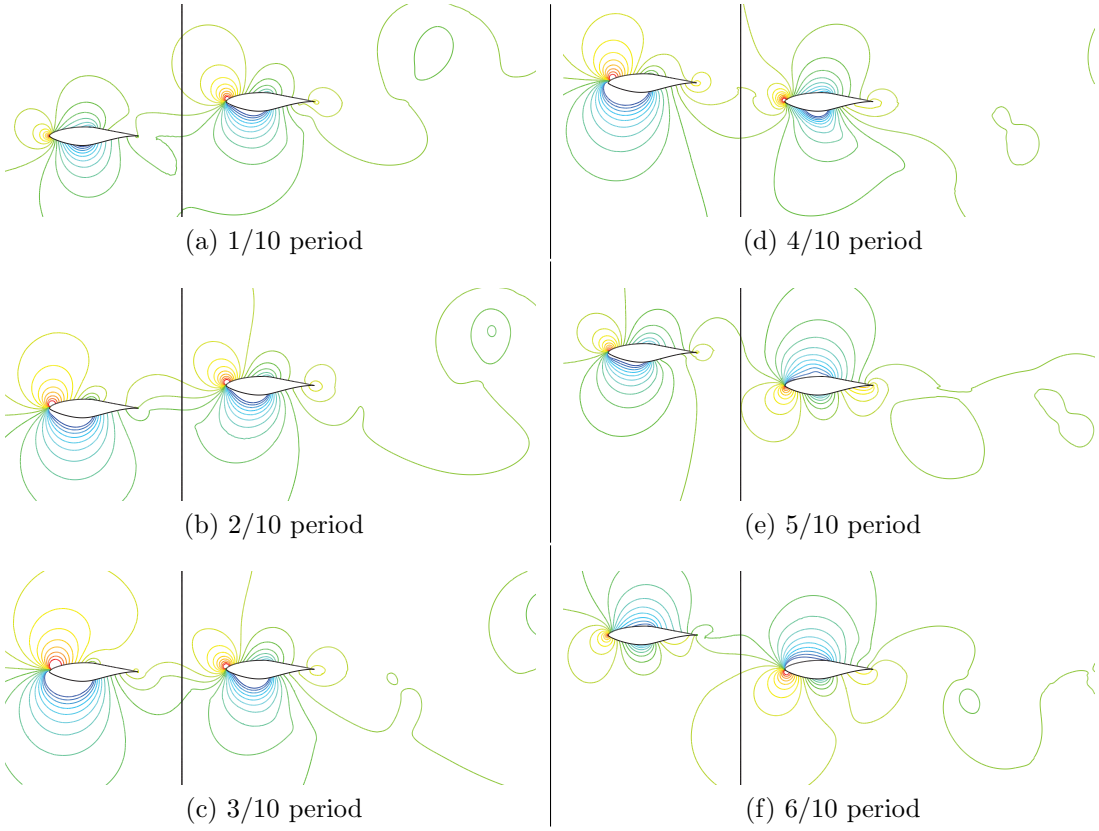

(a) 1/10 period (d) 4/10 period

(b) 2/10 period (e) 5/10 period

(c) 3/10 period (f) 6/10 period

Figure 6.15: C_{Pressure} contour plots for an upstroke for the S809 airfoil. $k = 0.5$ and $h = 0.4$ ($Sr = 0.127$). Colored by magnitude: Dark blue $= -1$ and red $= 1$.

the surface normal pointing almost horizontally upstream in this area. It is also desirable for the LEV to decay completely when it reaches the top (the highest point) of the airfoil. Near the top or the bottom of the airfoil the LEV only generates lift, which acts in the opposite direction of the airfoil motion, and thus increases the power requirements to move the airfoil (C_{Power}). If the LEV reaches the rear of the airfoil, it will contribute to drag production as well as the undesired lift production. This explains the peak in C_T for high Sr values (as was observed in Figure 6.9); for Sr values above this peak there is enough time for the LEV to travel to the drag-producing region of the airfoil.

In the last frame, the pressure distribution is almost identical to that of the first frame, only now the upper and lower sides are switched. Since the sequence repeats itself for the downstroke in a similar fashion, illustrations of the downstroke were not included.

Thrust can be generated either by suction near the nose of the airfoil or pressure at the rear of the airfoil. As the low pressures in the LEVs were of much higher magnitudes than any net pressure that could occur near the rear of the airfoil, the LEVs were the main cause of thrust generation for the leading airfoil. In Figure 6.14, it is evident that the suction peak building up right before a LEV is formed, also contributes greatly to the thrust. This is important to note, as LEV shedding does not occur for the lower Sr values, but the pre-LEV-shedding suction peak will occur even for the lower values of Sr.

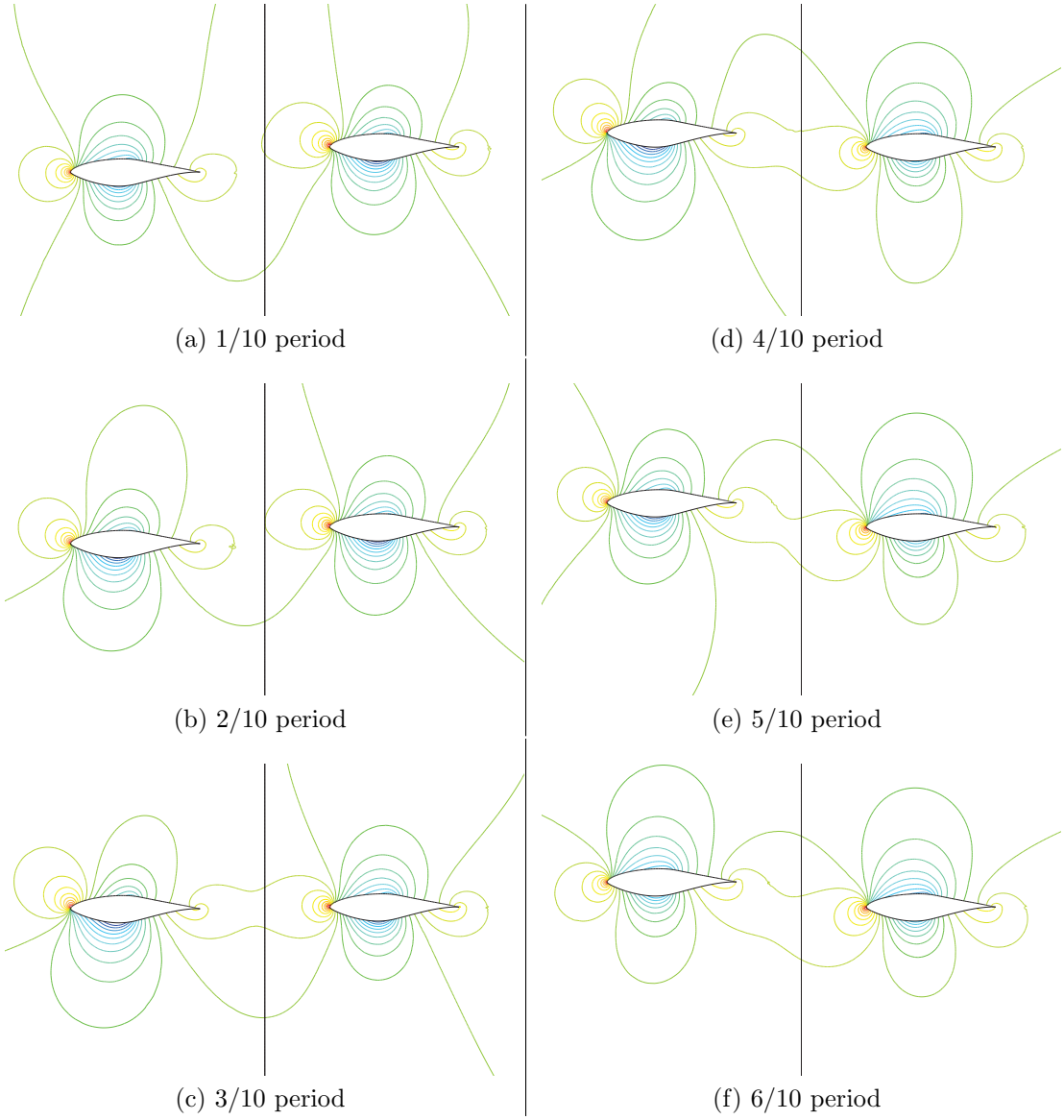

(a) 1/10 period (d) 4/10 period

(b) 2/10 period (e) 5/10 period

(c) 3/10 period (f) 6/10 period

Figure 6.16: C_{Pressure} contour plots for an upstroke for the S809 airfoil. $k = 0.3$ and $h = 0.2$ ($Sr = 0.038$). Colored by magnitude: Dark blue $= -1$ and red $= 1$.

This phenomenon is evident in Figure 6.15, which shows C_{Pressure} contour plots for an upstroke of the leading airfoil for $Sr = 0.127$. Frames two through four show how a LEV starts to form near the nose of the airfoil, but is never fully developed. Still, this k-h combination results in one of the highest propulsive efficiencies achieved in this study ($\eta = 0.711$). Since the low pressure region in this case does not move downstream, it always contributes significantly to thrust (as well as the undesired lift contribution), whereas the LEVs for the high Sr values only contribute significantly to thrust before they start to travel downstream.

Figure 6.16 shows the same plots as the previous mentioned figures, but for $Sr = 0.038$. These plots show no build up of a LEV and its resultant suction peak. However, the propulsive efficiency of this k-h combination is higher than that of the earlier discussed $Sr = 0.344$ k-h combination ($\eta = 0.439$ against $\eta = 0.407$). This illustrates the important (but undesired) effect of the increased lift and thus

also power requirements generated by the LEV.

The increase in η for decreasing k for constant Sr, as was observed in Figure 6.3, can be explained by the time the airfoil spends in the thrust producing state. For the low k values, the airfoil spends more time during each period with a low suction peak near its nose than for the high k values. This is because it takes time for the suction peak to build up and at high k values, the suction peak (or vortex build up) is destroyed shortly after it has formed.

6.4 Effects of the trailing airfoil

As the sample cases in Table 6.3 show, the tandem setup outperforms the single airfoil setup in most cases. This is due to the ability of the trailing airfoil to extract energy from the wake of the leading airfoil. Thus, the trailing airfoil can produce a net thrust without any extra power requirements. This section discusses the effects the leading and trailing airfoil have on each other. Trailing edge vortex (TEV) shedding is also discussed.

Figures 6.17, 6.18 and 6.19 show time-histories of C_L, C_T and C_{Power}, respectively, for different Sr for both the leading airfoil in the tandem setup as well as a single airfoil. All figures show that the leading airfoil does not experience any significant changes in its performance as compared to a single oscillating airfoil. This demonstrates how information travels in the direction of the flow, the trailing airfoil will not significantly affect the leading airfoil, but only its wake.

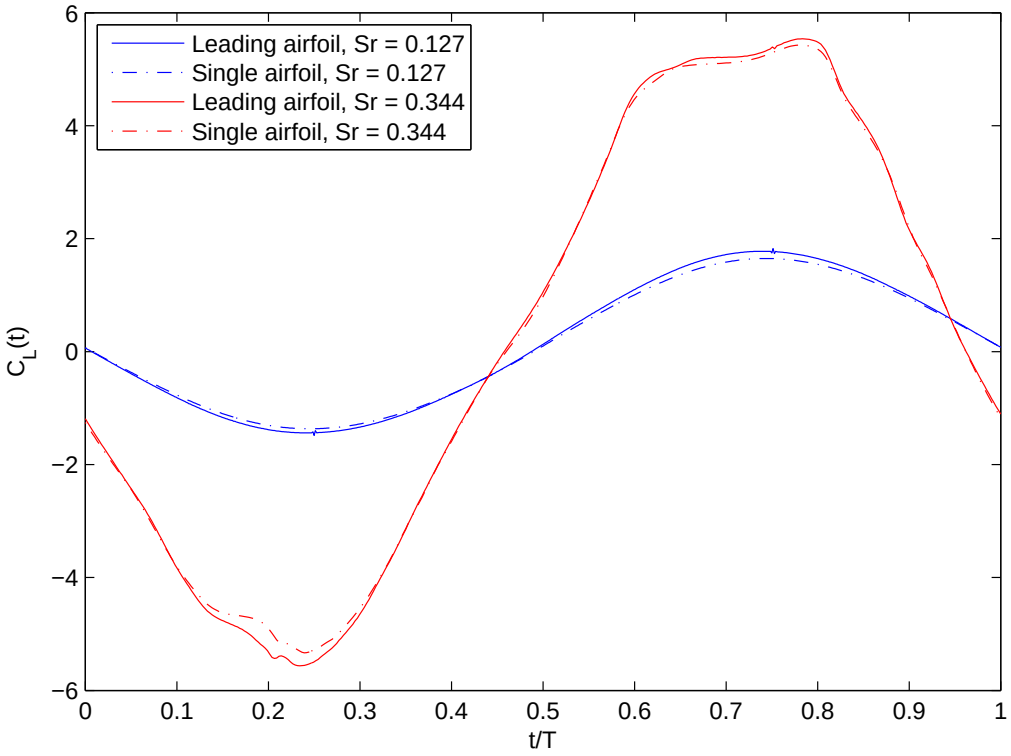

Figure 6.17: Time histories for lift coefficients. Data for the tenth period of simulation shown.

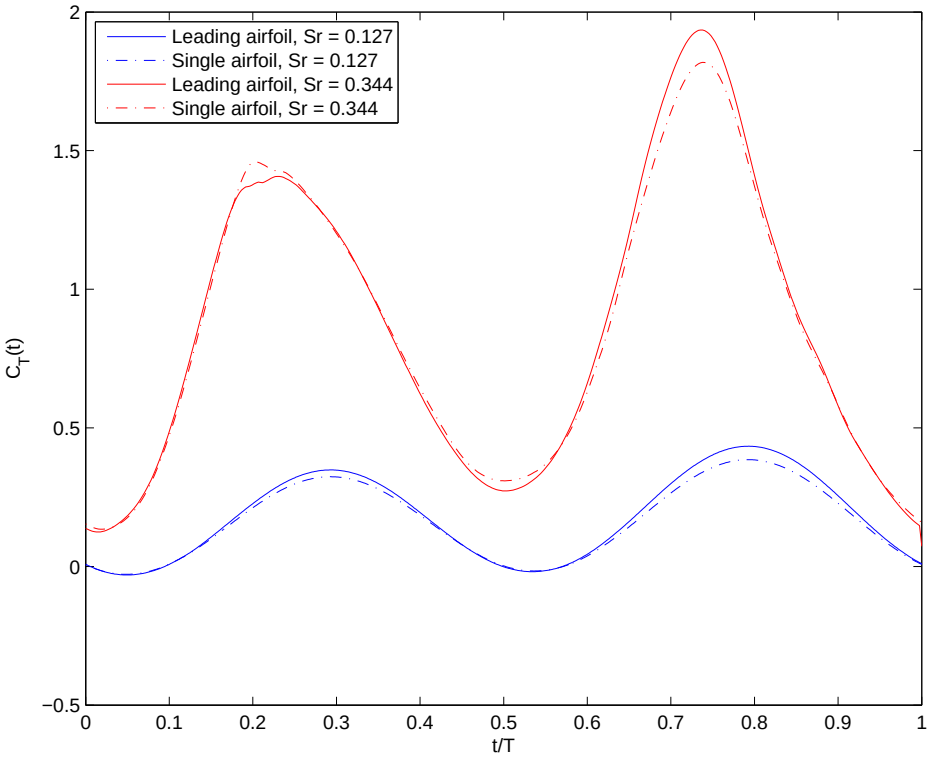

Figure 6.18: Time histories for thrust coefficients. Data for the tenth period of simulation shown.

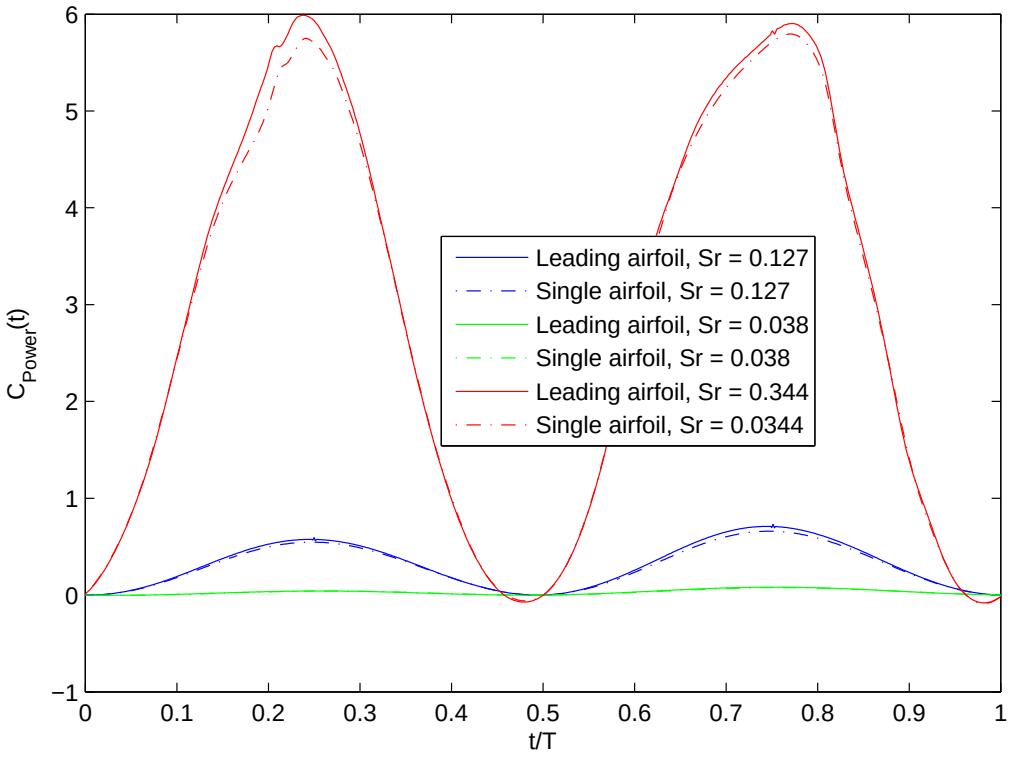

Figure 6.19: Time histories for power coefficients. Data for the tenth period of simulation shown.

The trailing airfoil experiences a change in apparent angle of attack (AoA) as a result of the leading airfoil oscillating and changing the direction of the flow in its wake. The resultant AoAs will be different from the ones the leading airfoil experiences; for several reasons. One reason is that when the leading airfoil reaches its highest plunge velocity, and thus also highest AoA, the fluid elements leaving the airfoil may be assumed to travel downstream with this same angle, but, for the same reason, they will not directly hit the trailing airfoil. A second reason is that the complex wake structures, most notably the TEVs, will interact with the flow that would otherwise reach the trailing airfoil uninterrupted. A third reason is viscous losses, which tends to "smooth" out the flow. In Figure 6.10 and 6.11, it is clear that the trailing airfoil experiences smaller changes in AoA, and thus also a lower apparent Strouhal number, than the leading airfoil since it reaches lower peaks in both C_T and C_L.

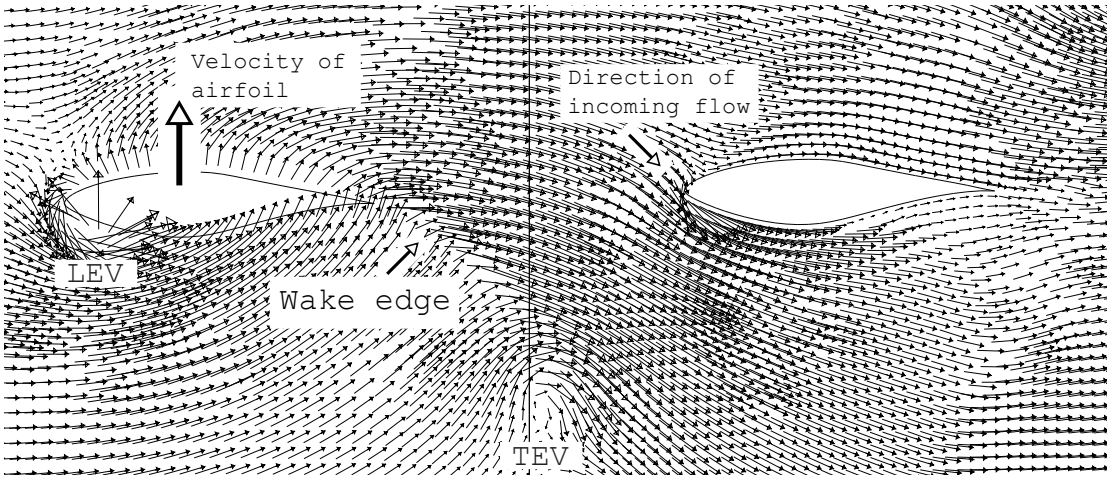

Figure 6.20: Velocity vectors for $Sr = 0.344$ with different elements marked. Vectors are sized and colored based on velocity magnitude: Upper limit $3U_0$ (red), lower limit $\frac{1}{8}U_0$ (dark blue).

In Figure 6.20, the direction of the flow the incoming flow from the trailing airfoil's point of view is marked, for the $Sr = 0.344$ case. The leading airfoil is in the middle of its upstroke (3/10 period) and the fluid elements that have reached the nose of the trailing airfoil left the leading airfoil during its previous downstroke. The "Wake edge" region, as marked in the figure, displays how the change in flow direction propagates downstream. This front will reach the trailing airfoil sometime during the following downstroke of the leading airfoil.

Tuncer and Platzer [4] attribute the thrust augmentation due to the trailing airfoil to the interaction between the trailing airfoil and the shed vortices from the leading airfoil. This is not the case, as it is the change in the flow direction caused by the leading airfoil that leads to this thrust augmentation. As may be seen in Figure 6.24, there are no vortices formed in front of the trailing airfoil for $Sr = 0.127$, but the setup still achieves a thrust augmentation due to the trailing airfoil, as apparent from Table 6.3.

The tandem setup will have a greater propulsive efficiency than the single airfoil only when the trailing airfoil experiences a net thrust. Since the trailing

airfoil experiences a lower apparent Sr than the leading airfoil, there is a threshold in Sr for when the trailing airfoil will achieve thrust production. That is, for all Sr values below this threshold, the trailing airfoil will experience a net drag, even though the leading airfoil (as well as the tandem setup in total) could experience a net thrust. This is evident in Table 6.3, where the single airfoil outperforms the tandem setup for $Sr = 0.038$, while the tandem setup achieves the highest η for $Sr = 0.127$ and $Sr = 0.344$. For $Sr = 0.344$, the increase is higher than for $Sr = 0.127$; indicating that the trailing airfoil has not reached its optimal apparent Sr (or k-h combination) at $Sr = 0.127$. However, since the performance of the leading airfoil is of most importance, $Sr = 0.127$, still achieves the highest η of the two cases.

As the leading airfoil performs an upstroke, it experiences a negative AoA, while the wake it generates will result in the trailing airfoil experiencing a positive AoA, as seen in Figure 6.20. There is also a delay in the change in the AoA that the trailing airfoil experiences as compared to the leading airfoil apparent AoA. Results of this may be seen in Figure 6.11. During the upstroke, the leading airfoil experiences negative lift, while the trailing airfoil will experience a delayed positive lift. The delay is dependent on the free stream velocity, as this determines the velocity of the wake. For $Sr = 0.344$, there is a delay of over half a period, in other words, the leading airfoil has finished more than half of its subsequent downstroke before the trailing airfoil notices the effects of the upstroke wake. For $Sr = 0.127$ (and a lower reduced frequency k), the delay is less than half a period. In this case the trailing airfoil experiences the wake effects of the upstroke even before the leading airfoil has finished the stroke.

6.4.1 Trailing edge vortex (TEV) shedding

If the Strouhal number is high enough, trailing edge vortex (TEV) shedding will occur. The case of $Sr = 0.344$ is used to investigate some of the effects that the TEVs have on both the wake in general as well as the trailing airfoil. As may be seen in Figure 6.21, the TEVs of the leading airfoil are formed so far away from the trailing airfoil that they do not directly interact with the trailing airfoil. However, the wake from the leading airfoil (as well as the TEVs themselves) causes vortices to be formed at or near the trailing airfoil. As the TEVs pass the trailing edge of the trailing airfoil, a complex vortex structure is formed, with at most six vortices existing simultaneously in the same "batch" of vortices (those formed as an effect of one upstroke or one downstroke of the leading airfoil). The six vortices interact with each other and at roughly four chord lengths downstream only three vortices remain, which all slowly diffuse as they continue their downstream movement.

In Figure 6.22, the effects on the trailing airfoil from the TEVs, seen in Figure 6.21, are visible. In the first frame, two suction peaks on the upper side of the airfoil are visible: One close to $x/C = 0.5$ and one near the tail of the airfoil ($x/C = 1$). The first peak is due to the leading airfoil TEV itself; this TEV has a very low pressure center, but as it is far away from the airfoil, it produces only a small effect. The last peak is due to the TEV formed at the tail, as a result of the TEV from the leading airfoil passing the trailing airfoil. This trailing airfoil TEV is created when the leading airfoil TEV "pulls" on the wake of the trailing

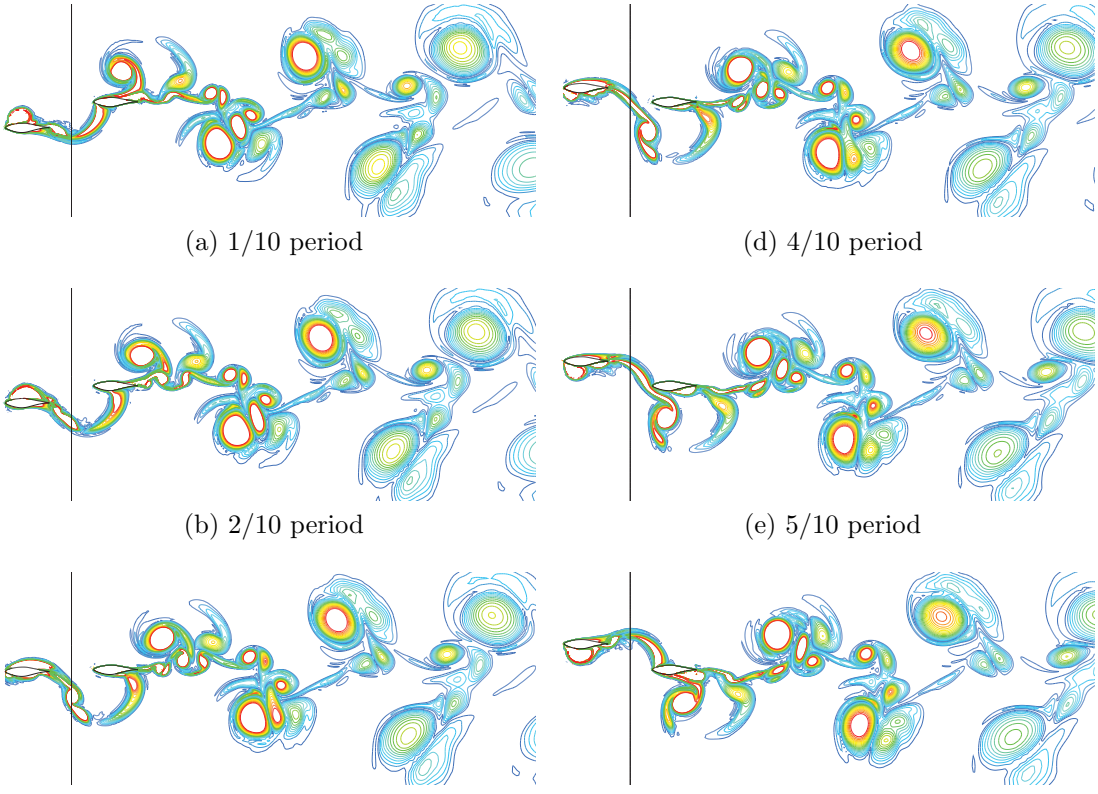

(a) 1/10 period (d) 4/10 period

(b) 2/10 period (e) 5/10 period

(c) 3/10 period (f) 6/10 period

Figure 6.21: Vorticity contour plots for an upstroke for the S809 airfoil. $k = 0.9$ and $h = 0.6$ ($Sr = 0.344$). Upper limit for vorticity set to 200 $^1/_s$ (colored red).

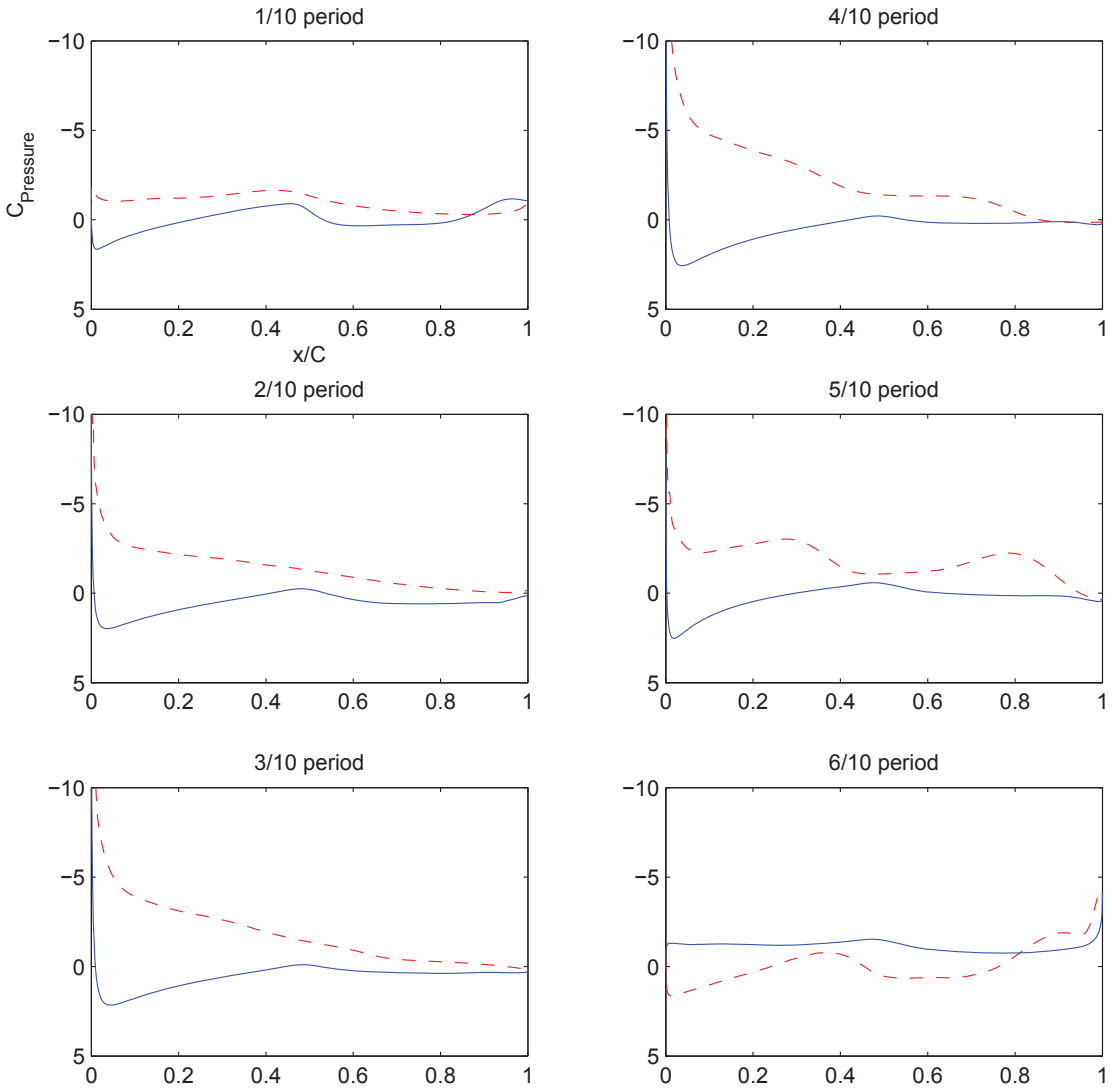

Figure 6.22: Plots of pressure coefficients for the leading airfoil. $k = 0.9$ and $h = 0.6$ ($Sr = 0.344$). Solid line: Upper side, dashed line: Lower side.

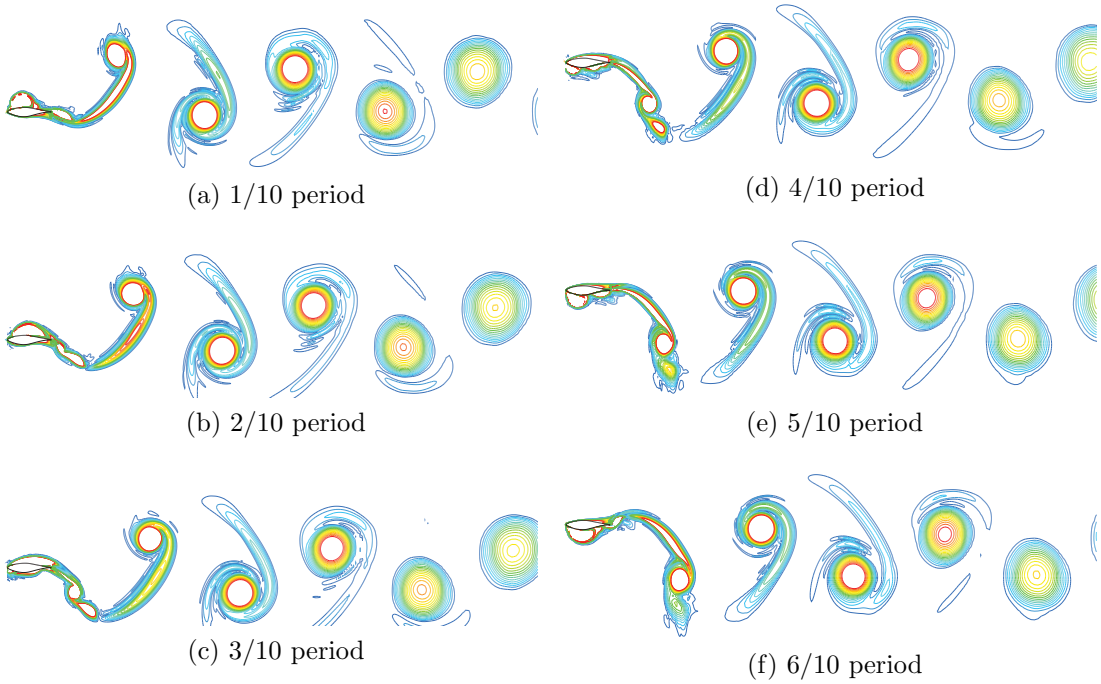

(a) 1/10 period (d) 4/10 period

(b) 2/10 period (e) 5/10 period

(c) 3/10 period (f) 6/10 period

Figure 6.23: Vorticity contour plots for an upstroke for the S809 airfoil. $k = 0.9$ and $h = 0.6$ ($Sr = 0.344$). Upper limit for vorticity set to 200 $^1/_s$ (colored red).

airfoil, as may be seen in Figure 6.21. Both these peaks are smoothed out in the fourth frame of Figure 6.22, where there are no vortices near the upper side of the airfoil.

For the lower side of the trailing airfoil, the two similar suction peaks may be seen in frames five and six. The pressure distributions in frames one and six are expected to be identical for a symmetrical airfoil, but as the S809 airfoil is not symmetrical, a stronger suction peak near $x/C = 1$ was created on the lower side than on the upper side. Because of this, the wake generated from the leading airfoil was not symmetrical for the upstroke and the downstroke.

The TEVs generated on the trailing airfoil are not desirable, as they generate suction that pulls the airfoil downstream and thus increases drag.

In the same figure, the results of the changing AoA, and thus also an apparent Strouhal number, may be seen. In the first frame the C_{Pressure} values are all centered around zero in a very rough, but still somewhat symmetrical way. In the following three frames, a suction peak near the nose of the airfoil ($x/C = 0$) may be seen to build up. This happens as the AoA increases. For higher and more abrupt changes in AoA (i.e. higher apparent Sr) it is expected that a LEV would form.

For comparison to the vortex shedding a single airfoil, Figure 6.23 shows vorticity contour plots for the same k and h parameters as the tandem setup previously discussed, but for a single airfoil. The first TEVs formed in the wake are formed approximately at the same positions for both setups. The effects on the vortex street from the trailing airfoil can be seen when comparing the two figures (Figure 6.23 and 6.21). The vortex street in Figure 6.23 is thrust indicative: the mushroom shapes are pointing downstream. The mushroom shapes are not

clearly visible in this figure, but the "tails" from each vortex can be seen having a downstream-fronting face.

Figures 6.24 through 6.27 show similar comparisons of vorticity contours for $Sr = 0.127$ and $Sr = 0.038$. For $Sr = 0.038$, there are small interactions between the wakes of the two airfoils. For $Sr = 0.127$, there are clearly visible effects from the trailing airfoil on the leading airfoil wake. Instead of a single LEV being formed during each stroke, up to four vortices are generated as a result of each up- or downstroke. The first vortex that forms, is formed about one chord length downstream of the trailing airfoil. As was shown previously for $Sr = 0.344$, the vortices need to be considerably closer than one chord length to have a noticeable effect on the airfoil pressure distributions. Although not shown here, the pressure distributions on the trailing airfoil did not show any suction peaks that could have been an effect of a vortex in close proximity to the airfoil.

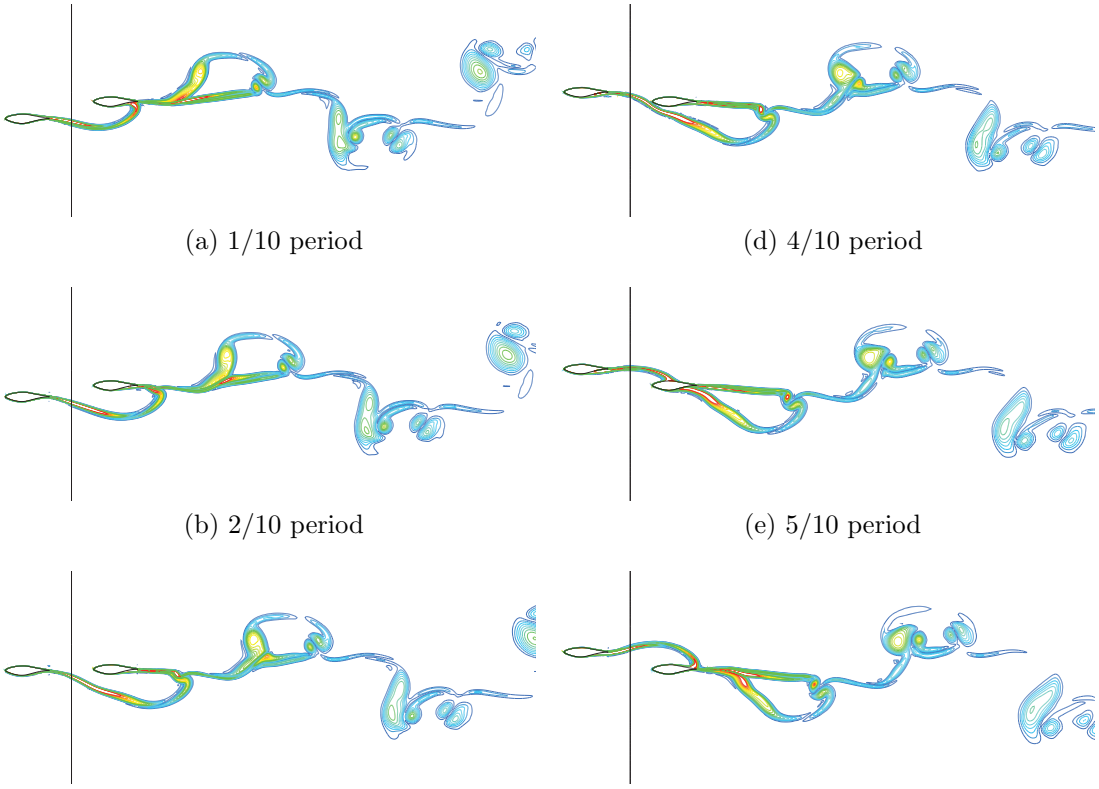

(a) 1/10 period (d) 4/10 period

(b) 2/10 period (e) 5/10 period

(c) 3/10 period (f) 6/10 period

Figure 6.24: Vorticity contour plots for an upstroke for the S809 airfoil for the tandem setup. $k = 0.5$ and $h = 0.4$ ($Sr = 0.127$). Upper limit for vorticity set to 200 $^1/_s$ (colored red).

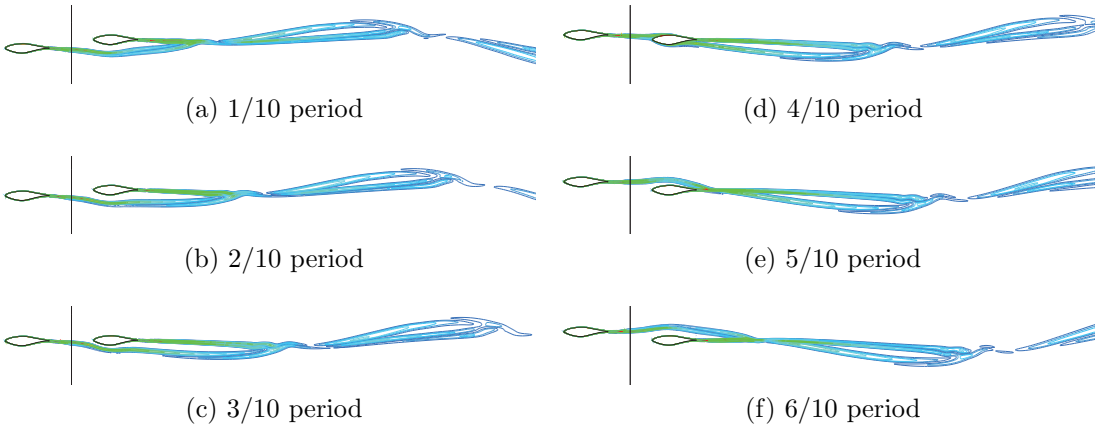

(a) 1/10 period (d) 4/10 period

(b) 2/10 period (e) 5/10 period

(c) 3/10 period (f) 6/10 period

Figure 6.25: C_{Pressure} contour plots for an upstroke for the S809 airfoil for the tandem setup. $k = 0.3$ and $h = 0.2$ ($Sr = 0.038$). Upper limit for vorticity set to 200 $^1/_s$ (colored red).

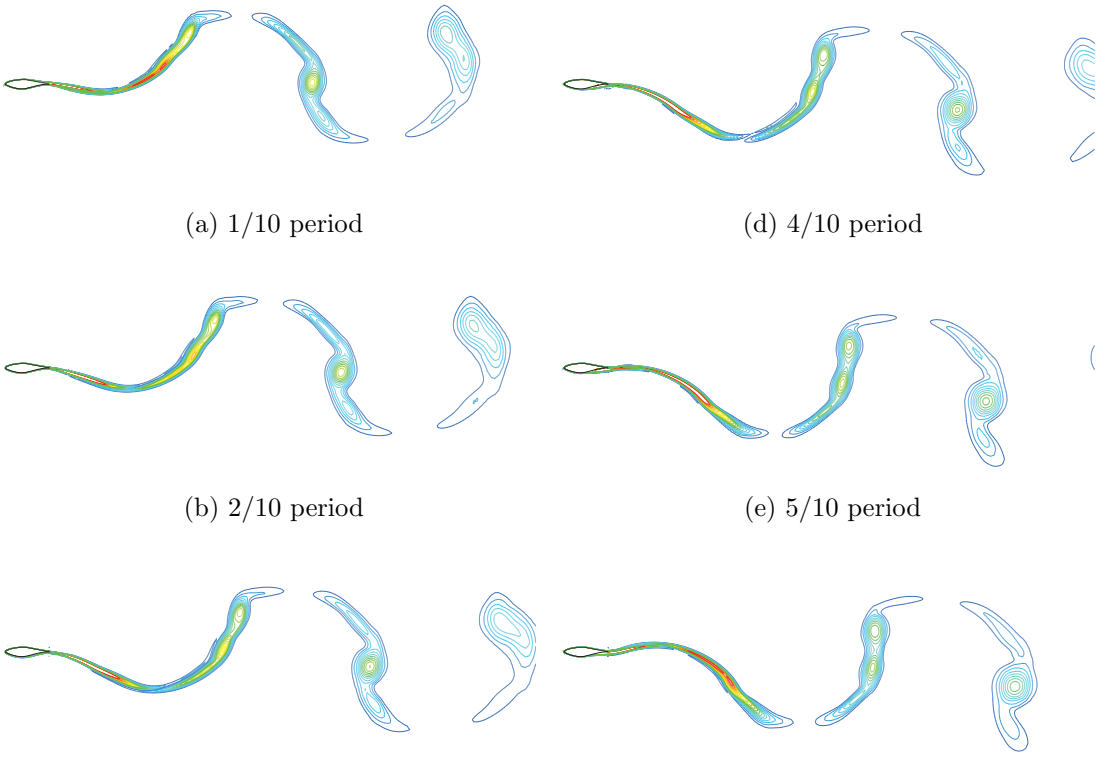

(a) 1/10 period

(d) 4/10 period

(b) 2/10 period

(e) 5/10 period

(c) 3/10 period

(f) 6/10 period

Figure 6.26: C_{Pressure} contour plots for an upstroke for the S809 airfoil for the single airfoil setup. $k = 0.5$ and $h = 0.4$ ($Sr = 0.127$). Upper limit for vorticity set to 200 $^1/_s$ (colored red).

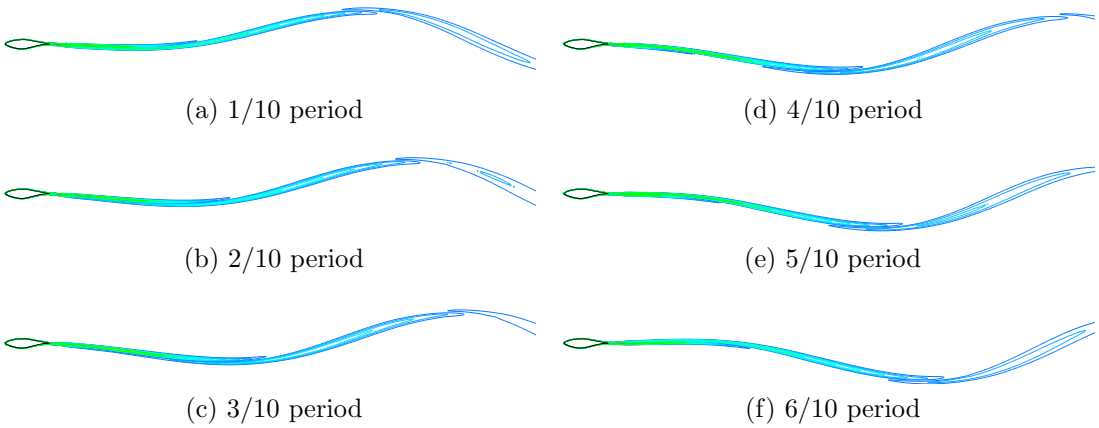

(a) 1/10 period

(d) 4/10 period

(b) 2/10 period

(e) 5/10 period

(c) 3/10 period

(f) 6/10 period

Figure 6.27: C_{Pressure} contour plots for an upstroke for the S809 airfoil for the single airfoil setup. $k = 0.3$ and $h = 0.2$ ($Sr = 0.038$). Upper limit for vorticity set to 200 $^1/_s$ (colored red).

Chapter 7

Model uncertainties

Earlier chapters (3 - Numerical methods, 4 - Grid generation and 5 - Model validation and verification) have discussed some aspects of the limitations of the model setup as well as potential sources for inaccuracy/uncertainty. This chapter discusses the observed effects of these uncertainties based on the post-processing of the results presented in the previous chapter (6 - Results and discussion). Several aspects resulting in uncertainties, which have not been mentioned earlier, are also discussed in this chapter.

7.1 Numerical considerations

The numerical setup was not stable for all the cases investigated in this study. For some of the oscillation modes (different k and h), the solution would diverge, while most modes gave converging solutions. As mentioned in Results and Discussion section 6.2, the solution for the NACA 0012 profile diverged for all $h = 0.5$ and some of the $h = 0.3$ cases. Since the NACA 0012 profile provided stable solutions for $h = 0.6$ for the same k values as simulated for $h = 0.5$, the divergence cannot be explained by the high plunge velocities reached by the airfoil. It is assumed that the divergence was related to the low quality cells near the trailing edge of the airfoil (see Section 7.2.1). A thorough investigation was not performed as the setup produced stable solutions for most cases.

7.1.1 Reduced URFs

As stated in the Model validation and verification chapter (Section 5.1.2), the number of iterations per time-step was thought to be low, due to limitations in computational time. Since many of the cases investigated were unstable, the reduced URFs (see Table 3.2) were used for many of the cases. This is believed to be a source of inaccuracy. Since the number of iterations per time-step was kept constant, the solution would advance less each time-step when the URFs were decreased, and it would reach higher residual values than the default URFs.

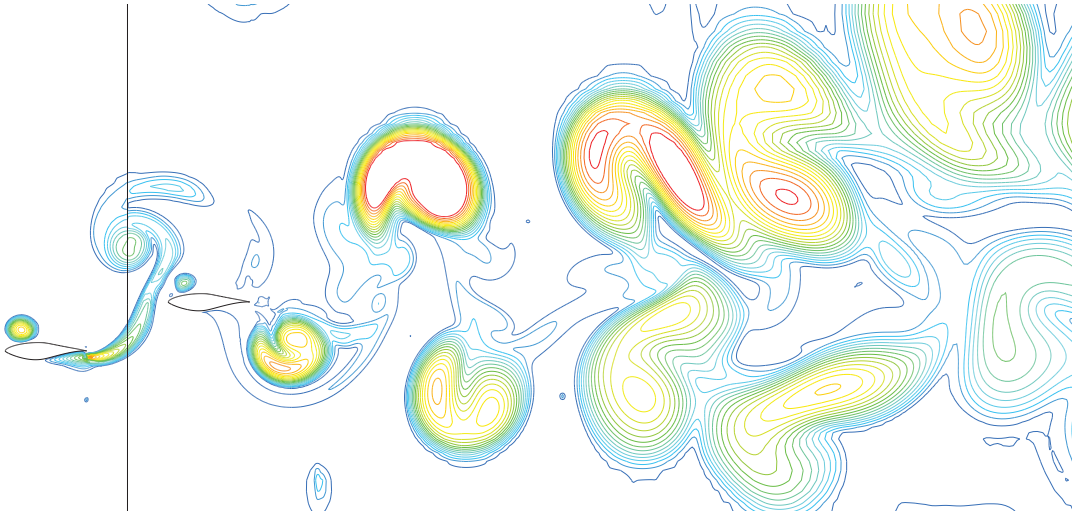

Figure 7.1: Turbulent viscocity ratio contour plot for $Sr = 0.573$. Upper limit set to $1 \cdot 10^5$ (colored red).

7.1.2 Turbulent viscocity ratio limit

The upper turbulent viscocity ratio limit set by default to 10,000 in Fluent was reached for the cases with Sr values of 0.477, 0.497 and 0.573 for both airfoils. These were the three highest Sr values investigated in this study. As seen in Figure 7.1, this limit was reached inside the TEVs. The number of cells for which the limit was reached behaved in a periodic manner for each of the cases, with peaks ranging from several hundred cells to a few thousand cells. Since the number of cells affected did not diverge and the affected cells were not near either of the airfoils, this was not believed to affect the airfoil performance significantly.

7.1.3 Boundary conditions

The boundary conditions for turbulence at the inlet was set to a turbulent intensity (TI) of 1% and a turbulent length scale of 1 m. For the three cases that were chosen for in depth investigations, the maximum TI levels were found to be 8%, 15% and 88% for Sr values of 0.038, 0.127 and 0.344 respectively. These levels appeared where the velocity magnitude also had its peak values.

Different TI levels for the boundary conditions were not investigated, and it is uncertain how a different level would affect the overall solution. However, it is expected that any effect would be smaller for higher Sr values, since the difference between TI values found in the areas of interest and the inlet TI values increased as Sr increased. Real world TI values might be lower for a modern wind tunnel and higher for typical outdoor conditions (up to the order of 10%).

Nothing in the results clearly indicated that the turbulent length scale of 1 m was unrealistic. No investigations of different turbulent length scales were performed.

7.1.4 Turbulence models

No clear effects due to the choice of turbulence model were observed. The other k-ω based models Fluent offers are believed to provide similar results, while the k-ϵ based models could give more substantial different results since they use a different near-wall treatment.

Direct numerical simulations (DNS) and the large eddy simulation (LES) turbulence model, which both give more accurate descriptions of the turbulence than the RANS models, were not investigated due to time constraints and high computational demands.

Figure 7.2 shows examples of how different turbulence models can produce significantly different results.

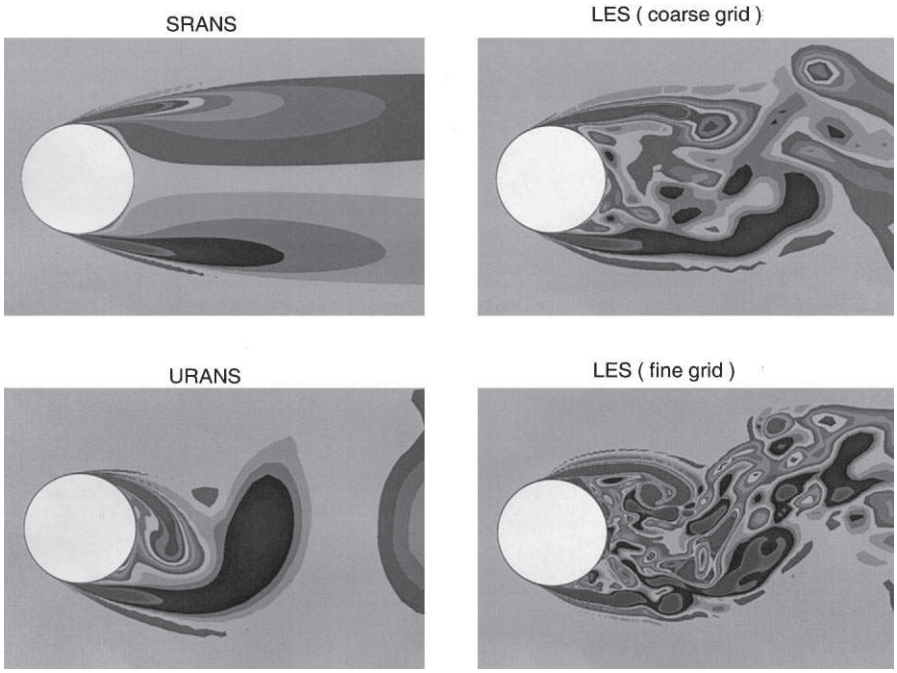

Figure 7.2: Wake patterns behind a circular cylinder for different turbulence models. SRANS stands for steady RANS, which in this text is referred to as simply as RANS. From [44].

7.1.5 Flow-time simulated

All cases were simulated for 10 periods of the oscillation motion. As seen in Figure 7.3, the thrust coefficient shows a periodic trend after only a few periods of simulation. Figure 7.4 shows only the peak values for the leading airfoil during the downstrokes for the three different Sr values. As may be seen, the peak values stabilizes faster for the lower Sr values. After 10 periods, all peak C_T values have stabilized. This indicates that it was sufficient to simulate 10 periods of oscillation motion for the overall solution to stabilize.

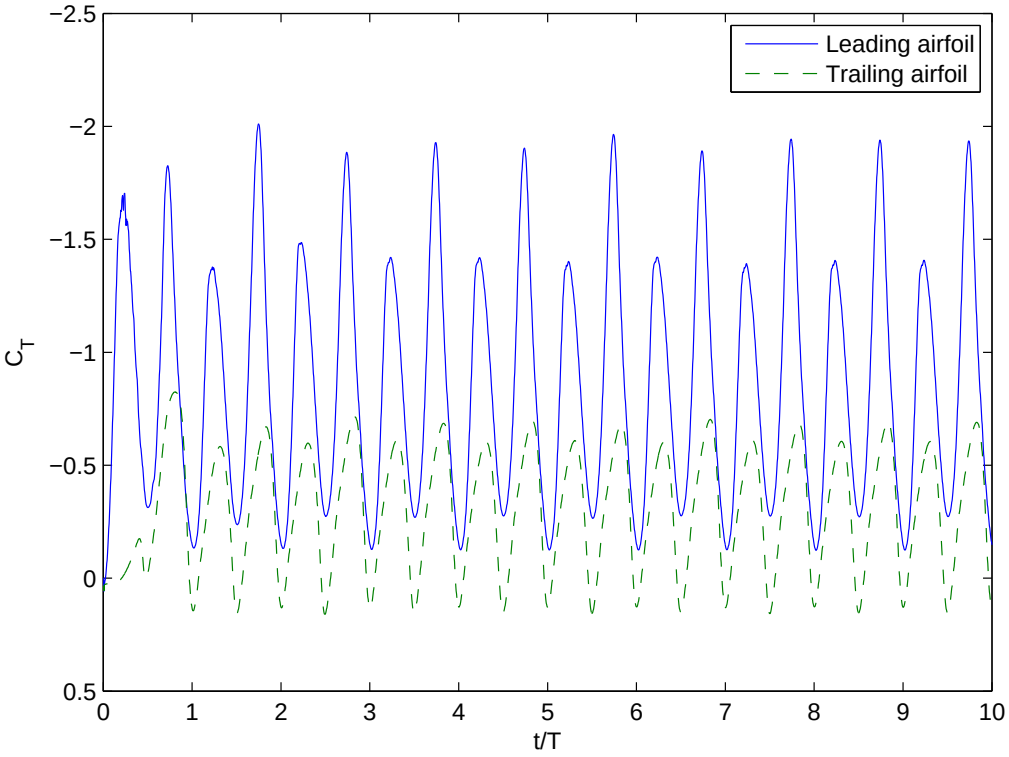

Figure 7.3: Time-histories of thrust coefficients for $Sr = 0.344$.

7.1.6 3D effects

Real-life flow is in three dimensions, and thus two dimensional simulations may not necessarily provide a realistic description of the flow. The main 3D effects of a wing in flapping motion (e.g. a bird's wing during flying) are related to the finite-span edge effects of the wing. Figure 7.5 shows the complexity of 3D flow.

For this study, 2D simulations were performed partly because of the high computational demand for 3D simulations and because there are still many aspects conserning flapping wing aerodynamics that are not fully described; which can be investigated through 2D simulations. It is not clear how 3D simulations of finite-span wings for similar case setups as those investigated in this study would compare to 2D simulations.

7.2 Grid dependency

An optimal grid produces grid independent results. That is, the flow physics are not dependent on the grid quality. However, several flow feautres, as well as the numerical accuracy, are dependent on the grid in this study. Different aspects of the weaknesses of grids used in this study are discussed in this section, starting the discussion with the near-airfoil regions and then expanding throughout the domain.

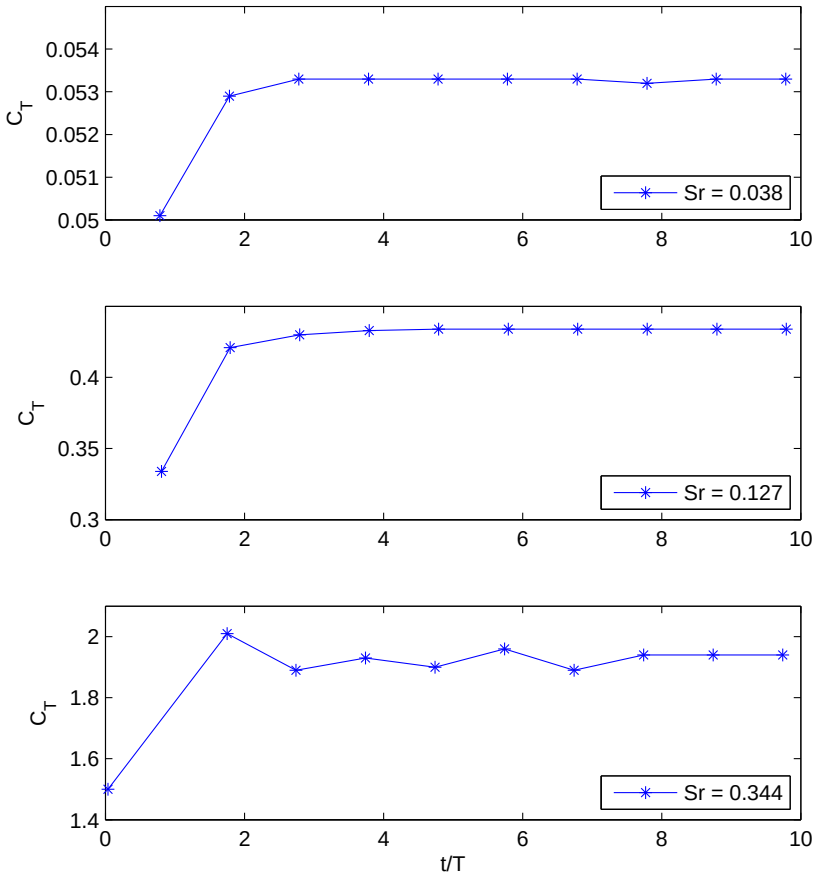

Figure 7.4: Peak values for thrust coefficients for leading airfoil for different Sr values. Only peaks during downstrokes plotted.

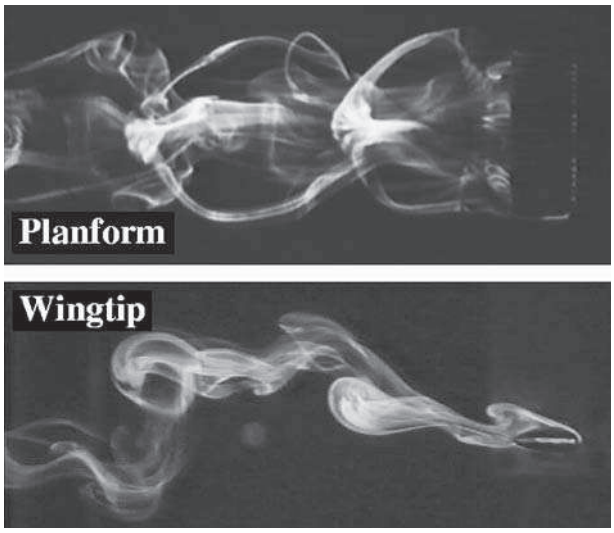

Figure 7.5: Dye flow visualization of the flow behind a 3D flapping airfoil. From Parker et al. [16].

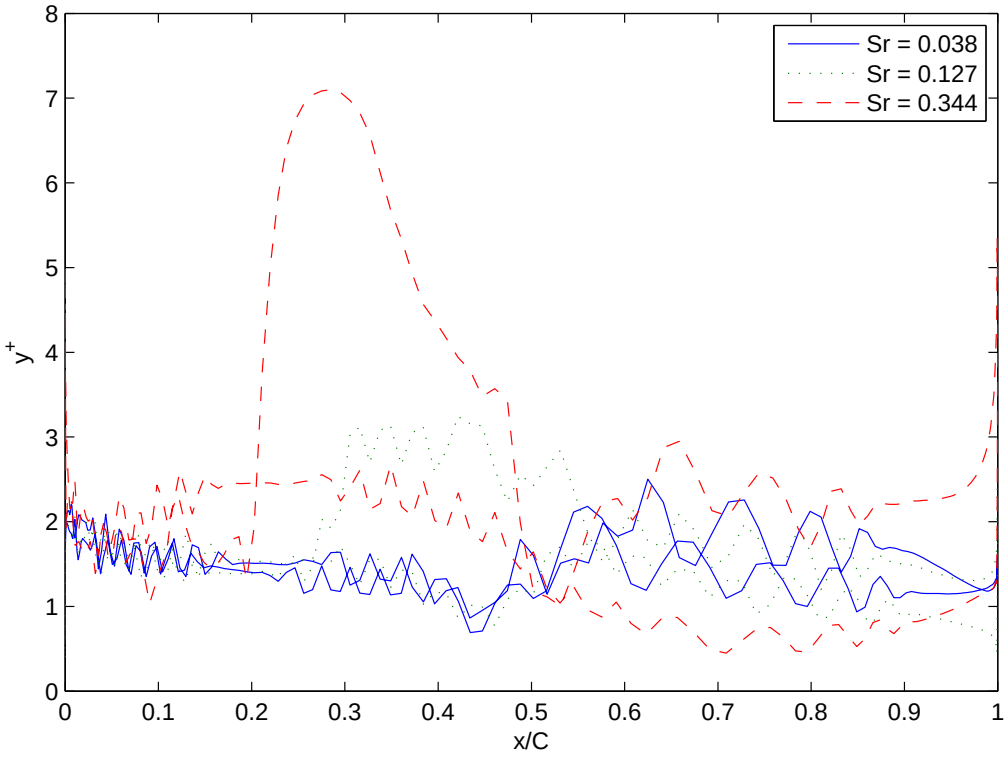

Figure 7.6: y^+ values for the leading airfoil for different Strouhal numbers.

Table 7.1: Average y^+ values for the leading airfoil for different Strouhal numbers.

Sr	Average y^+
0.038	1.50
0.127	1.52
0.344	2.31

7.2.1 Grid quality near the airfoil

The y^+ values for the first layer of cells should, for the k-ω based Tranition SST turbulence model, be as low as possible. For practical reasons, mostly computational demand, average y^+ values of around 1 are recommended [13]. In Table 7.1, it may be seen that none of the cases controlled had the recommended average y^+ values. The high average achieved for $Sr = 0.344$ is explained by the peak in y^+ seen in Figure 7.6, which is due to a vortex near the wall.

Although the enhanced wall treatment of the ω based turbulence models is designed to handle y^+ values within the buffer layer ($5 < y^+ < 10$), the high y^+ values are a source of inaccuracy. This is especially true since the highest values occurs where there is a LEV present, which was showed to have large effects on the airfoil performance. However, it is not believed that lower y^+ values would produce fundamentally different results.

Apart from the y^+ values of the first layer of cells near a wall, the number of cells that make up the boundary layer is also important to get a valid description of the boundary layer. Figure 7.7 shows samples of velocity vectors for two near-wall areas for the upper side of the leading airfoil for the $Sr = 0.344$ case. In the

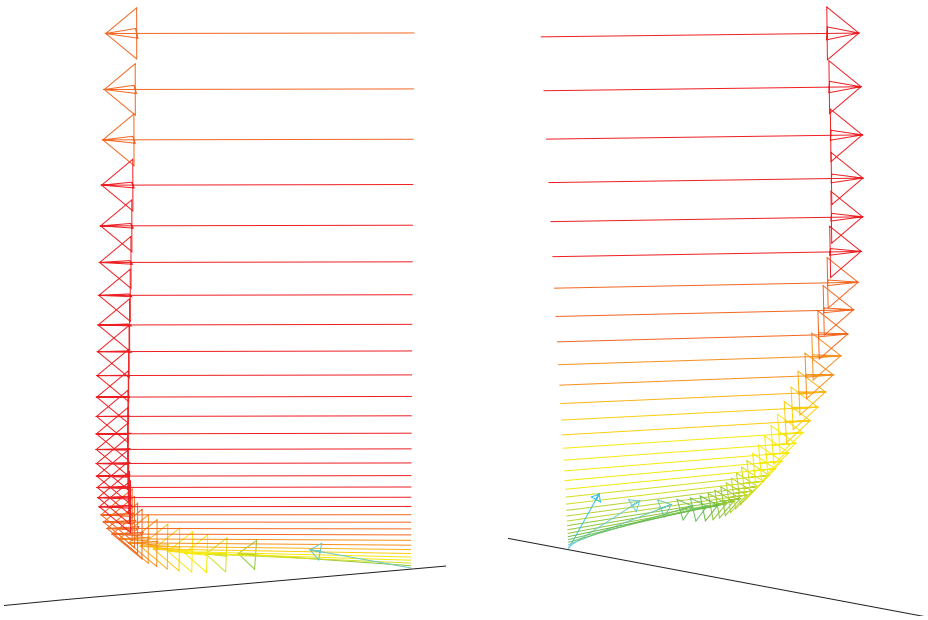

(a) At $0.33x/C$, with a LEV present. Colors: 0 m/s - dark blue and $3U_0$ - red.

(b) At $0.75x/C$, colors: 0 m/s - dark blue and $1.3U_0$ - red.

Figure 7.7: Velocity vectors at the upper side wall of the leading airfoil during start of upstroke for $Sr = 0.344$. One vector for each cell, colored by velocity magnitude.

first frame about 15 cells make up the boundary layer[1], while in the second frame about 29 cells make up the boundary layer.

By Fluent [13], it is recommended to have at least 10, preferably 20 cells in the boundary layer. Both samples investigated met this criterion. There was large differences in the number of cells making up the boundary layer for the different cases and flow times, and it was unfeasable to investigate every single case. However, the LEV produced at $Sr = 0.344$ was believed to produce some of the smallest boundary layers, and was thus concidered represantative for the lower limit of cells found throughout this study.

It may also be noted that the boundary layer in the first frame resembles a turbulent boundary layer (high velocity gradients, velocoties reach U_0 quickly), while the boundary layer in the second frame resembles a laminar boundary layer (lower velocity gradients, velocoties reach U_0 more slowly).

Near the trailing edge of the airfoil, the grid was not of optimal quality. This area of the grid may be seen in Figure 7.8. There are large differences in the size of the cells to the left and right of the vertical line running through the trailing edge (tail) of the airfoil. At the trailing edge itself, all 100 grid edges from the grid boundary layer semi-circle terminates in one point. This causes cells of high skewness.

Some effects of this are shown in Figure 7.10 and 7.9. The first figure shows vorticity contour plots for the area near the trailing edge. In the first frame, some unnatural jumps in vorticity can be seen along a vertical line that runs through

[1]The cells were counted by visual inspection, and the upper limit of the boundary layer was set to were two consecutive velocity vectors had the same length.

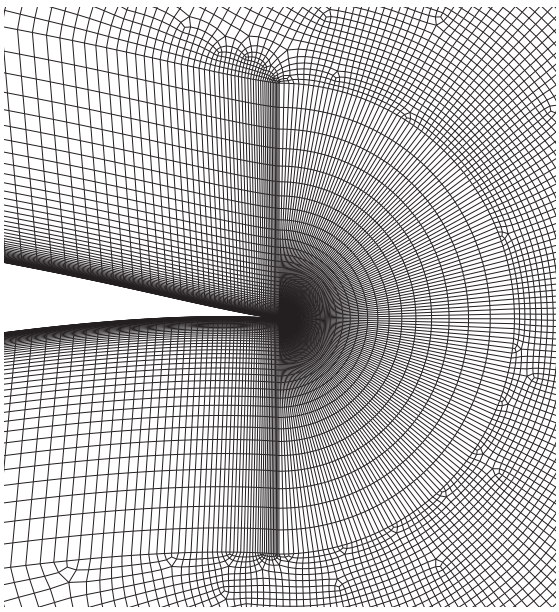

Figure 7.8: View of grid near trailing edge of S809 airfoil.

the trailing edge. These artifacts may also be seen in the second frame, which shows a close up of the trailing edge. It is unclear how much this affected the overall solution.

Figure 7.10 shows contour plots of Courant numbers, defined in one dimension as

$$\text{Courant} = \frac{u\Delta t}{\Delta x}, \tag{7.1}$$

where u is the fluids velocity, Δt is the time-step and Δx is the size of the cell. The Courant number is a measure of how many cell-lengths a fluid element will travel during each time-step, and its value should be close to one. As seen in the first frame of Figure 7.10, a large number of cells have Courant numbers above 20, and in the second frame Courant numbers are seen to exceed $1,000$. The highest Courant number for the entire domain was $26,508$, for the cells right next to the trailing edge. These high Courant number regions are belived to decrease the accuracy of the solution, particularly in these regions.

7.2.2 Grid quality throughout the domain

The small disk shaped areas in the first frame of Figure 7.10 with elevated Courant numbers as compared to the surrounding area, are found throught the unstructured region of the grid. The first frame of Figure 7.11 shows a close-up of these artifacts superimposed on a view of the grid. As seen in the figure, the elevated Courant numbers occur where the cell skewness is increased as compared to the surrounding cells. These areas occur as a result of the unstructured grid technique. The second frame shows a contour plot of vorticity for the same area, an unnatural increase in vorticity is seen close to one of the regions with elevated Courant numbers.

Figure 7.12 shows the artifacts occurring throughout the unstructured region, while there are no such artifacts in the structured region. It should be noted that

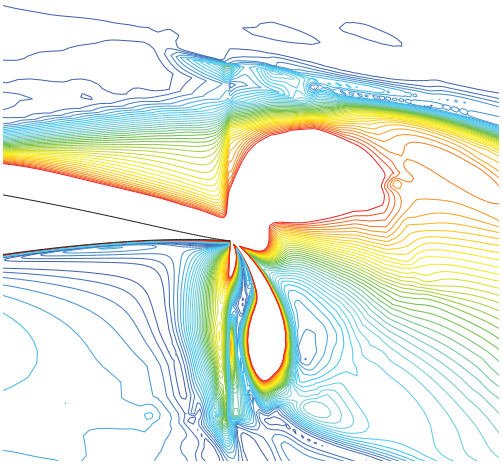

(a) Limits: 0 (dark blue) and 800 $^1/_s$ (red).

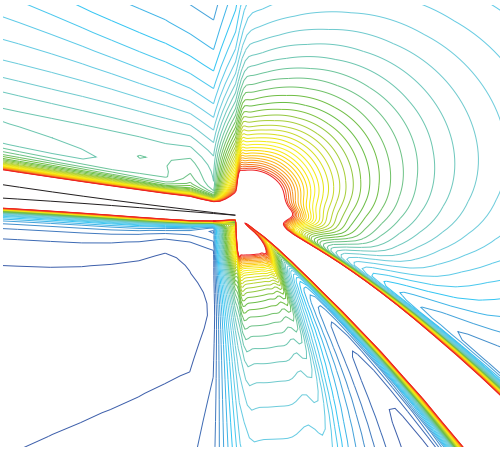

(b) Close-up of trailing edge. Limits: 0 (dark blue) and 10,000 $^1/_s$ (red).

Figure 7.9: Vorticity contour plots for the trailing edge of the leading airfoil during start of upstroke for $Sr = 0.344$.

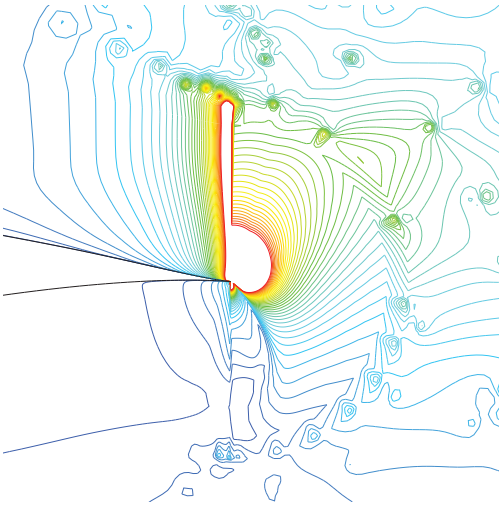

(a) Limits: 0 (dark blue) and 20 (red).

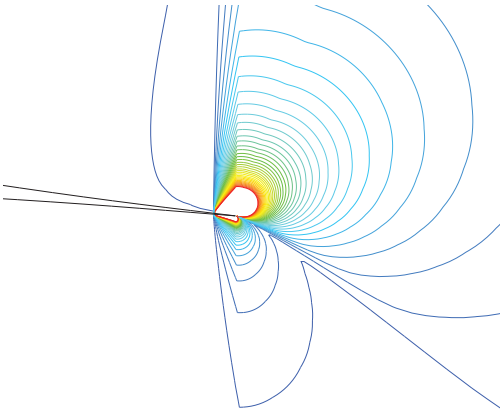

(b) Close-up of trailing edge. Limits: 0 (dark blue) and 1,000 (red).

Figure 7.10: Courant number contour plots for the trailing edge of the leading airfoil during start of upstroke for $Sr = 0.344$.

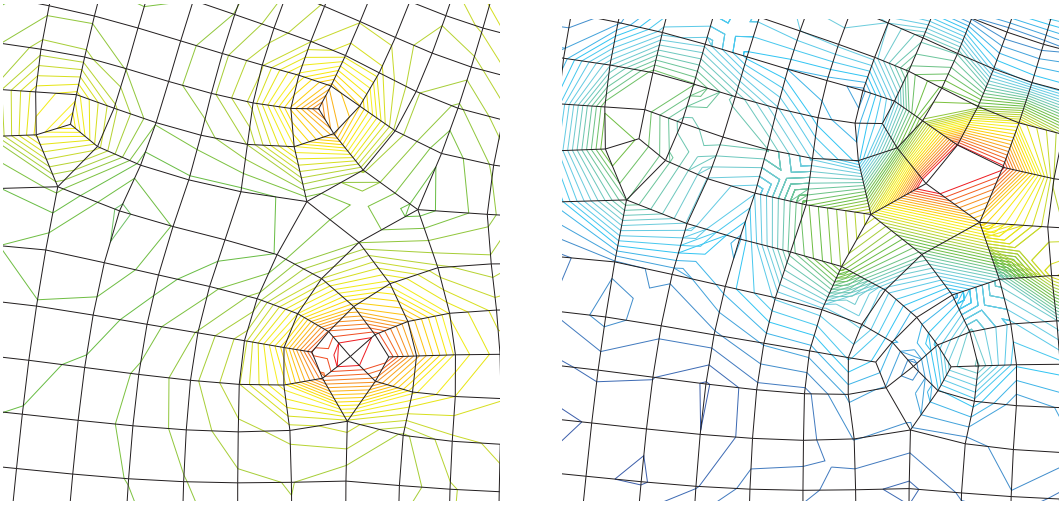

(a) Courant number, upper limit set to 1 (colored red).

(b) Vorticity, upper limit set to 1.2 $^1/_s$ (colored red).

Figure 7.11: Contour plots in unstructured region of the grid with grid showing.

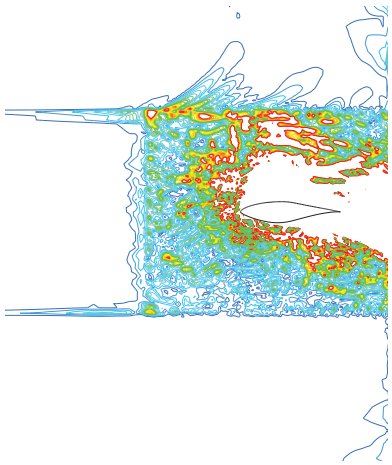

Figure 7.12: Contour plot of vorticity for area surrounding the unstrucuret region surrounding the leading airfoil. Upper limit of vorticity set to 1 $^1/_s$ (colored red)

unevennesses are a few orders of magnitude smaller than the vorticity scales that are found in the LEVs and TEVs. The LEV for $Sr = 0.344$ reaches a vorticity of around $1,500$ $^1/_s$ in its center, while the TEV reaches around 700 $^1/_s$. These artifacts are believed to decrease the accuracy of the solutions, but not affect the general physics of the flow.

As discussed in the section Grid independence study 5.1.1, the grid resolution is crucial for resolving the wake structures properly. For the highest amplitudes investigated in this study ($h = 0.4$, 0.5 and 0.6), the trailing edge vortices extended into the region of decreased grid resolution. As shown in Figure 7.13, this did not lead to any unnatural effects in the vortices. However, it is believed that the vortices diffused quicker because of this. It should be noted that the wake structures did not have a significant effect on the airfoils performance, as was shown in Section 6.4; where performance of the leading airfoil was shown to be very close to that of the single airfoil, even though the two cases had very different

wake structures. This leads to the conclusion that the possible numerical diffusion of the vortices several chord lengths away from the airfoils did not lead to any significant impacts on the airfoils performance.

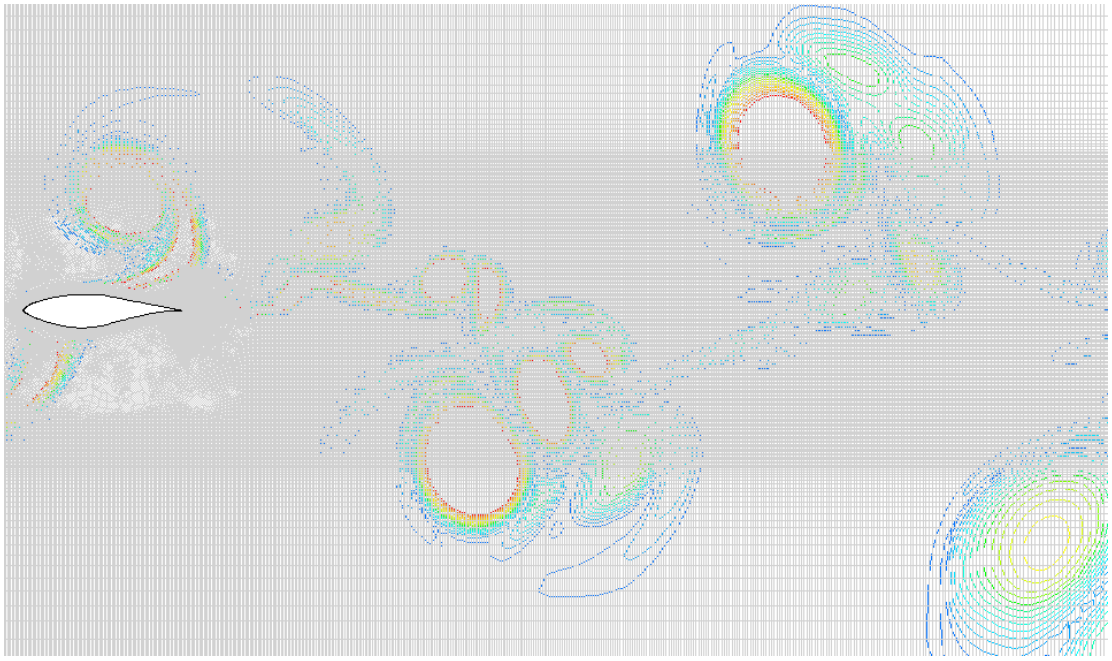

Figure 7.13: Vorticity contour plot for $Sr = 0.344$ with grid showing. Upper limit for vorticity set to 200 $^1/_s$ (colored red). Note: Tandem setup with only trailing airfoil showing.

The size of the overall domain, which extends $12.5C$ upstream, above and below the leading airfoil and $20C$ downstream of the leading airfoil, was considered sufficiently large, based on the same arguments given above.

7.2.3 Sliding grid technique

The sliding grid technique did not seem to be a source of significant error in the solutions. As may be seen in figures presented earlier of different contour plots, there were no observable artifacts near the sliding grid boundary for any of the cases.

Chapter 8

Conclusions

8.1 Concluding remarks

Results on parameter dependency from this study agrees with those in the recent literature covering flapping airfoils (c.f. Ref [18]). That is, there is a dependency on the Strouhal number Sr, but it does not fully describe the flow, and the k-h combination of a given Strouhal number is also of importance. This was found to be true for both single and tandem airoil setups.

One reason for this is related to leading edge vortex (LEV) shedding. The downstream velocities of LEVs are determined by the free-stream velocity, and not Sr. Thus, for a constant Sr value the lower the k value is, the further downstream the LEV will travel, which results in fundamentally different flow conditions for equal Sr values.

The suction peaks near the front of the airfol were found to be the single most important source of thrust generation. These suction peaks resulted sometimes in LEV shedding.

The investigation of the LEV shedding offered explanations to the differences between the propulsive efficiensies for the low, optimum and high Sr values. For low Sr values, no LEVs were formed (or starting to be formed) due to the low effective AoA achieved for low plunge velocities, and low or even negative thrust is achieved. For Sr values giving optimum η values, there was a build up of a low pressure region by the nose of the airfoil during each stroke, but no LEVs were fully formed. This lead to pressure forces consisting of a large part of upstream horizontal forces (thrust) and smaller parts of undesired vertical forces (lift). For high Sr values, LEVs were formed and traveled downstream along the airfoil, thus increasing the lift and power demand C_{Power} significantly. There was also a rise in C_T, since the magnitude of the LEV increased. However, the rise in C_{Power} was greater than the rise in C_T for these high Sr values, and thus η decreased.

The trailing airfoil was not found to affect the performance of the leading airfoil with any significance; the leading airfoil performed similar to a single airfoil for the same conditions. Thus, the tandem setup was assumed to outperform the single airfoil setup as long as the trailing airfoil generated a net thrust. This was found true for the three cases investigated in detail.

The trailing airfoil experienced an apparent oscillating motion, since the wake of the leading airfoil changed the apparent angle of attack for the trailing airfoil

periodically. Thus it was able to extract energy from the wake, and turn it into a net thrust.

The trailing edge vortex (TEV) shedding from the leading airfoil was found to affect the trailing airfoils if they were formed in front of the trailing airfoil. However, the effects of the apparent Sr value was found to have a higher effect on the trailng airfoil's performance, since this generated higher suction peaks than the passing TEVs. It should be noted that this conclusion was based on the case of $Sr = 0.344$ with $h = 0.6$, and if setups with a lower h value were to produce TEVs closer (in the vertical direction) to the trailing airfoil, their effects on the airfoil would be greater.

For the cases with the highest η values, the TEVs were found to be generated past the trailing airfoil. This could indicate that TEVs generated before the trailing airfoil had negative effects on it, but since this was not investigated in detail no conclusions could be made.

For all but the lowest Sr values investigated, the wakes for the tandem setups were significantly different than those for the single airfoil setups. For $Sr = 0.344$, for instance, the single airfoil produced a pure reverse von Kármán vortex street, while the tandem setup produced a complex wake pattern with six times as many vortices generated in the wake. However, it is important to note that the wake was not found to significantly affect the performance of the airfoils, which emphazises that the wake is an effect, and not a cause, of the airfoils motion/performance. Some papers (e.g. Ref. [18, 11]) states that the wakes are thrust or drag *producing*, while this study indicates that the wakes are rather thrust or drag *indicating*, as Jones et al. [1] states.

8.2 Future studies

This section lists possibilities for future studies based on this study and its results.

- **Investigating different X_{shift} values.** Tuncer and Plazter [4] found small variations in η for X_{shift} values ranging from 0.65 to 3.0. It is expected that much higher or much lower lower X_{shift} values would give significantly different results.

- **More comparisons between single and tandem setups.** In this study, only three cases for the tandem setup were simulated for both the single and the tandem setups. More simulations for the single airfoil setup could provide more insight in the effects of the trailing airfoil.

- **Investigating the wake velocity profiles.** Previous studies (c.f. [1]) have found that an increase in mean velocities in the wake indicate thrust production by the oscillating airfoil. This investigation has to the authors knowledge not been performed for a tandem airfoil setup.

- **Investigating higher h values than** 0.6**.** This study only investigated h values up to 0.6, and the peak propulsive efficiency was believed to be found at a higher h value. However, it should be noted that for real life systems (e.g. birds or micro air vehicles), very high h values are not feasible.

Appendix A

High performance computing

The simulations in this study were performed on the high performance Linux cluster Kongull. This was due to the high computational demands for the cases investigated. A large number of grid cells, moving grids and transient simulations were three important reasons for this high demand.

The following is extracted from the Kongull support site:

> The Kongull cluster is a CentOS 5.3 Linux cluster running Rocks on HP servers with AMD processors. The cluster has 98x 12-way nodes, with 1 login, 4 I/O and 93 compute nodes. Each node is equipped with 2x 6-core 2.4 GHz AMD Opteron 2431 (Istanbul) processors, with 6x 512KiB L1 cache and a common 6 MiB L3-cache.

The nodes that were used in this study had 24 GiB/node of memory. For each simulation, 12 cores of 2.4 GHz were used.

Table A.1: Run times (wall-clock) for a sample case.

	Run time
PC	570 min
Kongull	103 min

Table A.1 shows run times for the same simulation, performed at both at Kongull and at a desktop PC with an Intel Core 2 Duo CPU, 3.33 GHz and 4,00 GB RAM. The PC took 5.5 times as long to complete the simulation. The PC had a faster CPU and less memory than the Kongull cores, so the speed-up is not directly comparable, but it gives an indication of the actual speed-up.

The Kongull cluster offered the opportunity to run several simulations in parallel, effectively increasing the speed-up even more.

In order for the 12 CPUs to work on the same grid simultaneously, the grid needed to be divided into 12 partitions. The "Cartesian X-Coordinate" partitioning scheme from Fluent was applied; the result may be seen in Figure A.1. This scheme was chosen because it was necessary for the sliding grid technique to have only one CPU assigned to work with the grid interface. There are approximately the same number of cells in each partition.

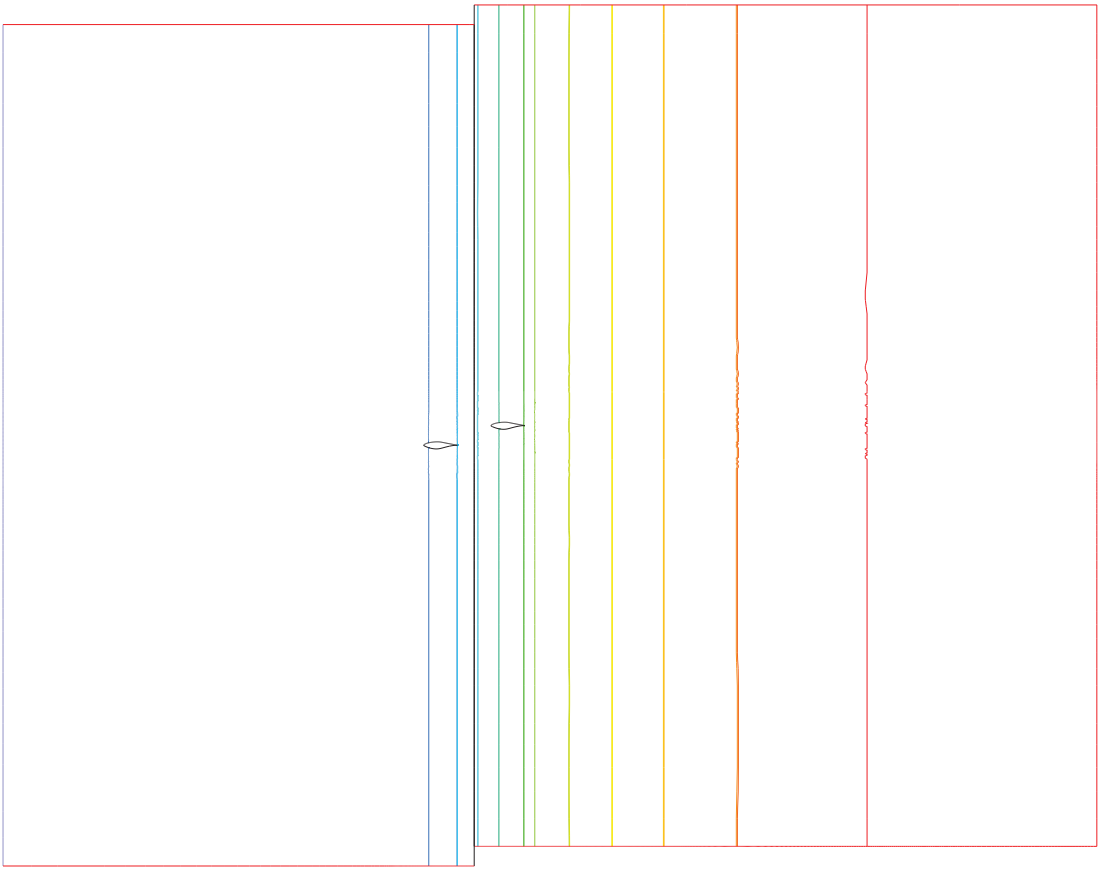

Figure A.1: The partitioning of the grid for parallel computing.

Appendix B

User-defined functions

A short introduction to user-defined functions (UDFs) in Fluent is given in Section 3.7. This section provides an example of a source file used to define an oscillating motion as well as a description of the DEFINE_ZONE_MOTION macro, which was used to define the UDFs that controlled the motion of the cell zone that included the oscillating airfoil.

The source file of the UDF is written in the C programming language and may contain a single or multiple UDF definitions. An example of a source file is given here.

Contents of `oscillation_motion.C`:

```
#include "udf.h"

DEFINE_ZONE_MOTION(amp00125freq157,omega,axis,origin,
    velocity,time,dtime)
{
        real amp,freq,pi; /* Declare variables */
        pi = 3.14159265; /* Define pi */

        /* Define variables */
        amp = 0.0125; /* Amplitude */
        freq = 2 * pi * 0.729997082; /* Oscillation
           frequency */

        /* Define grid motion */
        velocity[1] = amp * freq * cos(freq*time); /* y-
           component of velocity */
}
```

The first line, `#include "udf.h"`, of the source code includes the udf.h file which contains definitions for DEFINE macros as well as `#include` compiler directives for C library function header files. The udf.h file must be included at the beginning of all UDF source code files. In the study, several UDFs were defined in the source file while this example shows only one UDF being defined.

The general usage of the DEFINE_ZONE_MOTION macro is given by

```
DEFINE_ZONE_MOTION(name,omega,axis,origin,velocity,time,
    dtime)
```

where the arguments are described in Table B.1. All the variables apart from `name` are passed by the solver to the UDF.

Table B.1: Descriptions of arguments in the DEFINE_ZONE_MOTION macro. From the Fluent UDF Manual [17].

Argument type	Argument	Description
symbol	name	UDF name
real	*omega	Pointer to the rotational velocity magnitude, default 0
real	axis[3]	Rotation axis direction vector, default (0 0 1) and (1 0 0) for 2D axisymmetric cases
real	origin[3]	Rotation axis origin vector, default (0 0 0)
real	velocity[3]	Translational velocity vector, default (0 0 0)
real	current_time	Current time
real	dtime	Current time step

Appendix C

Results from regression analysis

This appendix presents the detailed results of the regression analysis performed with Minitab 16.1.1 for $X_{shift} = 1$ for both the NACA 0012 and the S809 airfoils.

Output for the NACA 0012 airfoil:

```
General Regression Analysis: eta versus h; k

Regression Equation

eta = −3,66264 + 25,9382 h + 8,99431 k − 86,8274 h*h −
   10,0983 h*k − 12,369
         k*k + 134,479 h*h*h + 16,3054 h*h*k + 1,15142 h*k*
            k + 8,41026 k*k*k −
         73,6328 h*h*h*h − 20,0812 k*h*h*h + 4,95458 k*k*h*
            h − 1,25308 k*k*k*h −
         2,02871 k*k*k*k


Coefficients

Term          Coef  SE Coef         T      P
Constant    −3,663   0,7870  −4,65365  0,000
h           25,938   7,4880   3,46396  0,004
k            8,994   2,0971   4,28893  0,001
h*k        −10,098   8,0883  −1,24851  0,232
h*h        −86,827  35,9801  −2,41320  0,030
k*k        −12,369   2,5858  −4,78344  0,000
k*k*k        8,410   1,6567   5,07636  0,000
h*h*h      134,479  77,8480   1,72746  0,106
h*k*k        1,151   4,6975   0,24511  0,810
h*h*k       16,305  13,3542   1,22100  0,242
k*k*k*k     −2,029   0,4388  −4,62362  0,000
h*h*h*h    −73,633  58,6282  −1,25593  0,230
k*k*k*h     −1,253   1,1061  −1,13287  0,276
k*k*h*h      4,955   3,3060   1,49867  0,156
k*h*h*h    −20,081   8,5543  −2,34749  0,034
```

Summary of Model

S = 0,0473128 R–Sq = 97,28% R–Sq(adj) = 94,55%
PRESS = 0,354902 R–Sq(pred) = 69,14%

Analysis of Variance

Source	DF	Seq SS	Adj SS	Adj MS	F	P
Regression	14	1,1187	1,1187	0,07991	35,6982	0,00000
h	1	0,0278	0,0269	0,02686	11,9991	0,00380
k	1	0,0097	0,0412	0,04118	18,3950	0,00075
h*k	1	0,2908	0,0035	0,00349	1,5588	0,23232
h*h	1	0,0734	0,0130	0,01304	5,8236	0,03010
k*k	1	0,3487	0,0512	0,05122	22,8813	0,00029
k*k*k	1	0,1330	0,0577	0,05769	25,7695	0,00017
h*h*h	1	0,0758	0,0067	0,00668	2,9841	0,10607
h*k*k	1	0,0277	0,0001	0,00013	0,0601	0,80993
h*h*k	1	0,0263	0,0033	0,00334	1,4908	0,24225
k*k*k*k	1	0,0576	0,0479	0,04785	21,3778	0,00039
h*h*h*h	1	0,0031	0,0035	0,00353	1,5774	0,22970
k*k*k*h	1	0,0135	0,0029	0,00287	1,2834	0,27630
k*k*h*h	1	0,0191	0,0050	0,00503	2,2460	0,15617
k*h*h*h	1	0,0123	0,0123	0,01234	5,5107	0,03413
Error	14	0,0313	0,0313	0,00224		
Total	28	1,1501				

Fits and Diagnostics for Unusual Observations

Obs	eta	Fit	SE Fit	Residual	St Resid	
13	0,526950	0,469874	0,0379740	0,057076	2,02241	R
14	0,030203	0,066321	0,0438487	−0,036118	−2,03244	R
15	0,720950	0,622203	0,0319292	0,098747	2,82825	R

R denotes an observation with a large standardized residual.

Output for the S809 airfoil:

```
General Regression Analysis: eta versus h; k

Regression Equation

eta  =  −3,55617 + 23,4688 h + 9,40614 k − 65,8698 h*h −
   17,968 h*k − 11,3553
        k*k + 93,2528 h*h*h + 17,4359 k*h*h + 8,49241 k*k*
           h + 6,63564 k*k*k −
        50,5513 h*h*h*h − 10,3716 k*h*h*h − 0,798873 k*k*h
           *h − 2,27098 k*k*k*h
        − 1,43778 k*k*k*k


Coefficients

Term            Coef  SE Coef         T      P
Constant    −3,5562   0,3808  −9,33805  0,000
h           23,4688   2,9244   8,02520  0,000
k            9,4061   1,0577   8,89279  0,000
h*k        −17,9680   4,4937  −3,99849  0,000
h*h        −65,8698  10,8993  −6,04351  0,000
k*k        −11,3553   1,2186  −9,31797  0,000
h*h*h       93,2528  20,0305   4,65553  0,000
k*k*k        6,6356   0,7978   8,31733  0,000
k*k*h        8,4924   2,5527   3,32685  0,002
k*h*h       17,4359   7,1444   2,44050  0,021
h*h*h*h    −50,5513  13,6298  −3,70888  0,001
k*k*k*k     −1,4378   0,2218  −6,48315  0,000
k*k*k*h     −2,2710   0,6038  −3,76109  0,001
k*k*h*h     −0,7989   1,9516  −0,40934  0,685
k*h*h*h    −10,3716   4,2392  −2,44660  0,021


Summary of Model

S = 0,0326544      R–Sq = 97,59%         R–Sq(adj) = 96,38%
PRESS = 0,155980   R–Sq(pred) = 87,40%


Analysis of Variance

Source       DF  Seq SS  Adj SS   Adj MS        F        P
Regression   14  1,2083  1,2083  0,08630  80,9364  0,00000
  h           1  0,0263  0,0687  0,06867  64,4039  0,00000
  k           1  0,0759  0,0843  0,08433  79,0817  0,00000
```

h*k	1	0,3637	0,0171	0,01705	15,9879	0,00042
h*h	1	0,0597	0,0390	0,03895	36,5241	0,00000
k*k	1	0,3214	0,0926	0,09258	86,8245	0,00000
h*h*h	1	0,0260	0,0231	0,02311	21,6740	0,00007
k*k*k	1	0,1584	0,0738	0,07377	69,1780	0,00000
k*k*h	1	0,0522	0,0118	0,01180	11,0680	0,00247
k*h*h	1	0,0494	0,0064	0,00635	5,9560	0,02125
h*h*h*h	1	0,0136	0,0147	0,01467	13,7558	0,00091
k*k*k*k	1	0,0384	0,0448	0,04482	42,0313	0,00000
k*k*k*h	1	0,0161	0,0151	0,01508	14,1458	0,00079
k*k*h*h	1	0,0008	0,0002	0,00018	0,1676	0,68540
k*h*h*h	1	0,0064	0,0064	0,00638	5,9859	0,02096
Error	28	0,0299	0,0299	0,00107		
Total	42	1,2381				

Fits and Diagnostics for Unusual Observations

Obs	eta	Fit	SE Fit	Residual	St Resid	
1	0,153750	0,189574	0,0298905	−0,035824	−2,72466	R
5	0,439750	0,379298	0,0231612	0,060452	2,62619	R
12	0,044665	0,112046	0,0262679	−0,067381	−3,47348	R

R denotes an observation with a large standardized residual.

Bibliography

[1] K. D. Jones, C. M. Dohring, and M. F. Platzer. Experimental and computational investigation of the Knoller-Betz effect. *AIAA Journal*, 36(7):1240–1246, 1998.

[2] J. Guerrero. *Numerical Simulation of the Unsteady Aerodynamics of Flapping Flight*. PhD thesis, University of Genoa, 2009.

[3] K. D. Jones, C. M. Dohring, and Platzer M. F. Wake structures behind plunging airfoils: A comparison of numerical and experimental results. *AIAA Paper 96-0078-CP*, 1996.

[4] I. H. Tuncer and M. F. Platzer. Thrust generation due to airfoil flapping. *AIAA Journal*, 34(2):324–331, 1996.

[5] S.B. Pope. *Turbulent flows*. Cambridge University Press, 2000.

[6] H.K. Versteeg and W. Malalasekera. *An introduction to computational fluid dynamics: the finite volume method*. 2nd edition.

[7] D.C. Wilcox. *Turbulence modeling for CFD*. 3rd edition.

[8] P. G. Tucker and Z. Pan. URANS computations for a complex internal isothermal flow. *Computer Methods in Applied Mechanics and Engineering*, 190(22-23):2893–2907, 2001. Cited By (since 1996): 5.

[9] M.M. Zdravkovich. *Flow Around Circular Cylinders: Fundamentals*. Oxford science publications. Oxford University Press, 1997.

[10] P. Freymuth. Propulsive vortical signature of plunging and pitching airfoils. *AIAA Journal*, 26(7):881–883, 1988. Cited By (since 1996): 62.

[11] J. C. S. Lai and M. F. Platzer. Jet characteristics of a plunging airfoil. *AIAA Journal*, 37(12):1529–1537, 1999.

[12] Ansys Fluent 13.0 Theory guide. 2009.

[13] Ansys Fluent 13.0 User guide. 2009.

[14] J. Young and J. C. S. Lai. Mechanisms influencing the efficiency of oscillating airfoil propulsion. *AIAA Journal*, 45(7):1695–1702, 2007.

[15] S. Heathcote, Z. Wang, and I. Gursul. Effect of spanwise flexibility on flapping wing propulsion. *Journal of Fluids and Structures*, 24(2):183–199, 2008.

[16] K. Parker, K. D. Von Ellenrieder, and J. Soria. Using stereo multigrid DPIV (SMDPIV) measurements to investigate the vortical skeleton behind a finite-span flapping wing. *Experiments in Fluids*, 39(2):281–298, 2005.

[17] Ansys Fluent 13.0 UDF manual. 2009.

[18] M. F. Platzer, K. D. Jones, J. Young, and J. C. S. Lai. Flapping-wing aerodynamics: Progress and challenges. *AIAA Journal*, 46(9):2136–2149, 2008.

[19] R. Knoller. Die Gesetze des Luftwiderstandes. *Flug- und Motortechnik (Wien)*, 3(21):1–7, 1909.

[20] A. Betz. Ein Beitrag zur Erklaerung des Segelfluges. *Zeitschrift fur Flugtechnik und Motorluftschiffahrt*, 3:269–272, 1912.

[21] W. Shyy, H. Aono, S. K. Chimakurthi, P. Trizila, C. . Kang, C. E. S. Cesnik, and H. Liu. Recent progress in flapping wing aerodynamics and aeroelasticity. *Progress in Aerospace Sciences*, 46(7):284–327, 2010.

[22] G. K. Taylor, R. L. Nudds, and A. L. R. Thomas. Flying and swimming animals cruise at a Strouhal number tuned for high power efficiency. *Nature*, 425(6959):707–711, 2003.

[23] M. S. Triantafyllou, G. S. Triantafyllou, and R. Gopalkrishnan. Wake mechanics for thrust generation in oscillating foils. *Physics of Fluids A*, 3(12):2835–2837, 1991.

[24] Triantafyllou M. S. Triantafyllou, G. S. and M. A. Grosenbaugh. Optimal thrust development in oscillating foils with application to fish propulsion. *Journal of Fluids and Structures*, 7:205–224, 1993.

[25] Z. J. Wang. Vortex shedding and frequency selection in flapping flight. *Journal of Fluid Mechanics*, 410:323–341, 2000.

[26] J. Young. *Numerical Simulation of the Unsteady Aerodynamics of Flapping Airfoils*. PhD thesis, The University of New South Wales, 2005.

[27] J. Young and J. C. S. Lai. Oscillation frequency and amplitude effects on the wake of a plunging airfoil. *AIAA Journal*, 42(10):2042–2052, 2004.

[28] J. Katz and A. Plotkin. *Low-Speed Aerodynamics From Wing Theory to Panel Methods*. McGraw-Hill, Inc., New York, 1991.

[29] I.E. Garrick. Propulsion of a flapping and oscillating airfoil. *NACA*, 567, 1937.

[30] D.M. Somers. Design and experimental results for the S809 airfoil. *NREL-SR-440-6918*, 1997.

[31] H. Schlichting and K. Gersten. *Boundary-layer theory*. 8th edition.

[32] R. Eppler. *Airfoil design and data*. Springer-Verlag, 1990.

[33] F. R. Menter, R. B. Langtry, S. R. Likki, Y. B. Suzen, P. G. Huang, and S. Voelker. A correlation-based transition model using local variables - Part I: Model formulation. *Journal of Turbomachinery*, 128(3):413–422, 2006.

[34] Vebjørn Tveiterås. Numerical study of the interaction of flow over two airfoils. Project work TFY4510 at NTNU, 2010.

[35] R. B. Langtry, F. R. Menter, S. R. Likki, Y. B. Suzen, P. G. Huang, and S. Völker. A correlation-based transition model using local variables - Part II: Test cases and industrial applications. *Journal of Turbomachinery*, 128(3):423–434, 2006.

[36] F. R. Menter. Two-equation eddy-viscosity turbulence models for engineering applications. *AIAA Journal*, 32(8):1598–1605, 1994.

[37] M.M. Zdravkovich. *Flow Around Circular Cylinders: Fundamentals*. Oxford science publications. Oxford University Press, 1997.

[38] J. M. Anderson, K. Streitlien, D. S. Barrett, and M. S. Triantafyllou. Oscillating foils of high propulsive efficiency. *Journal of Fluid Mechanics*, 360:41–72, 1998.

[39] H. Bénard. Formation of centres of circulation behind a moving obstacle. *Comptes Rendus Academie des Sciences*, 147:839–842, 1908.

[40] C. H. K. Williamson. Vortex dynamics in the cylinder wake. 28:477–539, 1996.

[41] C. M. Rhie and W. L. Chow. Numerical study of the turbulent flow past an airfoil with trailing edge separation. *AIAA Journal*, 21(11):1525–1532, 1983.

[42] Gambit 2.4 User's guide. 2007.

[43] Minitab 16.1.1 StatGuide. 2009.

[44] P. R. Spalart. Strategies for turbulence modelling and simulations. *International Journal of Heat and Fluid Flow*, 21(3):252–263, 2000. Cited By (since 1996): 239.